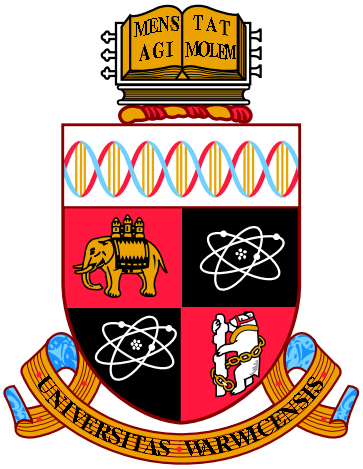

Design and Simulation of Nanofluidic Branching Networks

by

David Stephenson

Thesis

Submitted to the University of Warwick

for the degree of

Doctor of Philosophy

School of Engineering

March 2015

THE UNIVERSITY OF WARWICK

Contents

List of Tables

List of Figures

Acknowledgments

First and foremost, I would like to thank my supervisor, Duncan Lockerby, for his support and guidance throughout the last three and a half years. My thanks also go to all the researchers in the 'Non-equilibrium Fluid Dynamics for Micro/Nano Engineering Systems' project group for their useful discussions along the way — in particular, to Matthew Borg for his help and advice regarding OpenFOAM and molecular dynamics, and to Alex Patronis for his words of wisdom regarding all things computational. I am grateful for the funding provided by the EPSRC in the form of Programme Grant EP/I011927/1 and grant EP/K038664/1. Finally, although it goes without saying, I want to thank my family for their unconditional love and support.

Declarations

This thesis is submitted to the University of Warwick in support of my application for the degree of Doctor of Philosophy. It has been composed by myself and has not been submitted in any previous application for any degree. The work presented (including data generated and data analysis) was carried out by the author.
Parts of this thesis have been published by the author:

The hybrid methodology developed in Chapter 2 is published in

> David Stephenson, Duncan A. Lockerby, Matthew K. Borg, Jason M. Reese. Multiscale simulation of nanofluidic networks of arbitrary complexity, *Microfluidics and Nanofluidics*, 2014.
>
> David Stephenson, Duncan A. Lockerby, Matthew K. Borg, Jason M. Reese. Multiscale simulation of nanofluidic networks, *12*$^{\text{th}}$ *International Conference on Nanochannels, Microchannels, and Minichannels, 2014, Chicago, USA*.

The extended hybrid methodology developed in Chapter 3 is published in

> David Stephenson, Duncan A. Lockerby, Matthew K. Borg, Jason M. Reese. A hybrid molecular-continuum design tool for multiscale nanofluidic networks, *Microfluidics and Nanofluidics*, 2015 (Under review).
>
> David Stephenson, Duncan A. Lockerby, Matthew K. Borg, Jason M. Reese. Design of multiscale nanofluidic networks, *13*$^{\text{th}}$ *International Conference on Nanochannels, Microchannels, and Minichannels, 2015, San Francisco, USA* (In press).

The optimisation principle developed in Chapters 5 and 6 applied to symmetric branching is published in

> David Stephenson, Alexander Patronis, David M. Holland, Duncan A. Lockerby. Generalizing Murray's Law: an optimization principle for fluidic networks of all shapes and sizes, *Journal of Applied Physics*, 2015 (Under review).

The optimisation principle developed in Chapters 5 and 6 applied to asymmetric branching is published in

> David Stephenson, Duncan A. Lockerby. A generalised optimisation principle for asymmetric branching in fluidic networks, *Proceeding of the Royal Society A*, 2015 (Under review).

Abstract

Branching networks play a major role in a variety of physiological and engineering structures over a range of physical scales. However, increasingly, artificial systems are being tailored towards the nanoscale to reduce costs and improve performance and process control. In this thesis, analytical and numerical models are developed to enable the efficient design and accurate simulation of nanofluidic branching networks, where non-continuum/non-equilibrium effects prohibit the use of common solutions.

A hybrid molecular-continuum method is presented for the design and simulation of general high-aspect-ratio nanofluidic networks. This increases the scope of hybrid techniques in two main ways: 1) the method is generalised to accurately model any nanofluidic network of connected channels, regardless of its size or complexity; 2) by generalising the application of constraints, the geometry or governing pressures can be the output of the method, enabling the design of networks without the need for a costly trial-and-error process. For a variety of constraint combinations, it is shown that the hybrid method converges quickly to the solution of a full molecular dynamics simulation, with relative errors of $< 4\%$ for all variables across all cases.

Network design is further advanced by the development of a generalised optimisation principle that finds the daughter-parent area ratio maximising flow conductance per unit volume in all branches. Through numerically verified analytical models, it is demonstrated that the common branching principle 'Murray's law' is sub-optimal for asymmetric branching (where the local optimisation of each individual channel does not correspond to the global optimum for the network as a whole), while the generalised law presented in this thesis is valid for 1) symmetric and asymmetric branching, 2) slip and plug flows, which occur at very small scales, and 3) any cross-sectional shape; making it a powerful tool for nanofluidic biomimetic modelling.

Preface

Fluid transport through branching networks is of critical importance to a number of natural and artificial systems, with applications spanning a diverse range of subject areas including physiology, biology, chemistry, geology, and engineering. Prominent examples include mammalian cardiovascular systems [Murray, 1926a,b,c] and bronchial trees [Horsfield and Cumming, 1967; Horsfield et al., 1976; Horsfield and Cumming, 1968], plant xylem [McCulloh et al., 2003, 2004; McCulloh and Sperry, 2005], river and canal networks [Horton, 1945], electronic cooling systems [Chen and Cheng, 2002; Wang et al., 2006], fuel cells [Senn and Poulikakos, 2004], microreactors [Renault et al., 2012], and a myriad of lab-on-a-chip devices [Kovarik and Jacobson, 2009; Jiang et al., 2010; Segerink and Eijkel, 2014; Prakash and Yeom, 2014]. As technology evolves, artificial networks are being increasingly designed at smaller scales to benefit from enhanced operation efficiency and process control, e.g. miniaturised heat exchangers make effective cooling systems as their efficiency improves with decreasing size, owing to an increase in the heat-transport coefficient and surface-volume ratio [Tuckerman and Pease, 1981]; nanotube membranes have great potential in desalination applications as they have demonstrated the ability to control the permeation of ions [Lee et al., 2011] and enhance fluidic transport [Mattia and Calabrò, 2012]. In addition, small devices are attractive as they come with a low economic cost in terms of fabrication and fluid consumption.

Modelling nanofluidic branching networks comprises two major challenges: accurate simulation and efficient design. As channel heights approach the nanoscale, simulating the physical behaviour of a fluid through high-aspect-ratio networks becomes a formidable problem: non-continuum/non-equilibrium effects near surfaces are more prominent and render the continuum approximation invalid [Gad-el Hak, 1999]; however, a full molecular resolution is computationally prohibitive as channel lengths are still relatively large. To accurately resolve the molecular phenomena within a reasonable time frame, a hybrid method is required that combines the efficiency of a continuum solver with the precision of a molecular solver. Hy-

brid methods are a relatively new approach to fluid simulation and require a high degree of scale separation between the macroscopic processes and molecular phenomena. This is difficult to obtain in a high-aspect-ratio branching network, as non-continuum/non-equilibrium effects persist across the entire channel height and the variation of thermodynamic variables through the junction can not easily be predicted — as such, there currently lacks a computationally and physically robust method capable of modelling these geometries.

Hybrid simulations can also play an important role in nanofluidic network design, where the geometry must conform to satisfy a particular thermodynamic variable, e.g. shear stress, mass flow rate, etc. More generally, however, network design considers the optimal geometrical form of branching in terms of the relative cross sections of the daughter 'branches' and the parent 'trunk', and the angle of the branching junction. Optimisation principles operate by minimising a 'cost' function and many have been developed to model branching structures: most famously, the principle of minimum work by Murray [1926a,c], but also (among others) the principle of minimum mass [Williams et al., 2008], and the principle of minimum volume [Kamiya and Togawa, 1972]. However, all existing optimisation principles exhibit common limitations that make them inaccurate or invalid for modelling artificial nanofluidic networks, which often require: 1) non-circular and varying cross-sectional shapes (e.g. a constant depth), owing to fabrication restrictions; and 2) a non-continuum description of the fluid flow, owing to the small scale.

The purpose of this thesis is to improve the scope of both the simulation and design facets of nanofluidic branching network modelling through the creation, development, and verification of new analytical and numerical methodologies. To reflect the dual nature of the modelling challenge, the thesis is split into two parts as outlined in the next section.

Thesis outline

Part 1 focuses on the simulation challenge through the development and verification of a new hybrid method for high-aspect-ratio nanofluidic branching networks — the general networks internal-flow multiscale method (GeN-IMM).

Chapter 1 presents an introduction to the function of hybrid multiscale methods and the limitations that prohibit current methods from being useful for the high-aspect-ratio problems considered in this thesis. An overview of molecular dynamics (MD) — the molecular solver of choice for this thesis — is also given.

In Chapter 2, the methodology and algorithm for the GeN-IMM is detailed.

The new hybrid method is verified against full MD simulations for some simple test networks: 1) a straight channel connecting two reservoirs; and 2) a bifurcating channel. Agreement between the GeN-IMM and full MD solutions are analysed in terms of the measured macroscopic properties and the captured nanoscale phenomena. Total computational expense is also compared.

The GeN-IMM is further generalised in Chapter 3 to function as a design tool by enabling a wide variety of different properties (e.g. geometric features, mass flow rate, pressure, etc.) to be constrained throughout the network. The converged solutions for the hybrid method are compared to the results from full MD simulations for a range of constraint combinations. The precision and efficiency of the GeN-IMM is again highlighted.

Part 2 focuses on the design challenge through the development and verification of a new optimisation principle for fluidic branching networks — the generalised law.

Chapter 4 presents on overview of existing optimal branching principles, including an in-depth derivation of the ubiquitous Murray's law, and highlights the limitations that prevent current methods from being fully utilised as a design tool for engineering problems.

In Chapter 5, a generalised law is derived for the optimal daughter-parent area ratio in a two-level branching network. Analytical solutions describe the optimal geometrical arrangement for 1) asymmetric branching, 2) any cross-sectional shape, and 3) any length-scale. It is shown that there are two limiting cases of scale: 1) the continuum-flow limit at large scales, where there is no slip at the walls and the velocity profile is parabolic; and 2) the plug-flow limit at small scales, where the velocity profile is dominated by slip at the walls and becomes plug-like. The shortcomings of Murray's law are highlighted and results are numerically verified.

In Chapter 6, the generalised law is applied to more complicated fluidic network cases: 1) to constant-depth networks across the entire range of length scales, where it is shown that there are high- and low-aspect-ratio limits at each of the scale limits; and 2) to non-Newtonian and turbulent fluidic networks at the continuum-flow limit, where the deficiencies of a Murray's law approach to optimal asymmetric branching are further demonstrated. Finally, the generalised law is extended to consider optimal branching angles in bifurcating networks for a variety of cross-sectional shapes and scales. All analytical solutions are numerically verified.

The key findings of this thesis, and a discussion of how this work can be advanced in the future, are presented in Chapter 7.

Part I

Multiscale Modelling for Nanofluidic Networks of Arbitrary Complexity

Abbreviations

Latin

a	Acceleration $[m/s^2]$ or equation of state coefficient [various]
D	Flow-conductance coefficient $[m \cdot s]$
e	Relative error [%]
F	Force $[N]$
H	Channel height $[m]$
K	Flow-conductance coefficient $[m \cdot s]$
L	Channel component length $[m]$
L'	Channel micro-element length $[m]$
m	Mass $[kg]$
$\dot{m}$	Mass flow rate $[kg/s]$
N	Number of molecules $[-]$
P	Pressure $[Pa]$
Q	Number of components $[-]$
Q_v	Number of components under a volume constraint $[-]$
r	Position $[m]$

r_c	Potential energy truncation radius $[m]$
T	Temperature $[K]$
t	Time $[s]$
U	Potential energy $[J]$
V	Volume $[m^3]$
v	Velocity $[m/s]$
W	Number of boundaries $[-]$
x, y, z	Cartesian coordinates $[m]$

Greek

β	Order of the polynomial equation of state $[-]$
Γ	Variable macroscopic property [various]
ΔT	Macro-model time scale $[s]$
Δt	Molecular dynamics time-step $[s]$ or micro-model time scale $[s]$
ΔX	Macro-model length scale $[m]$
Δx	Micro-model length scale $[m]$
ϵ	Potential well depth $[J]$
ζ	Residual $[-]$
λ	Channel component prefactor $[s/m]$
μ	Dynamic viscosity $[Pa \cdot s]$
ρ	Mass density $[kg/m^3]$
ρ_n	Number density $[m^{-3}]$

σ	Interatomic separation corresponding to a potential of zero $[m]$
τ	Total simulation time $[s]$ or wall shear stress $[Pa]$
τ_T	Berendsen thermostat coupling time constant $[s]$
Φ	Junction component pressure jump $[Pa]$
χ	Berendsen thermostat velocity modifier $[-]$
Ψ	Artificial region prefactor $[s/m^2]$
Ω	Junction component prefactor $[s/m^2]$

Subscripts

B	Boundary condition or generalised constraint
F	Full molecular dynamics simulation
i, j	Atom/boundary index
LJ	Lennard-Jones
l	Iteration index
$f - f$	Fluid-fluid
M	Multiscale method
p	Component index
q	Component index
q_c	Channel component index
R	Reference quantity
SF	Shifted Lennard-Jones
$w - f$	Wall-fluid

Superscripts

b	Equation of state order index
tol	Tolerance
$*$	Dimensionless quantity

Accents

$\bar{}$	Average value

Acronyms

CPU	Central processing unit
DDM	Domain decomposition method
DSMC	Direct simulation Monte Carlo
GeN-IMM	General networks internal-flow multiscale method
GPU	Graphics processing unit
HMM	Heterogeneous multiscale method
IMM	Internal-flow multiscale method
LJ	Lennard-Jones
MD	Molecular dynamics
μVE	Grand canonical ensemble
NPBCs	Non-periodic boundary conditions
NPT	Isothermal-isobaric ensemble
NVE	Microcanonical ensemble
NVT	Canonical ensemble
PBCs	Periodic boundary conditions
SeN-IMM	Serial networks internal-flow multiscale method

Chapter 1

Introduction and Background

The continuum assumption is central to macroscopic fluidic modelling, whereby the fluid is treated as if it were a continuous material that can be subdivided into infinitesimal elements. Macroscopic properties are described through the conservation of mass, momentum, and energy, e.g. by the Navier-Stokes-Fourier (NSF) equations. As the characteristic length of the fluid flow decreases towards the nanoscale, the flow behaviour becomes highly dependent on molecular phenomena. Examples include surface effects [Schoch et al., 2008], the moving contact line problem [Koplik and Banavar, 1995], the break-up and merging of fluid droplets [Brenner et al., 1994], dynamic melting processes [Thompson and Robbins, 1989], and highly rarefied gases [Bird, 1994]. In these instances, the NSF equations become inaccurate as the continuum approximation is invalid and local thermodynamic equilibrium is not ensured; thus the fluid must be modelled atomistically, via discrete particle collisions. For high-aspect-ratio nanofluidic networks, non-continuum/non-equilibrium effects occur in the form of high velocity slip and (in dense fluid flows) density layering near the channel walls, as the wall-fluid interaction dominates the flow behaviour owing to the large surface-volume ratio.

While the NSF equations are inaccurate for modelling non-continuum/non-equilibrium fluid flows, a full molecular simulation is often also inappropriate. Many engineering applications require a nanoscale resolution to capture non-continuum/non-equilibrium phenomena, e.g. nanotube membranes for sea-water desalination [Mattia and Gogotsi, 2008] or air-purification [Mantzalis et al., 2011], miniaturised heat exchangers for cooling electronic circuits [Yarin et al., 2009], and many lab-on-a-chip devices [Kovarik and Jacobson, 2009; Jiang et al., 2010; Segerink and Eijkel, 2014; Prakash and Yeom, 2014]. However, the size of these systems would render a full molecular simulation computationally intractable, prohibiting comparison with

experimental observation and limiting its use as a design tool. Molecular methods, such as molecular dynamics (MD), are limited to small system sizes, $\mathcal{O}(100\ \text{nm}^3)$, and short simulation times, $\mathcal{O}(100\ \text{ns})$, owing to the high computational cost of modelling particle collisions. The two competing interests of accuracy and computational efficiency can be satisfied by using a multiscale hybrid method that combines a molecular model and a continuum model into one simulation tool.

1.1 Hybrid methods

A vast number of hybrid methods have been developed, each with small nuances in 1) the coupling strategy governing communication between the atomistic and continuum models, and 2) the imposition of boundary conditions. This chapter presents a brief introduction to the main types of hybrid scheme and their suitability for modelling the network-type problems investigated in this thesis. For more detail, see the reviews by Wijesinghe and Hadjiconstantinou [2004], Hadjiconstantinou [2005], Koumoutsakos [2005], Kalweit and Drikakis [2008], and Mohamed and Mohamad [2009]. In this thesis, the term *micro* is used to define a region where a molecular non-continuum/non-equilibrium solution is required; the term *macro* refers to regions where a macroscopic continuum approximation is applied. All hybrid methods function on the premise of exploiting scale separation to enable the coupling of micro and macro solvers. Scale separation exists where the molecular phenomena are only weakly coupled to the macroscopic fluidic processes, and greater scale separation leads to larger computational savings for the hybrid method over a full molecular simulation. Scale separation can either be spatial, where a micro resolution is only required in a relatively small section Δx compared to the macro domain ΔX; or temporal, where the micro phenomena occur over a much faster time scale Δt compared to the time evolution of the macro phenomena ΔT. When $\Delta X \gg \Delta x$ or $\Delta T \gg \Delta t$, the micro and macro models can be decoupled and the micro simulation is performed as if the macro solution were constant.

Broadly speaking, all hybrid methods fall into one of three framework categories: the domain decomposition method (DDM) for *Type I* problems, the heterogeneous multiscale method (HMM) for *Type I* or *Type II* problems, and the internal-flow multiscale method (IMM) for *Type III* problems. *Type I* problems are those for which a macro solution provides reasonable accuracy for much of the flow field and a micro solver is only required for regions that contain non-continuum/non-equilibrium effects such as an isolated defect, a singularity, or regions near nanoscale surfaces (e.g. in the moving contact line problem [Hadjicon-

stantinou, 1999], or to resolve singularities that occur in the corners of lid-driven cavity flows [Nie et al., 2004a]). *Type II* problems are those for which a micro resolution is required to provide constitutive information to continually adjust the macro solver that spans the entire domain (e.g. in nanoscale non-Newtonian fluid flows [Borg et al., 2013c]). *Type III* problems are for high-aspect-ratio nanoscale channels where non-continuum/non-equilibrium effects can occur over the entire (or majority of the) cross-section (e.g. in nanotube desalination membranes [Ritos, 2014] or in the air-layer lubrication of a liquid journal bearing [Patronis et al., 2013; Lockerby et al., 2015]). *Type III* problems are still relatively new; in this thesis, the scope and fundamentals of the hybrid methodology to solve these problems are expanded upon. In the following sections, each of the main hybrid methodological frameworks will be described, along with an assessment of their applicability to *Type III* problems.

1.1.1 Domain decomposition methods

The majority of hybrid techniques fall under the umbrella of DDMs [O'Connell and Thompson, 1995; Hadjiconstantinou and Patera, 1997; Flekkøy et al., 2000; Wagner et al., 2002; Delgado-Buscalioni and Coveney, 2003a; Nie et al., 2004b; Werder et al., 2005; Flekkøy et al., 2005], an intuitively simple method whereby the flow domain is spatially divided into micro subdomains at surfaces, defects, and neighbouring fluid regions, and a macro subdomain in the bulk fluid region (see Fig. 1.1). Physical properties (density, momentum, and energy) and their fluxes must be consistent at the interface between the macro and micro subdomains. To avoid local structuring in the micro subdomain due to domain termination, the interface is often extended into an overlap region so that the average physical properties of molecules can be relaxed to those in the macro subdomain. Coupling between the two subdomains is performed via the information exchange of state variables (e.g. the alternating Schwartz method for steady-state systems and state variable coupling [Hadjiconstantinou and Patera, 1997]) or fluxes (e.g. flux coupling with an explicit numerical scheme for unsteady problems [Delgado-Buscalioni and Coveney, 2003a]), with the information from one subdomain imposed as a boundary condition on the other. This ultimately leads to a converged solution when boundary conditions cease to be updated.

A major difficulty with DDMs is how these boundary conditions are imposed. This is fairly straightforward in the micro-macro direction: molecule properties can be spatially and temporally averaged and applied at nodes in the continuum grid. However, in the macro-micro direction, continuous physical properties have to be

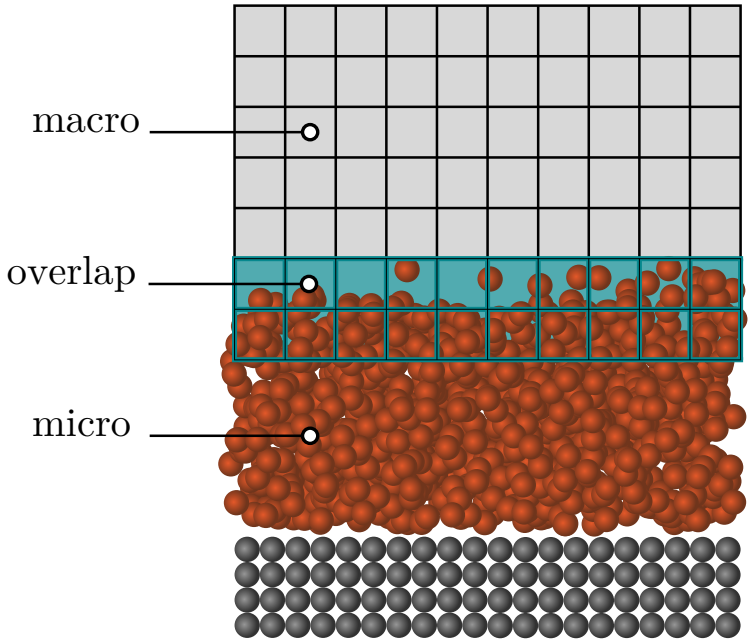

Figure 1.1: Schematic of the DDM for fluid flow past a wall. The macro, micro, and overlap regions are highlighted.

broken down to create a non-unique molecular distribution. There is yet to be a universally applicable methodology for applying a macroscopic field to a set of discrete particles [Mohamed and Mohamad, 2009], and the most appropriate technique will often be dependent on the choice of subdomain solver and the characteristics of the flow type. For example, in the first DDM, O'Connell and Thompson [1995] used momentum conservation to impose a boundary condition on the micro subdomain in an isothermal Couette flow using the Navier-Stokes equations and MD as the macro and micro solvers, respectively. Momentum conservation requires the continuity of stress at the interface, but, for MD, the microscopic stress tensor is a function of the kinetic and virial terms. Thus, to impose stress continuity, the length-scale and magnitude of the corrective forcing applied to the particles would need to be known *a priori*. This problem was overcome by relaxing the average momentum of the particles in the overlap region to that of the corresponding continuum fluid element through the application of constraint dynamics, thereby allowing the momentum transport across the interface to be handled by the interactions of the MD particles themselves.

The disadvantage of applying DDMs for high-aspect-ratio networks is that for long, narrow channels the entire length of the bounding wall must be simulated using the micro solver, and the bulk region is relatively small compared to what can

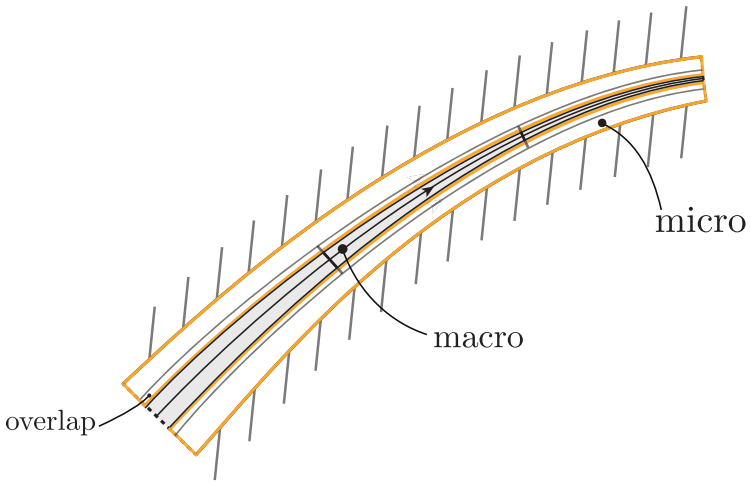

Figure 1.2: Schematic of the DDM in a high-aspect-ratio channel. Reproduced from Borg et al. [2013b].

be considered the near-wall region (see Fig. 1.2). This renders the computational savings of the hybrid method minimal compared to a full molecular simulation and severely restricts the system dimensions for which DDMs can practically be used. Another drawback is the challenging requirement for the micro solver to employ non-periodic boundary conditions (NPBCs) at the coupling interface, which for some molecular methods (e.g. MD) are an underdeveloped area. Finally, the accuracy of the coupling is significantly diminished if the fluid viscosities used in the micro and macro solvers are not exactly equal [Delgado-Buscalioni and Coveney, 2003a].

1.1.2 Heterogeneous multiscale methods

An alternative method, termed the HMM, was first proposed by E and Engquist [2003], whereby the entire domain is spanned by the macro solver, and the micro solvers provide local refinement at chosen grid points in the form of missing numerical data, see Fig. 1.3. While applicable to *Type I* problems, the HMM [E and Engquist, 2003; E et al., 2003; Ren and E, 2005; E et al., 2007; Yasuda and Yamamoto, 2008; E et al., 2009; Asproulis et al., 2012; Alexiadis et al., 2013; E, 2011] is more often used for *Type II* problems where a microscopic resolution is required throughout the domain, e.g. in the case of a polymeric fluid flow [Ren and E, 2005].

The HMM framework uses a top-down approach where the aim is to numerically approximate the macroscopic state of the system. This broadly consists of two steps [E et al., 2007]: 1) selecting a suitable macro model, and 2) estimating the missing macroscopic data from a constrained micro model. The choice of macro

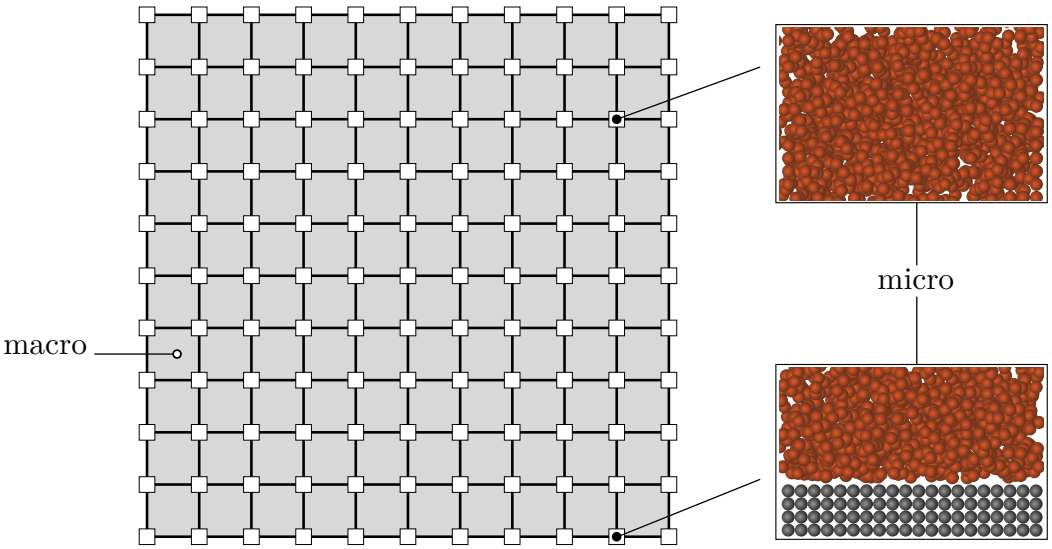

Figure 1.3: Schematic of the HMM for a fluid with unknown constitutive relations. The macro solver is represented by the background grid while the micro solver is applied at each node. Snapshots of the micro solver simulation domain in the bulk fluid and at the walls are shown as insets.

model is dependent on the nature of the problem, e.g. whether it is variational, whether it is conservative, etc. For dynamic problems that are conservative, the conservation of mass and momentum will often suffice. But this macro model will be missing information, e.g. the stress tensor, or will be invalid in part of the computational domain, e.g. around a singularity. An approximation of the macroscopic state can be obtained by solving the macro model in terms of some state variable, e.g. the velocity field, which is applied as a boundary condition to locally constrain the micro simulations. This ensures consistency between the states of the macro and micro domains. At each point where missing constitutive or boundary information is required, a constrained micro simulation is performed (e.g. using MD) and the spatially and temporally averaged data is passed back to the macro model. In the fluid bulk, this data is often the stress tensor, while micro simulations neighbouring a wall may also provide values of the velocity slip.

A key benefit of the HMM is it circumvents the need to model high-order constitutive relations, transport coefficients, or phenomenological boundary conditions, as the coupling process is done through data exchange, which can be stresses, fluxes, forces, elastic coefficients, etc. In addition, both length- and time-scale separation are naturally exploited as the micro solver is completely decoupled from the macro solver and need only be large enough and simulated for a sufficient amount

of time as to generate low-noise data.

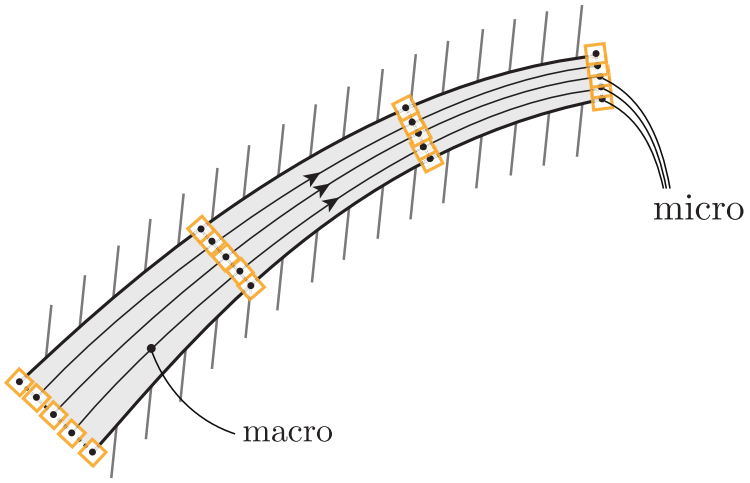

Figure 1.4: Schematic of the HMM in a high-aspect-ratio channel. As the channel narrows, micro subdomains overlap. Reproduced from Borg et al. [2013b].

The main drawback to using the HMM for the high-aspect-ratio networks presented in this thesis is that, in narrow flow channels, the micro solver domains are forced to overlap considerably (see Fig. 1.4), which renders the efficiency and accuracy of the hybrid method lower than that of a pure micro simulation. This occurs because the HMM requires a number of micro subdomains to accurately capture the macroscopic variables (e.g. the velocity profile) and each micro subdomain has a minimum size requirement (to prevent simulation artefacts) which is of similar magnitude to the channel heights for the cases in this thesis. Furthermore, micro solvers not directly adjacent to the wall are judged to be in the bulk fluid and thus are assumed to be unaffected by non-continuum/non-equilibrium wall effects, such as molecular layering (in dense fluids) and Knudsen layer effects (in gases). However, these non-continuum/non-equilibrium effects are still present near the centre of a narrow channel, so the micro solvers not directly adjacent to the wall would process inaccurate information. In addition, for dense fluids the molecular layering effect causes the strain rate to vary rapidly [Todd et al., 2008] and stress no longer exhibits the local linear behaviour [Todd, 2005; Cadusch et al., 2008] which HMM assumes: incurring further inaccuracies. Moreover, NPBCs are still required for micro simulations near walls, which presents a problem for some micro solvers, e.g. MD.

1.1.3 Internal-flow multiscale methods

The IMM was first developed by Borg et al. [2013a] to efficiently solve nanoscale high-aspect-ratio geometries for which other hybrid techniques had proven computationally inefficient. Although originally applied to dense fluid flows through serial channels, the IMM has since been used to model rarefied gas flows [Patronis et al., 2013; Patronis and Lockerby, 2014] and more complex network geometries [Borg et al., 2013b]. The IMM hybridisation exploits length-scale separation between the gradually varying macroscopic processes occurring in the streamwise direction (i.e. along scales similar to the channel length), and the rapidly varying molecular processes occurring in transverse direction (i.e. along scales similar to the channel height). This means that no scale separation exists perpendicular to the flow direction and each micro subdomain must cover the entire channel height (see Fig. 1.5). Fully periodic micro subdomains are placed at regular intervals along the channel length, with cross sections chosen to match the local geometry.

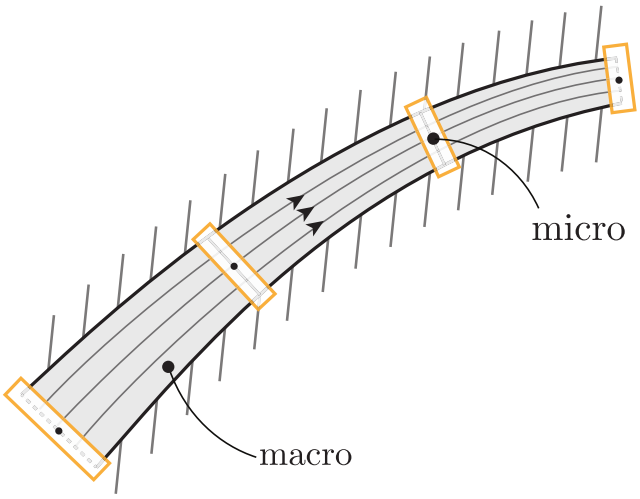

Figure 1.5: Schematic of the IMM in a high-aspect-ratio channel. Reproduced from Borg et al. [2013b].

The macro model uses the simple one-dimensional equations for mass and momentum conservation. These equations do not require constitutive or boundary relations (such as viscosity or velocity slip, respectively) to be defined by the macro model or explicitly calculated by the micro model. Instead, the fluid and wall conditions are implicitly captured by the micro solver as it covers the entire channel cross section. The micro-macro coupling is performed through the spatially and temporally averaged measurement of macroscopic properties, such as mass flow rate, which are used to evaluate macro continuity errors by comparing the values

obtained in different micro subdomains. Macro-micro coupling is performed by 1) adding/deleting particles to set a mean micro subdomain density, and 2) applying an external body force to the particles to induce a local pressure or temperature gradient, with the aim of reducing the macro continuity errors from those of the previous iteration.

The development of the serial networks IMM (SeN-IMM) [Borg et al., 2013b], enabled the hybrid method to be applied to high-aspect-ratio networks that consisted partly of 'junctions' for which scale separation cannot be exploited (e.g. inlet/outlet reservoirs or around channel defects). Junctions are an important part of a fluidic system because their losses can have a sizeable effect on the flow rate, which is a crucial variable in network design, (e.g. in desalination membranes [Nicholls, 2012; Ritos, 2014]). The SeN-IMM adopts variable scale-separation whereby the junctions are simulated in their entirety by the micro solver, and the high-aspect-ratio interlinking channels are modelled with the IMM procedure.

The term 'serial' refers to the fact that, in Borg et al. [2013b], every component in the network could only have one inflow and one outflow, so the mass flow rate was constant in each micro subdomain. In Chapter 2, the variable scale-separation approach used in the SeN-IMM is generalised to be applicable for any number of inlets and outlets, so that it can be used to model branching networks of arbitrary complexity. In Chapter 3, the methodology is further generalised to enable the hybrid method to be utilised as a design tool, rather than just a simulation tool. The hybrid methodology outlined in the following two chapters could be performed with any micro solver, but in this thesis MD is used.

1.2 Molecular dynamics

As the purpose of the micro solver is to model particle interactions, it could reasonably be supposed that the laws of quantum mechanics should be used, with Schrödinger's equation of motion [Schrödinger, 1926] employed to evaluate the evolution of the system through time. However, to do this even numerically is impossible for all but a few simple special cases [Griebel et al., 2007]; thus approximations must be made. The first is the Born-Oppenheimer approximation [Born and Oppenheimer, 1927] which enables the nucleus to be modelled independently of the electrons. The reasoning behind this is that the much smaller mass of the electrons enables them to adjust their position almost instantaneously to the motion of the nucleus. The nucleus, now assumed to be a point particle, can be moved according to classical Newtonian dynamics with interactions modelled by effective potentials

defined by the influence of the electrons. In classical MD, a further approximation is to model these potentials empirically by fitting to data from either quantum mechanical simulations or experiments. This hierarchy of approximations enables the accurate simulation of thousands of atoms to be computationally tractable with modern computational resources.

The interactions between particles (hereon referred to as 'molecules' for brevity) can be modelled simplistically by a pairwise potential $U(r_{ij})$ where $r_{ij} = |r_i - r_j|$ is the intermolecular distance between molecules i and j[1]. In this thesis, the common Lennard-Jones (LJ) potential [Jones, 1924] is used:

$$U_{LJ}(r_{ij}) = 4\epsilon \left[\left(\frac{\sigma}{r_{ij}} \right)^{12} - \left(\frac{\sigma}{r_{ij}} \right)^{6} \right], \tag{1.1}$$

where σ is the intermolecular separation that yields a potential of zero and ϵ is the potential well depth. The potential consists of two terms: the long range attractive term r_{ij}^{-6}, which represents the van der Waals interaction due to electron correlations; and the close range repulsive term r_{ij}^{-12}, which represents the repulsion due to overlapping electron clouds [Rapaport, 2004]. There is no physical reason behind the exponent choice for the repulsive term; 12 is used for the computational convenience of being the square of the attractive term.

The LJ parameters σ and ϵ are dependent on the molecule species. For simplicity, in this thesis, all MD simulations are of dense fluid argon flowing through channels with walls comprised of frozen argon molecules, although the techniques developed in Chapters 2 and 3 are applicable to more complex and realistic molecular models. Argon is very commonly used in MD because it is physically relatively simple. It is monatomic and inert, so molecules behave approximately like hard spheres and can be accurately modelled by a LJ potential. Likewise, the use of frozen argon molecules to represent the wall enables the wall-fluid interaction to be simply modelled by an LJ potential [Thompson and Troian, 1997]. This simplicity enables the MD simulations to be less computationally expensive. The σ and ϵ properties for the fluid-fluid $(f-f)$ and wall-fluid $(w-f)$ interactions are taken from Thompson and Troian [1997], with the intention of generating velocity slip at solid-fluid interfaces — thus making a continuum solver inappropriate. The values for these are, $\sigma_{f-f} = 3.4 \times 10^{-10}$ m, $\epsilon_{f-f} = 1.65678 \times 10^{-21}$ J, and $\sigma_{w-f} = 2.55 \times 10^{-10}$ m, $\epsilon_{w-f} = 0.33 \times 10^{-21}$ J. The mass density of the wall molecules is $\rho_w =$

[1] Although three-body (and higher) terms involving triplets of molecules would influence the potential in reality, their effect is small compared to the pairwise interaction and is highly computationally intensive, so they are usually omitted [Allen and Tildesley, 1987].

6.809 $\times 10^3$ kg/m^3, and the mass of one molecule is 6.6904 $\times 10^{-26}$ kg.

The force applied to the i^{th} molecule $\mathbf{F}_i$ is defined as the sum of the intermolecular pairwise forces:

$$\mathbf{F}_i = \sum_{j=1(\neq i)}^{N} -\nabla U(r_{ij}), \tag{1.2}$$

where N is the total number of molecules and $F(r_{ij}) = -\nabla U(r_{ij})$ is the pairwise force. Calculating the force applied to each molecule is by far the most computationally intensive task in an MD simulation (and scales with N^2), so it is considered good practice to use a radial cut-off r_c to truncate the LJ potential when it becomes sufficiently small as to be deemed negligible. In this thesis, the distance $r_c = 4\sigma$ is used. This cut-off distance has been used in previous studies involving MD in hybrid methods [Borg et al., 2013a,b], and represents the intermolecular separation where the potential is $\approx 0.1\%$ of the potential depth. This results in a slight discontinuity at $r_{ij} = r_c$, the effect of which can be reduced by shifting the entire potential such that

$$U_{SF}(r_{ij}) = \begin{cases} U_{LJ}(r_{ij}) - U_{LJ}(r_c) - (r_{ij} - r_c)\,\nabla U_{LJ}(r_c) & \text{if } r_{ij} < r_c \\ 0 & \text{if } r_{ij} \geq r_c, \end{cases} \tag{1.3}$$

where

$$\nabla U_{LJ}(r_c) = \frac{-48\epsilon}{\sigma}\left[\left(\frac{\sigma}{r_c}\right)^{13} - \left(\frac{\sigma}{r_c}\right)^{7}\right]. \tag{1.4}$$

The intermolecular force $F(r_{ij})$ for the truncated LJ potential is then

$$F_{SF}(r_{ij}) = \frac{48\epsilon}{\sigma}\left[\left(\frac{\sigma}{r_{ij}}\right)^{13} - \left(\frac{\sigma}{r_{ij}}\right)^{7} - \left(\left(\frac{\sigma}{r_c}\right)^{13} - \left(\frac{\sigma}{r_c}\right)^{7}\right)\right]. \tag{1.5}$$

Figure 1.6 compares the standard and truncated LJ potentials and forces in dimensionless units, i.e. lengths are expressed in terms of σ and energy is expressed in terms of ϵ.

Molecules move by relating the applied force to their acceleration via Newton's second law of motion:

$$\mathbf{F}_i = m_i \mathbf{a}_i, \tag{1.6}$$

where m_i and $\mathbf{a}_i = \ddot{\mathbf{r}}_i$ are the mass and acceleration of the i^{th} molecule, respectively. The system evolves in time by numerically integrating a discretized version of equation (1.6) for the positions $\mathbf{r}_i$ and velocities $\mathbf{v}_i = \dot{\mathbf{r}}_i$ of each molecule over a

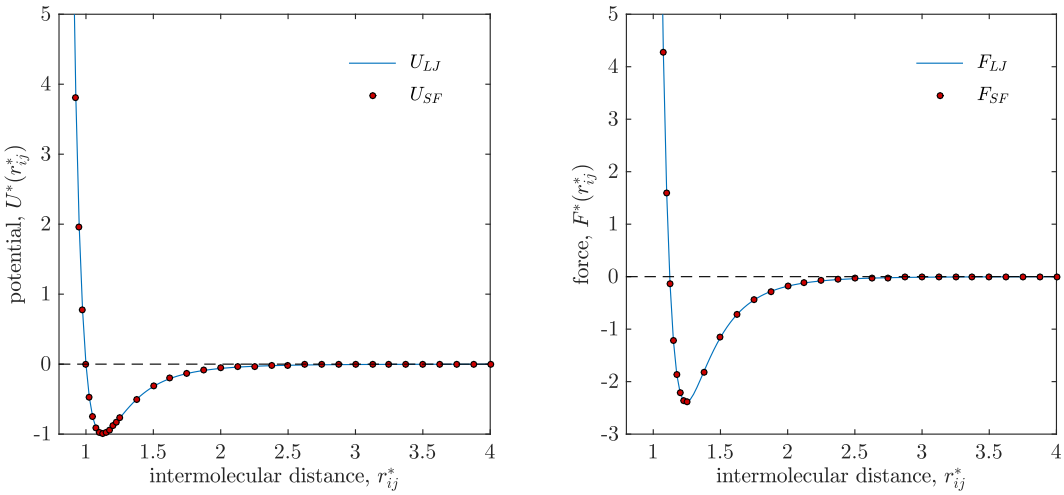

Figure 1.6: The standard and truncated dimensionless Lennard-Jones intermolecular **(a)** potential $U^*(r_{ij}^*)$ and **(b)** force $F^*(r_{ij}^*)$ against dimensionless intermolecular distance r_{ij}^*.

finite time-step. The size of the time-step is a compromise between computational cost and simulation robustness: a small time-step will be less computationally efficient, while a large time-step risks numerical instability, by placing molecules in the highly-repulsive region of one another (which escalates throughout the system). In this thesis, a time-step of $\Delta t = 5.4$ fs is used[2], which has previously been utilised in other hybrid MD studies [Borg et al., 2013a,b]. Common integration techniques include the Leapfrog method [Hockney, 1970] and the Verlet methods [Verlet, 1967; Swope et al., 1982], owing to their high precision and low computational cost (only calculating the force once per time-step). In this thesis, the Velocity Verlet method [Swope et al., 1982] is used, which employs the following procedural algorithm for each time-step [Allen and Tildesley, 1987]:

1. The molecule velocities are calculated at the midpoint of the time-step:

$$\mathbf{v}_i\left(t + \frac{1}{2}\Delta t\right) = \mathbf{v}_i(t) + \frac{1}{2}\Delta t \mathbf{a}_i(t). \tag{1.7}$$

2. The molecules are advanced to their new position:

$$\mathbf{r}_i\left(t + \Delta t\right) = \mathbf{r}_i(t) + \Delta t \mathbf{v}_i\left(t + \frac{1}{2}\Delta t\right). \tag{1.8}$$

[2]This time-step size is also a numerical convenience because it makes the size of each write-interval (every 400 time-steps) equal to 1 in dimensionless units.

3. The forces and accelerations are calculated at the new time-step using equations (1.2), (1.5), and (1.6). The velocity move is completed:

$$\mathbf{v}_i\left(t+\Delta t\right)=\mathbf{v}_i\left(t+\frac{1}{2}\Delta t\right)+\frac{1}{2}\Delta t\mathbf{a}_i(t+\Delta t). \tag{1.9}$$

In this thesis, non-equilibrium MD simulations [Allen and Tildesley, 1987; Rapaport, 2004] are solved using the mdFoam solver [Macpherson and Reese, 2008; Borg et al., 2010] developed in OpenFOAM — an open-source set of C++ libraries for solving sets of differential equations in parallel (www.openfoam.org). Flows are driven by the application of an external body force $\mathbf{F}^{ext}$ to every molecule in a specified region of constant depth, such as a reservoir or a straight section of a channel. This body force is used to generate pressure jumps and represent linear pressure gradients in simulations (see Chapter 2 for details), and is accounted for by altering equation (1.6) to

$$\mathbf{F}_i+\mathbf{F}^{ext}=m_i\mathbf{a}_i. \tag{1.10}$$

Thermodynamic macroscopic properties, such as pressure, cannot be determined from the behaviour of a single molecule, but may be estimated by averaging over a large number of molecules in an ensemble, through the use of statistical mechanics [Hansen and McDonald, 2006]. As a statistical average, the macroscopic properties calculated will only equal the true properties of the system when the simulation time tends to infinity and the phase space is fully sampled. Therefore, when performing an MD simulation, the simulation time for a sufficient sample size is a compromise between the desired efficiency and accuracy. Details of how specific properties are calculated in MD have been documented by Borg [2010] and Nicholls [2012].

The four ensembles commonly used in MD are the microcanonical (constant-NVE), the canonical (constant-NVT), the grand canonical (constant-μVT), and the isothermal-isobaric (constant-NPT), where V is the volume, E is the total energy, T is the temperature, μ is the chemical potential, and P is the pressure [Allen and Tildesley, 1987]. For each ensemble, the noted thermodynamic variables are fixed. In this thesis, the canonical ensemble is used and the temperature is kept constant using a thermostat to remove energy (generated by the external body force) from the system. Popular models for maintaining a constant temperature include the Berendsen thermostat [Berendsen et al., 1984], the Nosé-Hoover thermostat [Nosé, 1984; Hoover, 1985], and the Anderson thermostat [Andersen, 1980]; in this thesis,

the Berendsen thermostat is used. This thermostat rescales the thermal velocities, minimising the impact on the stream-wise velocity. The velocities are modified by a factor χ:

$$\chi = \left[1 + \frac{\Delta t}{\tau_T}\left(\frac{T}{T_0} - 1\right)\right]^{1/2}, \tag{1.11}$$

where T is the target temperature, T_0 is the measured temperature, and τ_T is a time constant that defines the strength of coupling between the system and a hypothetical heat bath. The thermostat is implemented via localised bins over the entire MD domain in the streamwise and transverse flow directions. Each bin has a target temperature of $T = 292.8$ K (see Appendix A for the phase diagram of argon), using a time constant $\tau_T = 21.61$ fs.

Chapter 2

The General Networks Internal-flow Multiscale Method

A generalised version of the internal-flow multiscale method (IMM) is not trivial to implement and has far greater practical applicability than its serial predecessor, enabling the simulation of mixing and branching channel devices. An example of such a network is shown in Fig. 2.1. In this chapter, the methodology for the serial networks internal-flow multiscale method (SeN-IMM) [Borg et al., 2013b] is extended to encompass general network geometries (where each component can have any number of inlets and outlets) and incorporates an equation of state to account for fluid compressibility. Hereon, this new method is referred to as the general networks internal-flow multiscale method (GeN-IMM). The other flow assumptions for the SeN-IMM are maintained, i.e. the GeN-IMM is applicable only to low speed, low Reynolds number, isothermal and steady state flows. The GeN-IMM provides computational savings over a full molecular simulation in two ways: 1) high-aspect-ratio channels are replaced by hydrodynamically-equivalent short channel micro-elements, reducing the number of simulated molecules; and 2) due to their small size, these micro-elements reach steady state much faster than a simulation of the full network. Furthermore, as the micro-elements are small and can be simulated independently of one another during each iteration, the GeN-IMM is less dependent on access to supercomputer resources than a full molecular simulation. Micro-elements can be run on single graphics processing units (GPUs) whereas a full molecular simulation may require a large number of central processing units (CPUs) as there is often a limit to the number of molecules able to be processed on a GPU.

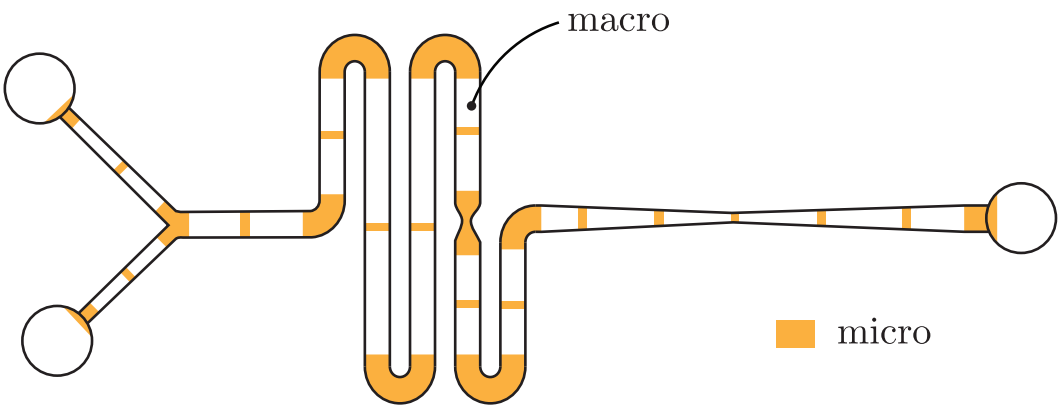

Figure 2.1: Schematic of a complex bifurcating network with high-aspect-ratio channels that can be solved by the GeN-IMM. The network is decomposed into components by adopting an IMM approach in the long channels and full molecular dynamics simulations of the junctions.

2.1 Methodology

A general fluidic network is decomposed into *components*, with each being defined as either a *junction* component or a *channel* component (see Fig. 2.2 for an illustrative example of such a decomposition). The main purpose of the decomposition is to enable the channel components to be simulated separately using short, periodic, and computationally cheaper micro-elements — this is the IMM approach. Each component has a number of 'inlet/outlet' *boundaries*; these are either *external boundaries* to the network, or *internal boundaries* which connect neighbouring components (see Fig. 2.2). To make the separate components consistent with conditions in the full network, the correct pressure values at all boundaries must be established. These must ensure that the mass flow rate ($\dot{m}$) and pressure (P) at all internal boundaries are consistent, and that the external pressure boundary conditions are satisfied, i.e.

$$\dot{m}_{i,p} = -\dot{m}_{j,q}, \tag{2.1}$$

$$P_{i,p} = P_{j,q}, \tag{2.2}$$

where i and j refer to a pair of connecting internal boundaries, from neighbouring components p and q, respectively, and

$$P_{i,q} = P_B, \tag{2.3}$$

where the subscript B denotes an external boundary condition on the i^{th} boundary of the q^{th} component. Note, by convention, the mass flow rate is treated as positive

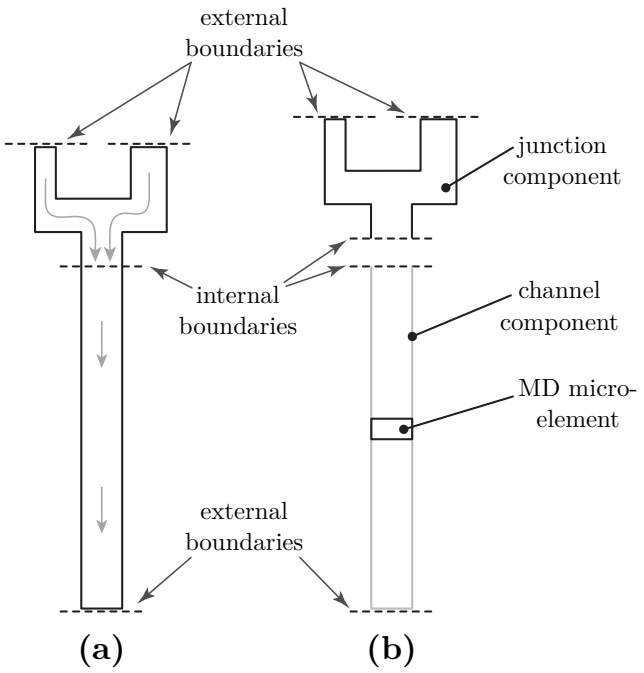

Figure 2.2: Schematics of **(a)** a simple Y-junction network with **(b)** the network decomposed into components; internal and external boundaries are highlighted.

flowing out of the component, hence the minus sign in equation (2.1).

In steady-state flows, the net mass flow rate through all boundaries of one component is zero:

$$\sum_{i=1}^{W_q} \dot{m}_{i,q} = 0, \tag{2.4}$$

where W_q is the total number of boundaries of the q^{th} component. This *local* mass conservation described in equation (2.4) is automatically guaranteed by any individual component simulation, but it is only in combination with equation (2.1) that *global* mass conservation is satisfied over the whole network.

The required pressure values are found iteratively, with successive estimations moving conditions closer to global mass conservation (within the constraints described above). To generate pressure values for the next iteration, a linear prediction of how mass flow rate varies in response to pressure changes is used:

$$\dot{m}_{i,q} - \sum_{j=1(\neq i)}^{W_q} \left(P_{i,q} - P_{j,q}\right) K_{ij,q} = \langle \dot{m}_{i,q} \rangle - \sum_{j=1(\neq i)}^{W_q} \left(\langle P_{i,q} \rangle - \langle P_{j,q} \rangle\right) K_{ij,q}\,, \tag{2.5}$$

where the terms in angle brackets are measurements extracted from component

MD simulations at the previous iteration; the terms $K_{ij,q}$ are flow-conductance coefficients between the boundaries i and j in component q. The flow-conductance coefficients can be estimated via either a presimulation (for details, see Appendix C), or from experience. Equation (2.5), in combination with equations (2.1)-(2.4), provides a system of linear equations with an equal number of unknowns. This system can be solved using a straightforward matrix inversion procedure (e.g. LU decomposition) to obtain values of pressure for the next iteration. Equation (2.5) ensures that as the component MD simulations approach global mass conservation (i.e. $\langle \dot{m}_{i,q} \rangle \rightarrow \dot{m}_{i,q}$) the values of pressure cease to be updated in subsequent iterations (i.e. $P_{i,q} \rightarrow \langle P_{i,q} \rangle$). Note, this converged result is independent of the flow-conductance coefficients ($K_{ij,q}$), which only affect the convergence rate and the approach to convergence.

Fluid compressibility in the network, due to large changes in pressure, is accounted for by modifying the number of molecules in each component MD simulation according to an empirical equation of state relating average mass density to the boundary pressures of the component. The empirical equation, which may be unique to each component, is a polynomial of the form

$$\bar{\rho}_q = \langle \bar{\rho}_q \rangle + \sum_{b=0}^{\beta} a_{b,q} \left(\bar{P}_q^b - \langle \bar{P}_q \rangle^b \right), \tag{2.6}$$

where $\bar{\rho}_q$ is the volume-averaged mass density in the q^{th} component, $a_{b,q}$ are predetermined constants, β is the order of the polynomial equation, and

$$\bar{P}_q = \frac{1}{W_q} \sum_{i=1}^{W_q} P_{i,q}, \tag{2.7}$$

where $P_{i,q}$ is the pressure at the i^{th} of W_q boundaries in the q^{th}component. As the flow is isothermal for all cases in this thesis, there is no temperature dependence in equation (2.6). The method used to determine the coefficients $a_{b,q}$ is outlined in Appendix D. Equation (2.6) enables an estimation to be made for the number of molecules that need to be added or removed for the next iteration of each component simulation (using the FADE algorithm of Borg et al. [2014], the USHER algorithm of Delgado-Buscalioni and Coveney [2003b], or the AdResS scheme of Praprotnik et al. [2005]). Equation (2.6) ensures that when the boundary pressures have converged, the mean mass density (and hence the number of molecules in each component) ceases to be updated for the next iteration.

Solving equations (2.1)-(2.5) provides the pressure values that satisfy external

boundary conditions, that are consistent at internal boundaries, and that create a mass-flow response that is closer to being globally conservative than that of the previous iteration. The method by which these boundary conditions are applied to the individual component simulations is now described.

2.1.1 Simulating channel components

The channel components, by definition, are highly scale separated and can thus be simulated using shorter MD micro-elements (which is the same as the IMM procedure of Borg et al. [2013a] and Patronis et al. [2013]). In the example of Fig. 2.2(b), the channel has a uniform cross-section in the streamwise direction. Therefore, given the assumption that the pressure variation is approximately linear along the entire channel length L, it is sufficient to model the channel using a shorter periodic MD micro-element of length L' with a uniform cross-sectional area, as shown in Fig. 2.3. A weak streamwise pressure gradient is hydrodynamically equivalent to

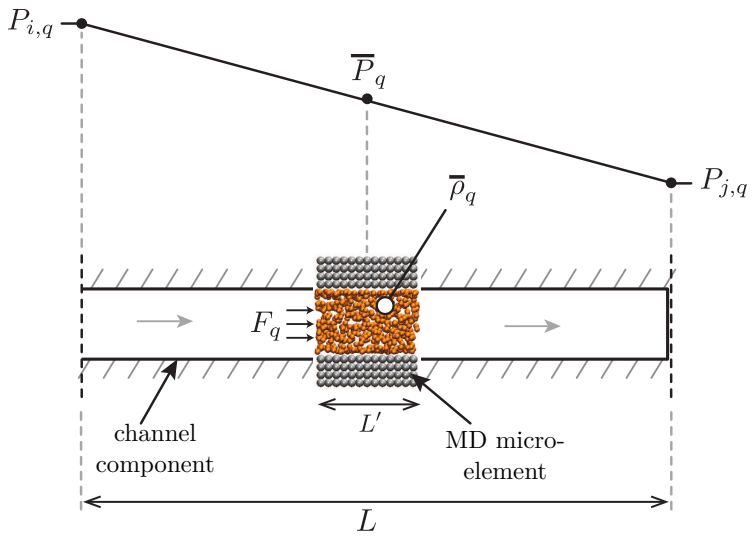

Figure 2.3: Schematic of the channel component from Fig. 2.2, demonstrating how a shorter micro-element MD simulation is used to represent the original channel.

a constant streamwise body force because the momentum flux produced is identical. As such, the pressure drop across a long channel can be simulated by applying a uniform body force F_q to all fluid molecules in a periodic MD channel of arbitrary length. Using a central-difference approximation:

$$F_q = \frac{(P_{i,q} - P_{j,q})m}{\bar{\rho}_q L}, \tag{2.8}$$

where m is the mass of a single molecule, and the direction of a positive force is from boundary i to boundary j. The computational savings accrued by using small MD micro-elements to model high-aspect-ratio channel components is the main source of speed-up in the GeN-IMM, and is roughly proportional to L/L' for these components.

In certain fluid cases (commonly in rarefied gases [Huang et al., 2007]), the pressure distribution along long channels can be non-linear. In these instances, the channel component is divided into multiple MD micro-elements, such that the combination of the linear pressure gradients over each micro-element is a good approximation of the overall pressure variation (see Borg et al. [2013a]; Patronis et al. [2013]; Patronis and Lockerby [2014]).

2.1.2 Simulating junction components

Junction components, unlike channels, cannot be represented using smaller MD simulations; there is no obvious scale separation that can be exploited, so the full component must be simulated. However, what is not straightforward in MD is how to deal with the non-periodicity of most junction components (e.g. the Y-junction in Fig. 2.2). There are no available MD ensembles to solve non-periodicity, even though a significant amount of progress has been made on developing artificial non-periodic boundary conditions (NPBCs). See Mohamed and Mohamad [2009] and the references therein for more details.

This problem is circumvented by introducing an artificial region attached to the main component, which enables convenient periodic boundary conditions (PBCs) to be used, as shown in Fig. 2.4. This means that, for junction components, the MD micro-element is comprised of the component (or the 'real' region) and the artificial region. The correct pressure boundary conditions for the real region are established by applying body forces in localised regions of constant cross-section within the artificial region. These body forces create sharp jumps in pressure $\Phi_{i,q}$ and introduce more unknowns into the system of equations. As in equation (2.5), these body forces are determined iteratively by making a linear prediction of how the mass flow rate and pressure in the real domain will be affected by the body-force-generated pressure jumps $\Phi_{i,q}$:

$$\dot{m}_{i,q} + \sum_{j=1(\neq i)}^{W_q} \Delta P_{ij,q} D_{ij,q} = \langle \dot{m}_{i,q} \rangle + \sum_{j=1(\neq i)}^{W_q} \langle \Delta P_{ij,q} \rangle D_{ij,q} \,, \tag{2.9}$$

where $\Delta P_{ij,q} = (P_{i,q} - \Phi_{i,q}) - (P_{j,q} - \Phi_{j,q})$, $D_{ij,q}$ are flow-conductance coefficients,

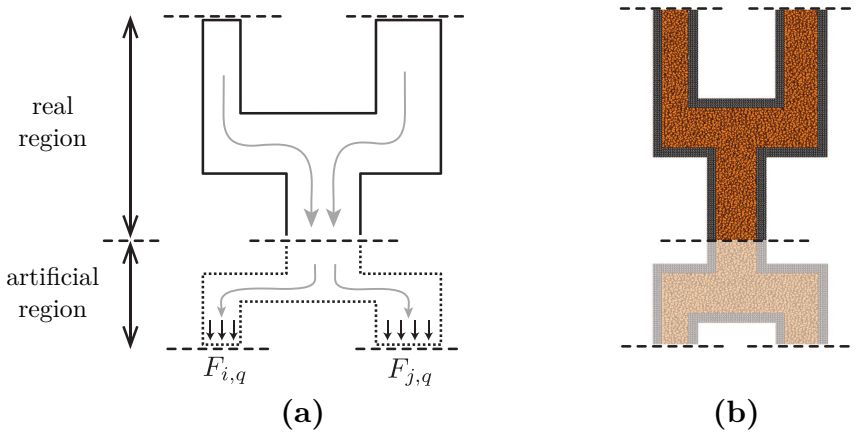

Figure 2.4: Schematics of **(a)** the junction component from Fig. 2.2 with body forces $F_{i,q}$ and $F_{j,q}$ applied in the artificial region, and **(b)** the periodic MD micro-element simulation setup of the same component.

and the angular brackets denote a measurement extracted from the MD simulation at the previous iteration. The exact relationship between the body forces $F_{i,q}$ and pressure jumps $\Phi_{i,q}$ is given in Appendix E. There is a sign differences between equations (2.5) and (2.9) because the mass flow rate at a boundary is treated as being positive if it flows out of the component.

At one boundary in each component (chosen arbitrarily) no body force is applied, i.e. $\Phi_{1,q} = 0$, so as not to over-constrain the simulation.

2.1.3 Algorithm

The iterative algorithm for the GeN-IMM is as follows:

1. Approximate the flow-conductance coefficients $K_{ij,q}$ and $D_{ij,q}$ for each component. The terms in angular brackets in equations (2.5) and (2.9) are assumed to be zero.

2. Solve the set of linear equations (2.1) - (2.5) and (2.9), using matrix inversion, for the predicted mass flow rates $\dot{m}_{i,q}$, pressures $P_{i,q}$, and junction pressure jumps $\Phi_{i,q}$.

3. Solve equation (2.6) for the mean mass densities $\bar{\rho}_q$ in all components. If this is the first iteration, the terms in angle brackets are assumed to be zero.

4. Solve (2.8) for the channel component body forces F_q, using the predicted values of pressure $P_{i,q}$ and ρ_q previously calculated.

5. Run all micro-element MD simulations with the new body forces and updated average densities until steady state. At steady state, measure the time-averaged mass flow rate $\langle \dot{m}_{i,q} \rangle$ at every boundary. In addition, for junctions measure the pressure $\langle P_{i,q} \rangle$ at every boundary, and for channels measure the mean pressure $\langle \bar{P}_q \rangle$ over the micro-element. These measured properties are used in equations (2.5), (2.6), and (2.9) for the next iteration. Note, for channel components, the term $(P_{i,q} - P_{j,q})$ is obtained directly from equation (2.8).

6. Update the flow-conductance coefficients $K_{ij,q}$ and $D_{ij,q}$.

7. Repeat from step 2 until a convergence criterion is met for the mass flow rate at a given boundary:

$$\zeta_{i,q} < \zeta^{\text{tol}}, \quad \text{with} \quad \zeta_{i,q} = \left| \frac{[\dot{m}_{i,q}]_l - [\dot{m}_{i,q}]_{l-1}}{[\dot{m}_{i,q}]_l} \right|. \tag{2.10}$$

   Here, ζ^{tol} is a predetermined convergence tolerance and the superscripts l and $l-1$ denote values calculated at the current and the previous iteration, respectively.

2.2 Results and discussion

The GeN-IMM is tested on compressible pressure-driven flows through some simple network configurations. Due to the statistical noise created by thermal fluctuations, large pressure gradients are required in MD simulations [Koplik et al., 1988; Travis et al., 1997] in order to achieve sufficiently low-variance data within a reasonable time frame.

The GeN-IMM results are verified via comparison to a full MD simulation of the entire network. In this way, any approximations made within the MD model are negated as they are the same in both the full and the hybrid cases. The pressure drops over the full MD networks are generated in the same manner as for junction micro-elements, i.e. through the application of body forces in an artificial region (the shaded region in Fig. 2.5c). The networks are restricted to a relatively small size in order that these full MD simulations are not too computationally expensive. All MD simulations are three-dimensional, with periodic boundary conditions (PBCs) applied in every direction. The cases are all set up so that there are no gradients of properties in one direction perpendicular to the flow; thus, the depth is chosen as a compromise between computational efficiency and the ability to generate sufficient data to calculate macroscopic properties. The full MD simulations are run in parallel

on 48 CPUs, while the MD micro-elements for the GeN-IMM solution are run on single GPUs.

The first network analysed is a straight channel connecting two reservoirs, i.e. a serial network, which is similar to a test case in Borg et al. [2013b]; the second network is a bifurcating channel, i.e. a general network, which demonstrates the novel capabilities of GeN-IMM.

2.2.1 A straight channel network

The configuration of the first network is a relatively long, straight nanochannel connecting an inlet reservoir to an outlet reservoir, as shown in Fig. 2.5a. Figure 2.5b shows the hybrid decomposition, consisting of three micro-elements: an inlet reservoir, a short channel to represent the long channel, and an outlet reservoir. The length of the entrance/exit channel sections of the reservoir micro-elements has been chosen conservatively to be roughly twice the channel flow entrance length from laminar macroscopic flow theory. This ensures the flow in micro-element #2 is fully developed and is not affected by expansion/contraction effects. The length of the channel component is $L = 102$ nm, which is represented in the multiscale model by a micro-element of length $L' = 4.08$ nm (see Appendix B for justification), producing a length ratio of $L/L' = 25$. The wall-wall height of the channel section is 3.4 nm, which is sufficiently small that there is non-continuum/non-equilibrium flow behaviour in the LJ fluid argon (e.g. molecular layering and velocity slip at the fluid-solid interface) that would not be effectively captured by a standard Navier-Stokes fluid dynamics solution. The reservoir height (in the y-direction) is 6.8 nm. The depth (in the z-direction) is a uniform 6.8 nm for the full network and each micro-element. A large pressure drop of ≈ 350 MPa is imposed over the network for the reason described above. The external boundary conditions for this network geometry are: boundary #1 (inlet) pressure $P_1 = 648$ MPa, and boundary #6 (outlet) pressure $P_6 = 295$ MPa.

(a) Multiscaled Network

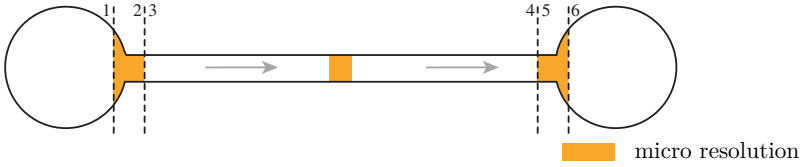

(b) Hybrid Simulation

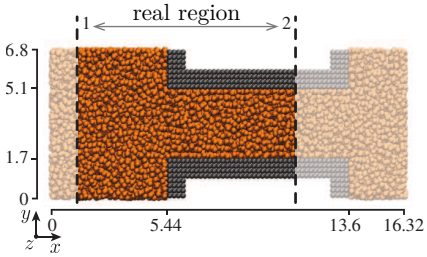

(i) MD micro-element #1: inlet reservoir

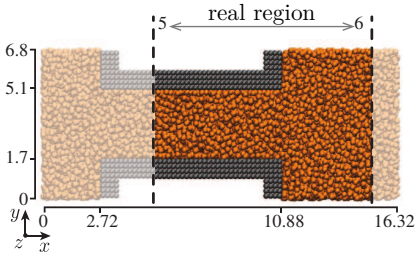

(iii) MD micro-element #3: outlet reservoir

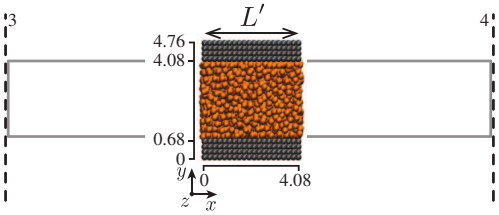

(ii) MD micro-element #2: channel

(c) Full MD Simulation

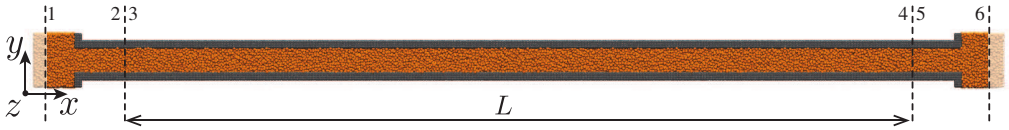

Figure 2.5: **(a)** Schematic of the straight channel multiscale network, with **(b)** the hybrid MD GeN-IMM decomposition, and **(c)** the full MD network setup. Dimensions are in nanometers. The boundary numbers are labelled above each image.

Table 2.1: Initial flow-conductance coefficients $K_{ij,q}$ and $D_{ij,q}$ for the straight channel network.

Component # q	Boundary # i,j	Flow-conductance coefficient $K_{ij,q}$ ($\times 10^{-20}$ m·s)	$D_{ij,q}$ ($\times 10^{-20}$ m·s)
1	1,2	-4.2866	-10.7081
2	3,4	-1.0708	-
3	5,6	-6.2154	-6.8168

The initial estimates of $K_{ij,q}$ and $D_{ij,q}$ are presented in Table 2.1. There is no value of $D_{ij,q}$ for component #2 because those coefficients are only required for junction components.

The iterative algorithm previously outlined is performed for five iterations (although convergence occurs in fewer) to illustrate the numerical stability of the method. Fig. 2.6 shows how the mass flow rate and pressure measurements (from MD simulations) develop with iteration number at boundaries #3 and #4, where there are no external boundary conditions. There is quick and accurate convergence of the GeN-IMM solution to the full MD result, and good numerical stability. This is expected as, once global mass conservation is reached, the pressures at boundaries (which dictate the magnitude of the density and external body forces) cease to be updated — so simulations in subsequent iterations will have approximately the same input parameters. The fluctuation of the mass flow rates between iterations 2 and 5 in Fig. 2.6a and Fig. 2.6c are of similar magnitude to the error bars, so can be accounted for by the noise inherent in the MD simulations. The error bars for both the full and hybrid solutions are 1.96 standard deviations either side of the mean to represent the 95% confidence level, and take into account the amount of correlation that occurs between molecules within the relevant micro-element or network.

Complete results demonstrating the precision and convergence speed of the GeN-IMM for the straight channel network are detailed in Tables 2.2 and 2.3, and Fig. 2.7, respectively. In the tables, the reference mass flow rate $\dot{m}_R$ and reference pressure P_R are respectively the largest mass flow rate and pressure measured in the GeN-IMM MD simulations, as it is these values that most strongly govern the flow characteristics. The final error in the GeN-IMM solution is $\approx 1\%$ at all boundaries for both mass flux and pressure. This can be compared to a relative error of 73% for the initial mass flow rate prediction. Setting a fairly tight tolerance of $\zeta^{\text{tol}} = 0.02$, the GeN-IMM solution converges within three iterations, as shown in Fig. 2.7.

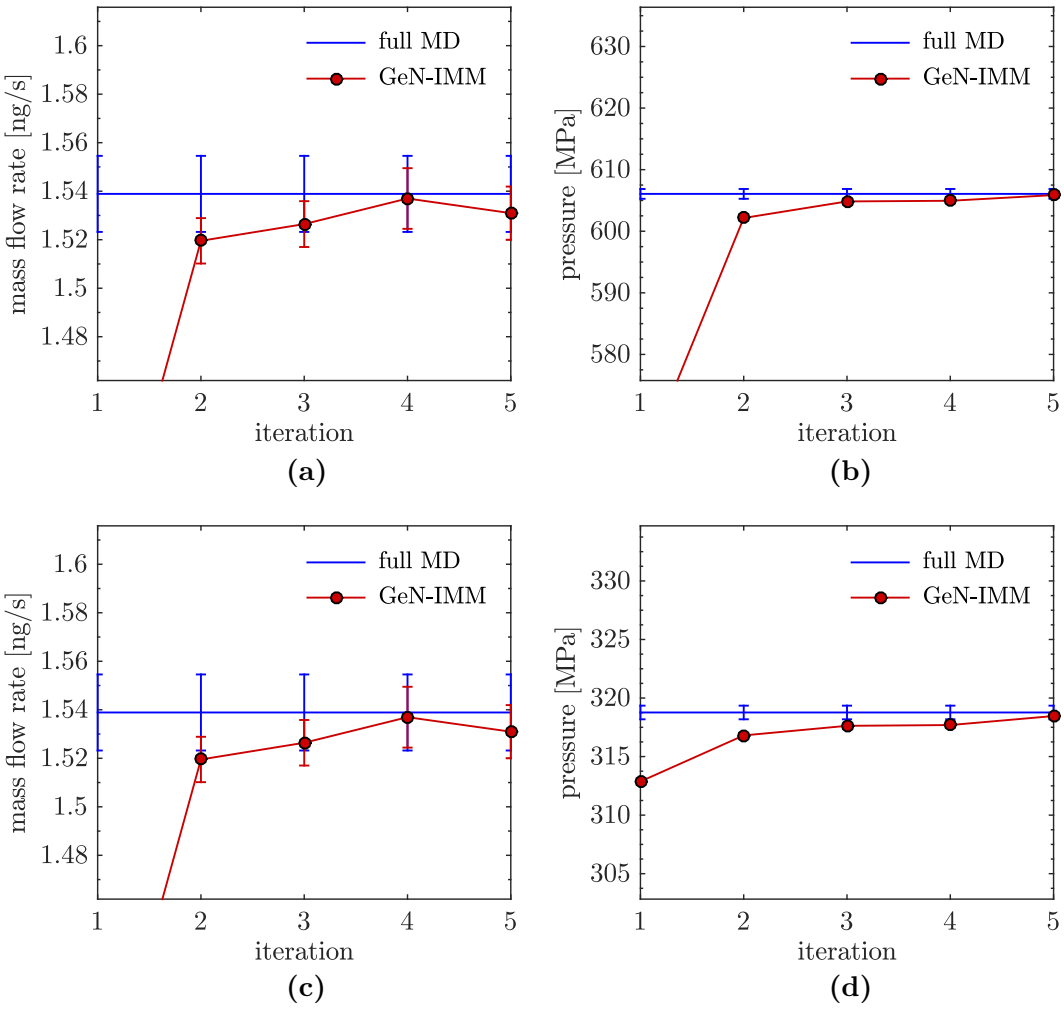

Figure 2.6: Straight channel network: GeN-IMM MD micro-element measurements of mass flow rate and pressure at boundaries #3 **(a & b)** and #4 **(c & d)**, respectively, progressing with number of iterations. The pressure error bars are smaller than the size of the symbol used. Comparisons are made with the results from a full MD simulation of the same network.

Table 2.2: Straight channel network: mass flow rate measurements for the GeN-IMM MD micro-elements (iteration 5) and the full MD solution. Relative error calculated as $|\dot{m}_F - \dot{m}_i|/|\dot{m}_R| \times 100$.

Boundary #	Full MD $\dot{m}_F$ (ng/s)	GeN-IMM $\dot{m}_i$ (ng/s)	Relative error e_i (%)
1	1.5389	1.5227	1.04
2	1.5387	1.5226	1.04
3	1.5389	1.5310	0.51
4	1.5389	1.5310	0.51
5	1.5389	1.5461	0.46
6	1.5387	1.5461	0.48

Table 2.3: Straight channel network: pressure measurements at for the GeN-IMM MD micro-elements (iteration 5) and the full MD solution. Relative error calculated as $|P_F - P_i|/|P_R| \times 100$.

Boundary #	Full MD P_F (MPa)	GeN-IMM P_i (MPa)	Relative error e_i (%)
1	648.01	647.99	0.00
2	606.07	604.81	0.19
3	606.07	605.70	0.03
4	318.77	318.63	0.05
5	318.77	317.68	0.17
6	295.06	295.28	0.03

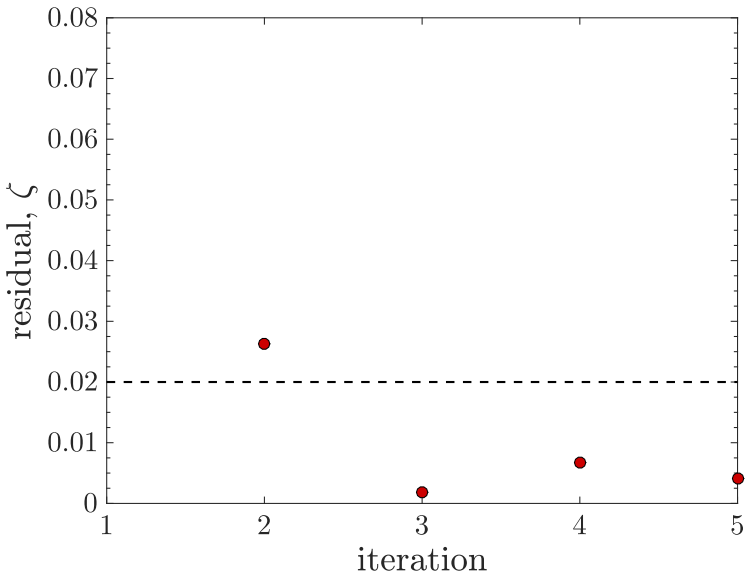

Figure 2.7: Convergence of the GeN-IMM for the straight channel network. The horizontal line is the prescribed tolerance ζ^{tol}.

To ensure that the hybrid solution is accurately representing the full MD system, longitudinal and transverse profiles are examined by measuring macroscopic properties in bins. All GeN-IMM profiles are plotted at iteration 5. Figure 2.8 shows the measured streamwise pressure and density profiles for the straight channel network. It is clear that the profiles for the junction micro-elements at the inlet and outlet (micro-elements #1 and #3, respectively) are in good agreement with the results from the full MD simulation. As the mass flow rate through these micro-elements is also in agreement with the full MD results, this suggests that the entrance/exit length chosen is sufficient for fully-developed flow. As outlined in the methodology, for the channel micro-element (#2), a body force is applied over the MD domain that is proportional to the required pressure gradient, and the boundary pressures are then extrapolated from the central point in the channel. As such, the GeN-IMM solution pressure profile in the channel section is linear. Evidently, from Figure 2.8, this is not so for the full MD simulation — although it seems to have had little impact on the overall accuracy of the method, suggesting that the linear approximation is acceptable, at least for this network.

Figure 2.9 presents the transverse profiles of streamwise velocity and density for the straight channel network. As shown in Fig. 2.9a, these profiles are measured at the half way point along the network, at the plane A-A — i.e. the profiles for the GeN-IMM solution are obtained from measurements in micro-element #2. Once again, excellent agreement between the solutions is found, including the accu-

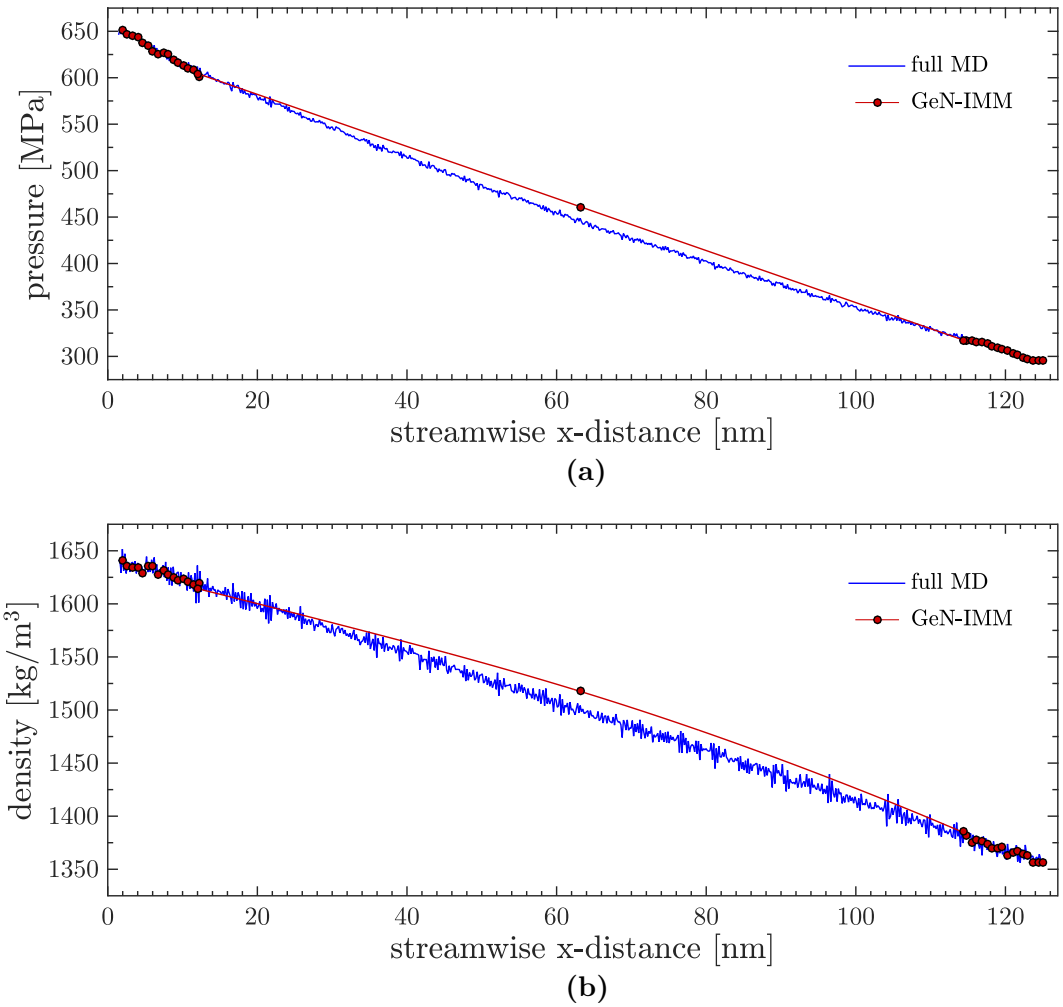

Figure 2.8: Straight channel network: longitudinal profiles of **(a)** pressure and **(b)** density (averaged over the cross-section). Measured in the GeN-IMM MD micro-elements (at iteration 5) and the full MD simulation. The GeN-IMM density profile in the channel section is generated using the equation of state (2.6)

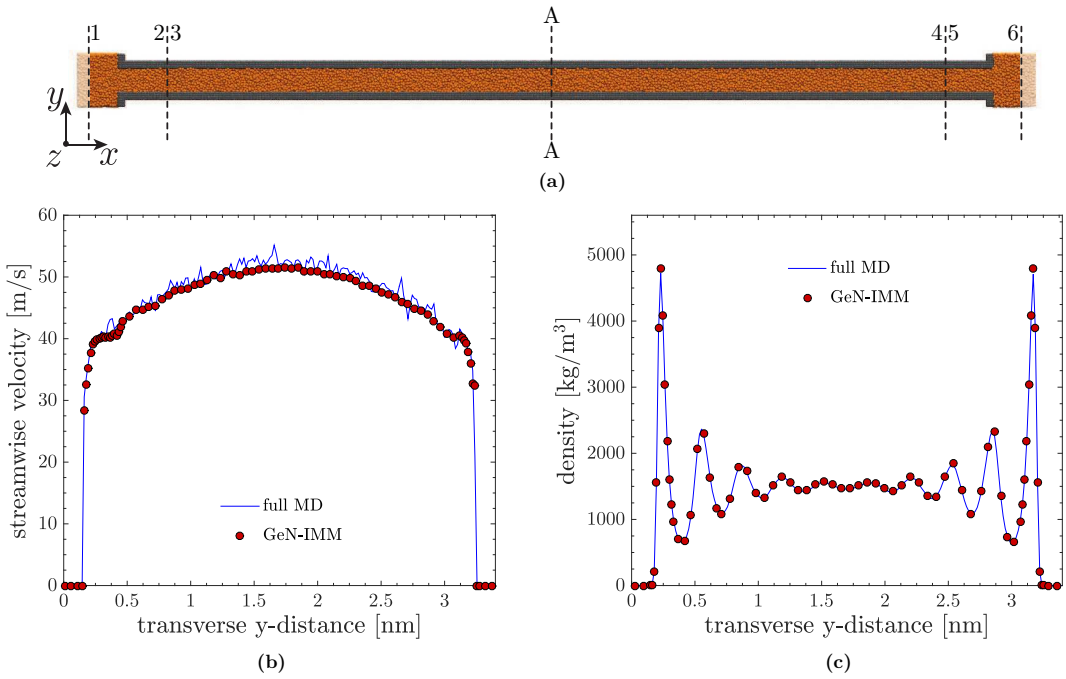

Figure 2.9: Straight channel network: **(a)** schematic showing the location of plane A-A; transverse profiles of **(b)** streamwise velocity and **(c)** density. Measured in the GeN-IMM MD micro-elements (at iteration 5) and the full MD simulation.

rate capturing of non-continuum/non-equilibrium effects, namely velocity slip and molecular layering in the velocity and density profiles, respectively. In Fig. 2.9, the data from the full MD simulation appears to contain a higher level of oscillation than the data from the GeN-IMM micro-element. This phenomenon is not due to any physical discrepancy between the full MD and channel micro-element simulations; it is owing to the small domain size of the micro-element. This enabled the macroscopic properties to be averaged over a longer time-period for little computational expense.

While accuracy is important, hybrid methods also need to show improved computational efficiency over a full molecular simulation. Computational speed-up is measured by comparing the product of the total number of time-steps and the average simulation time for one time-step, for both the full MD simulation and the GeN-IMM solution — τ_F and τ_G, respectively. The total number of time-steps is considered to be the number of time-steps taken for the hybrid solution to exhibit the same level of error as the full network solution, and the time taken to reach steady state is included within the measurement time. For a fair comparison, the average simulation time for one time-step was calculated by running each micro-element and

the full network on one CPU. The full MD simulation was run for approximately 1400000 time-steps, costing 9.4 seconds in computational time per time-step. The micro-elements for the hybrid solution were run for between $800000 - 1200000$ time-steps per iteration, costing between $0.2 - 0.65$ seconds per time-step. Assuming three iterations for convergence, the speed-up τ_F/τ_G is calculated to be 3.9. This is smaller than the value of 7.6 calculated by Borg et al. [2013b] for a similar network because that paper combined the two reservoir micro-elements into one, avoiding the need for artificial regions. While this is a useful technique, it is highly specific to the geometry of the network, requiring a serial network with junction components at both the inlet and the outlet. Here, we have relaxed this requirement in order to construct a more general technique. In Borg et al. [2013b], the channel height is also slightly greater, so the length-scale separation exploited in component #2 provides greater time savings (relative to the entire network) than in the present study.

Although the speed-up is fairly modest, it should be noted that this test network uses a channel length of only 102 nm and is presented in order to determine the accuracy of the hybrid method. A very large network would have rendered a full MD simulation computationally intractable. The computational speed-up is expected to increase dramatically as the scale-separation and size of the network increases as the number on micro-elements required to simulate channel components will likely increase at a slower rate than the size of the channel. This can be inferred from the fact that, in the even when the longitudinal pressure distribution is not accurately captured by the micro-element(s), the comparative error to the full MD solution is still very small. For example, if the channel component of the same network was 3 μm long and could be modelled by a single micro-element, the speed-up of the GeN-IMM over the full MD simulation would be approximately 100-fold.

For completion, the GeN-IMM solution for the straight channel network is considered with the channel component modelled by two micro-elements. In effect, the original channel is divided into equally in two, with each smaller component modelled by one micro-element. Figure 2.10 shows the new description of the component boundaries and the longitudinal pressure and density profiles for this configuration. Increasing the number of channel components shows a noticeable improvement in the accuracy of the longitudinal profiles to that of the full MD solution. However, convergence still requires three iterations and the accuracy of the mass flow rate measurement is not improved upon. Furthermore, the addition of an extra micro-element reduces the computational speed-up over the full MD simulation to 3.2.

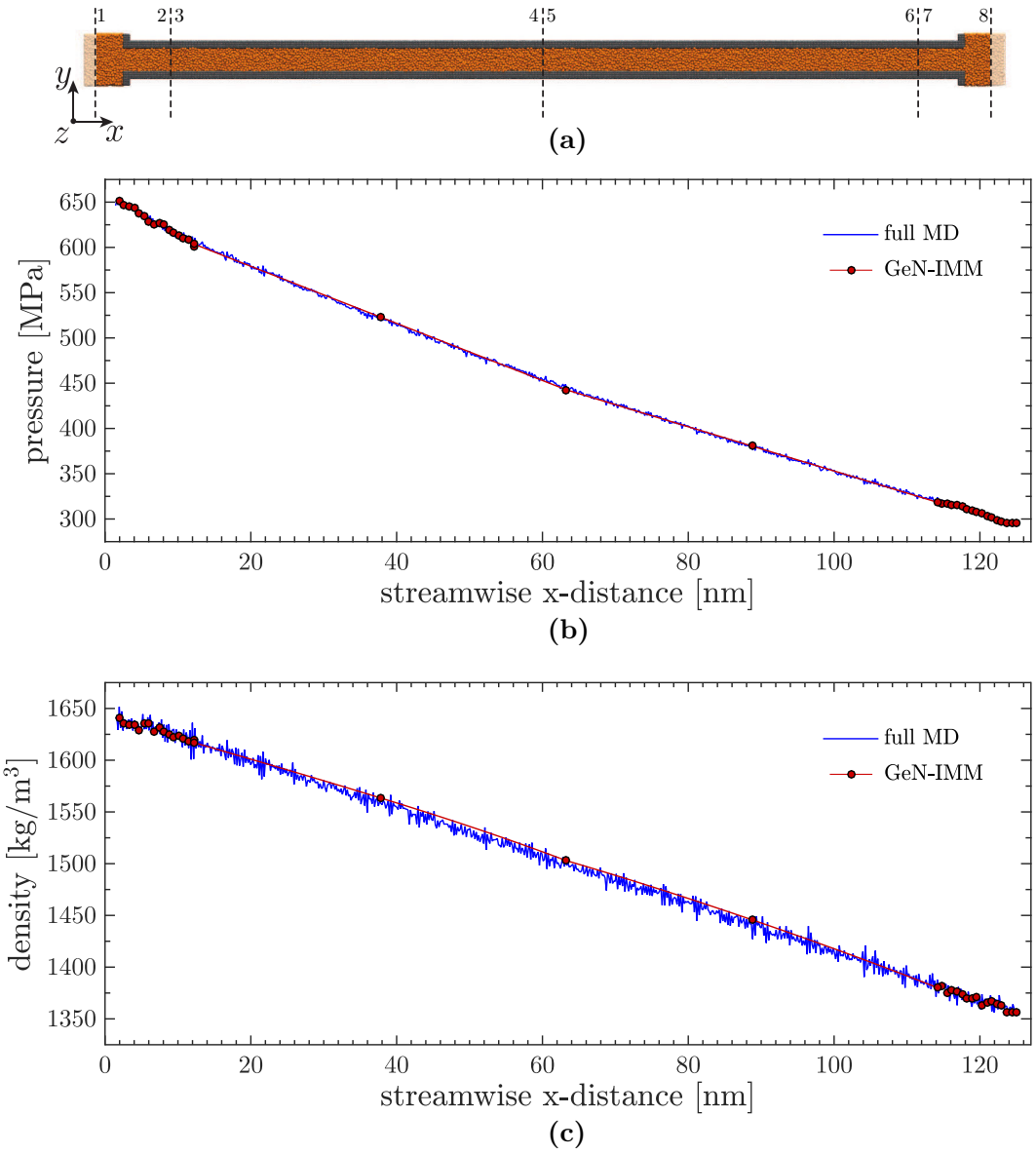

Figure 2.10: Straight channel network: **(a)** boundary locations using two micro-elements for component #2; longitudinal profiles of **(b)** pressure and **(c)** density (averaged over the cross-section). Measured in the GeN-IMM MD micro-elements (at iteration 5) and the full MD simulation. The GeN-IMM density profile in the channel section is generated using the equation of state (2.6)

2.2.2 A bifurcating channel network

The second network considered is a bifurcating channel, a configuration that has not previously been open to a hybrid solution. To further demonstrate the generality of the GeN-IMM, two test cases are solved for this network: 1) a bifurcating case (B1) which has an inlet at boundary #1, $P_1 = 565$ MPa, and outlets at boundaries #7, $P_7 = 135$ MPa, and #9, $P_9 = 140$ MPa; and 2) a mixing case (B2), which has inlets at boundaries #1, $P_1 = 427$ MPa, and #7, $P_7 = 699$ MPa, and an outlet at boundary #9, $P_9 = 46$ MPa. The network, along with its hybrid decomposition and the full MD setup (for verification purposes) are shown in Fig. 2.11.

The network is split into four components: three channel components at the inlets/outlets, and one bifurcating junction component linking them. The lengths of the entrance/exit channel sections of the Y-junction micro-element are ≈ 6 nm in both the real and artificial regions. This size has been chosen conservatively to be at least four times the largest channel flow entrance length calculated from laminar macroscopic flow theory for these cases (see Appendix F for more detail). It is also greater than the MD development length calculated using a root mean square deviation approach by Borg et al. [2013b] ($\approx 2 - 4$ nm) for similar channel sizes. This ensures that the flow in the channel components and connecting parts of the Y-junction is fully developed and will not introduce any artificial disturbances into the multiscale model[1]. Each channel component has a length of $L_1 = L_2 = L_3 = 68$ nm, while the corresponding MD micro-elements in the hybrid method are once again $L'_1 = L'_2 = L'_3 = 4.08$ nm. This produces length ratios of $L/L' = 16.7$. To add to the complexity and make the solution less apparent, the heights of the channel components (and therefore micro-elements) are all different: 4.08 nm, 2.72 nm, and 3.40 nm for micro-elements #1, #3 and #4, respectively. All micro-elements and the full MD network have a depth in the z-direction of 5.44 nm. This is smaller than the depth of the straight channel network to ensure that the full MD simulation is computationally tractable, as the other dimensions of the bifurcating network are much larger. The initial flow-conductance coefficients $K_{ij,q}$ and $D_{ij,q}$ for the bifurcating network cases are displayed in Table 2.4.

For both cases B1 and B2, convergence occurred within three iterations to a tolerance $\zeta^{\text{tol}} = 0.02$, as shown in Fig. 2.12. For each case their are three plots because there are three different mass flow rates required to converge, one for each

[1]It is possible that a smaller junction micro-element could produce fully developed flow and better computational savings. However, extra simulations would need to be performed for each new geometrical and thermodynamic setup to optimise the size of the junction components, and this would severely reduce the speed-up. So, it was deemed more pragmatic to use a conservative estimate from laminar macroscopic theory.

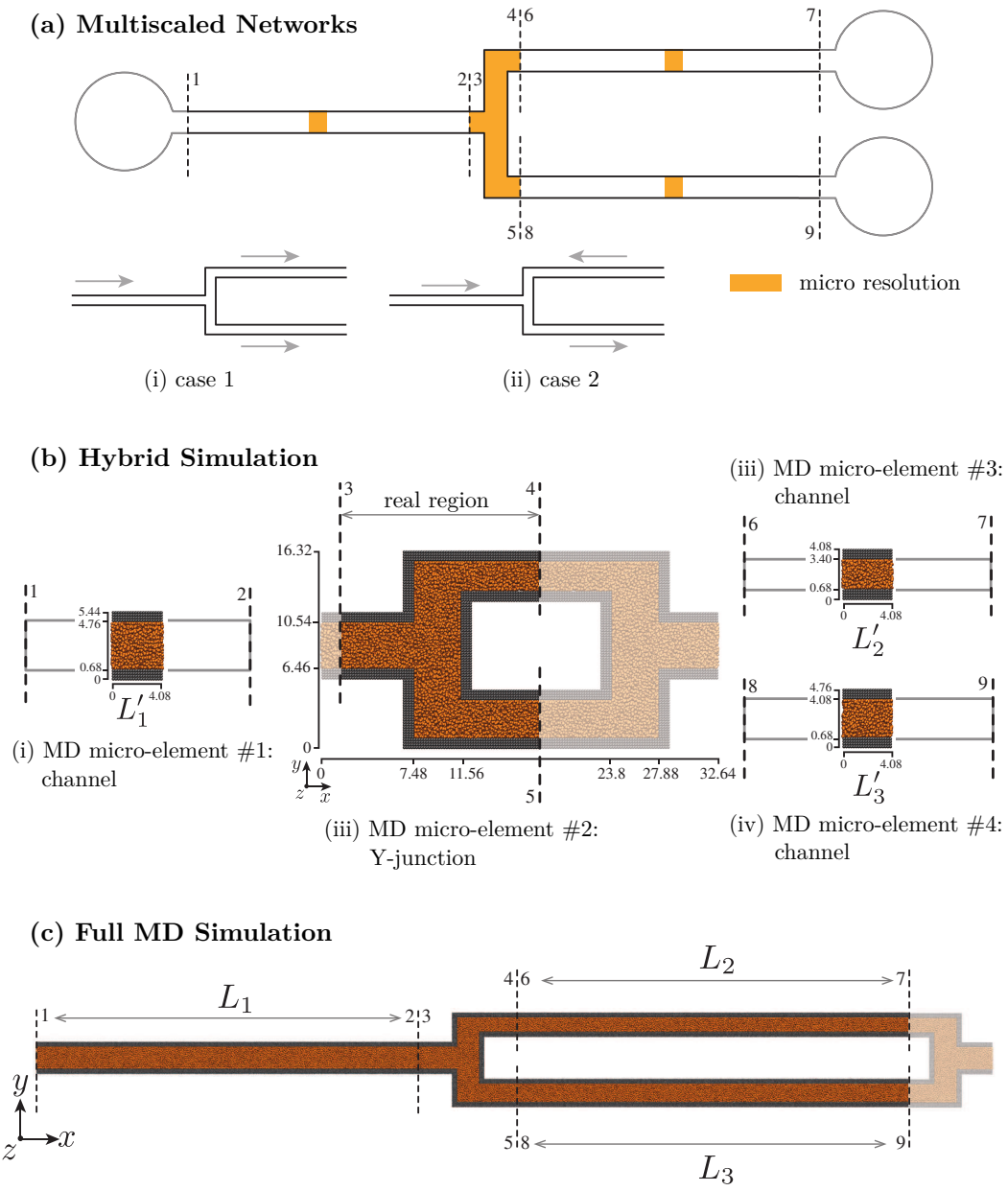

Figure 2.11: **(a)** Schematic of the bifurcating channel multiscale network and its two flow cases with **(b)** the hybrid GeN-IMM decomposition and **(c)** the full MD setup. Dimensions are in nanometers. The boundary numbers are also labelled in each image.

Table 2.4: Initial flow-conductance coefficients $K_{ij,q}$ and $D_{ij,q}$ for the bifurcating channel network.

Component # q	Boundary # i,j	Flow-conductance coefficient $K_{ij,q}$ ($\times 10^{-20}$ m·s)	$D_{ij,q}$ ($\times 10^{-20}$ m·s)
1	1,2	-1.7281	-
2	3,4	-1.4744	-1.5141
2	3,5	-2.0921	-2.0047
2	4,5	-0.6242	-0.8408
3	6,7	-0.7349	-
4	8,9	-1.1581	-

channel. For all channels, case B1 converges faster and to a lower tolerance than case B2: the residual being under 0.01 after three iterations.

The speed-ups for the bifurcating network cases are relatively low. The full MD simulation was run for approximately 1400000 time-steps, costing 14.3 and 13.4 seconds per time-step for cases B1 and B2, respectively. The micro-elements for the GeN-IMM solution were run for $800000 - 1200000$ time-steps per iteration, costing $0.2 - 3.0$ seconds per time-step. This leads to $\tau_F/\tau_G = 2.1$ for case B1 and $\tau_F/\tau_G = 2.0$ for case B2. The complex geometry shows the disadvantage of using PBCs in

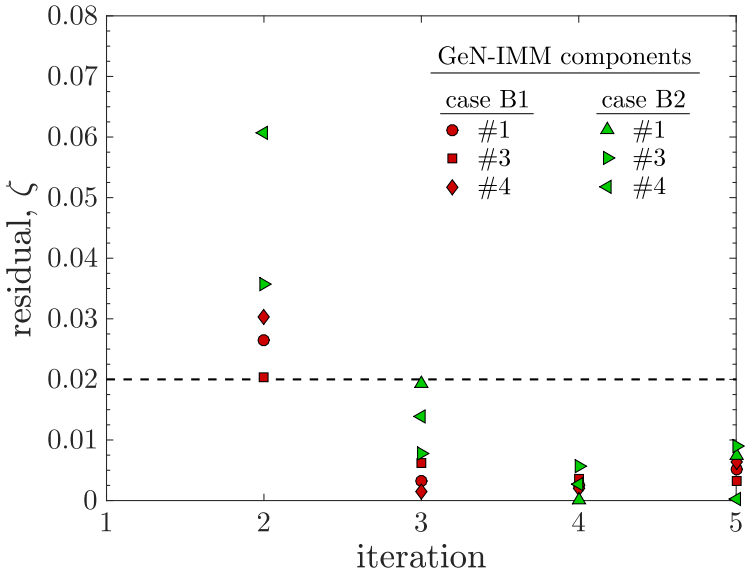

Figure 2.12: Convergence of the GeN-IMM for the bifurcating channel network: cases B1 and B2. The horizontal line is the prescribed tolerance ζ^{tol}.

MD. Although physically simple, the necessity for a mirroring boundary leads to a large artificial region that is costly to simulate, especially across multiple iterations. The exploitation of length-scale separation had to be minimised in these test cases to ensure that the full network could be simulated (for verification purposes) within a reasonable time.

It should be noted that, although the method is demonstrated here using MD as the micro solver, it is potentially compatible with any other micro solver, such as the direct simulation Monte Carlo (DSMC) method for gas flows, where NPBCs are better developed. Using a different micro solver may therefore remove the need for an artificial region and dramatically increase the speed-up in networks such as this. The complete results for case B1, the bifurcating configuration, are now presented, followed by those for case B2, the mixing configuration.

Case B1 - bifurcating configuration

The mass flow rate and pressure data for case B1 are shown in Tables 2.5 and 2.6, respectively. Again, good accuracy is seen, with the mass flow rate errors being less than 2%, and the pressure errors being mostly less than 1%, compared to an initial prediction error of 31%. These are slightly larger than those seen in the straight channel network, but that is to be expected as a more complex network will have fewer components directly constrained by the boundary conditions and small errors will accumulate.

Table 2.5: Bifurcating network case B1: mass flow rate measurements for the GeN-IMM MD micro-elements (iteration 5) and the full MD solution. Relative error calculated as $|\dot{m}_F - \dot{m}_i|/|\dot{m}_R| \times 100$.

Boundary #	Full MD $\dot{m}_F$ (ng/s)	GeN-IMM $\dot{m}_i$ (ng/s)	Relative error e_i (%)
1	2.3942	2.3627	1.32
2	2.3942	2.3627	1.32
3	2.3942	2.3535	1.70
4	0.9258	0.9115	1.55
5	1.4691	1.4416	1.88
6	0.9258	0.9133	1.36
7	0.9258	0.9133	1.35
8	1.4691	1.4465	1.54
9	1.4691	1.4464	1.54

Table 2.6: Bifurcating network case B1: pressure rate measurements for the GeN-IMM MD micro-elements (iteration 5) and the full MD solution. Relative error calculated as $|P_F - P_i|/|P_R| \times 100$.

Boundary #	Full MD P_F (MPa)	GeN-IMM P_i (MPa)	Relative error e_i (%)
1	564.84	564.46	0.07
2	332.28	334.01	0.31
3	332.28	333.86	0.28
4	262.71	267.86	0.91
5	257.16	262.01	0.86
6	262.71	268.57	1.04
7	135.38	135.75	0.07
8	257.16	261.89	0.84
9	139.64	139.53	0.02

The longitudinal pressure and density profiles are presented in Fig. 2.13. As with the straight channel network, the GeN-IMM solution shows strong agreement with the full MD result in the junction component. Along the channel components, the GeN-IMM solution assumes a linear pressure distribution which is not quite the case in the full MD simulation, but gives a close approximation. For case B1, the size of the two outlet pressure boundary conditions are very similar, so the outlet pressure and density profiles in Fig. 2.13 overlap somewhat.

The non-continuum/non-equilibrium fluid phenomena (i.e. velocity slip and molecule layering) seen in the full MD simulation are again accurately replicated in all the GeN-IMM channel micro-elements. Transverse profile of streamwise velocity and density are plotted at the channel midpoints in Fig. 2.14 (with GeN-IMM profiles measured in micro-elements #1, #3, and #4), and at the internal boundaries in Fig. 2.15 (with GeN-IMM profiles measured in micro-elements #2) to further demonstrate that the entrance/exit lengths of component #2 are adequate to enable fully-developed flow.

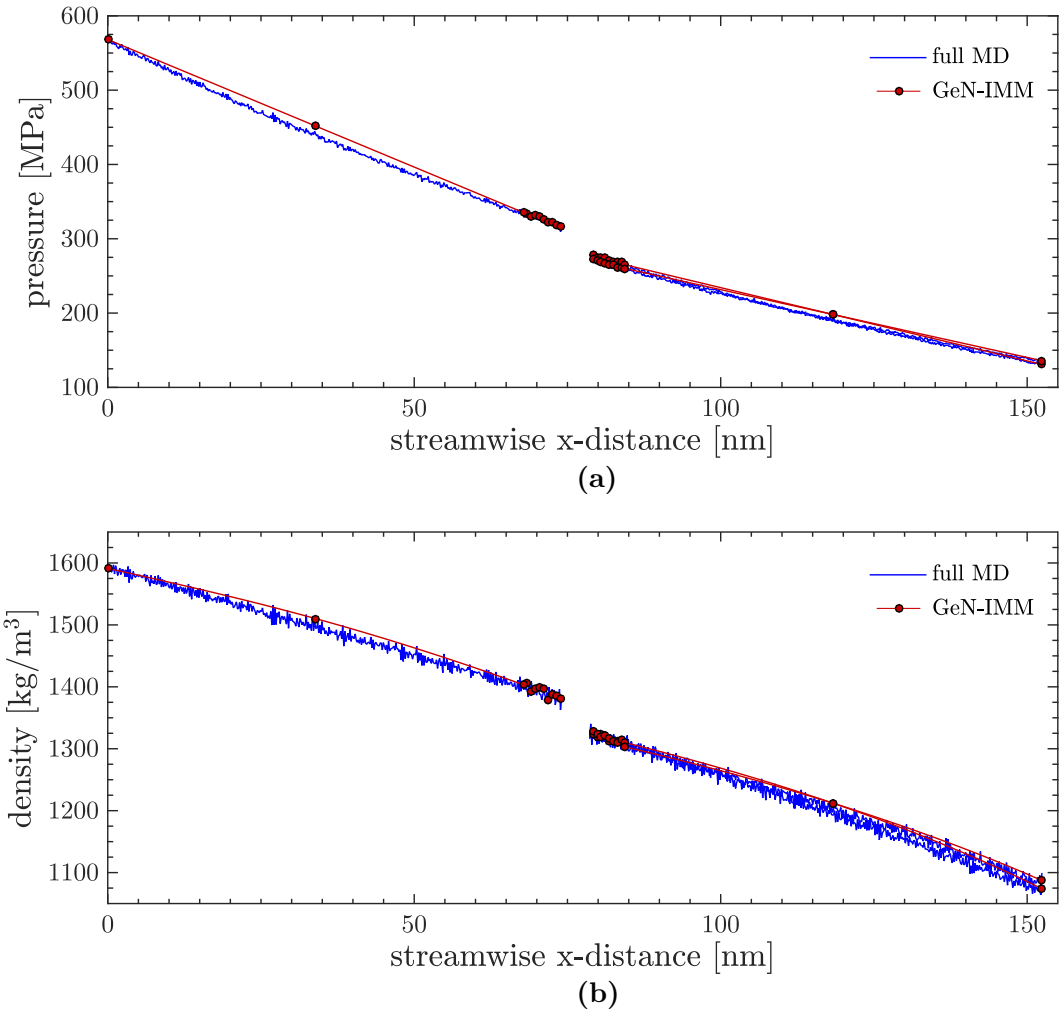

Figure 2.13: Bifurcating network case B1: longitudinal profiles of **(a)** pressure and **(b)** density (averaged over the cross-section). Measured in the GeN-IMM MD micro-elements (at iteration 5) and the full MD simulation. The GeN-IMM density profile in the channel section is generated using the equation of state (2.6)

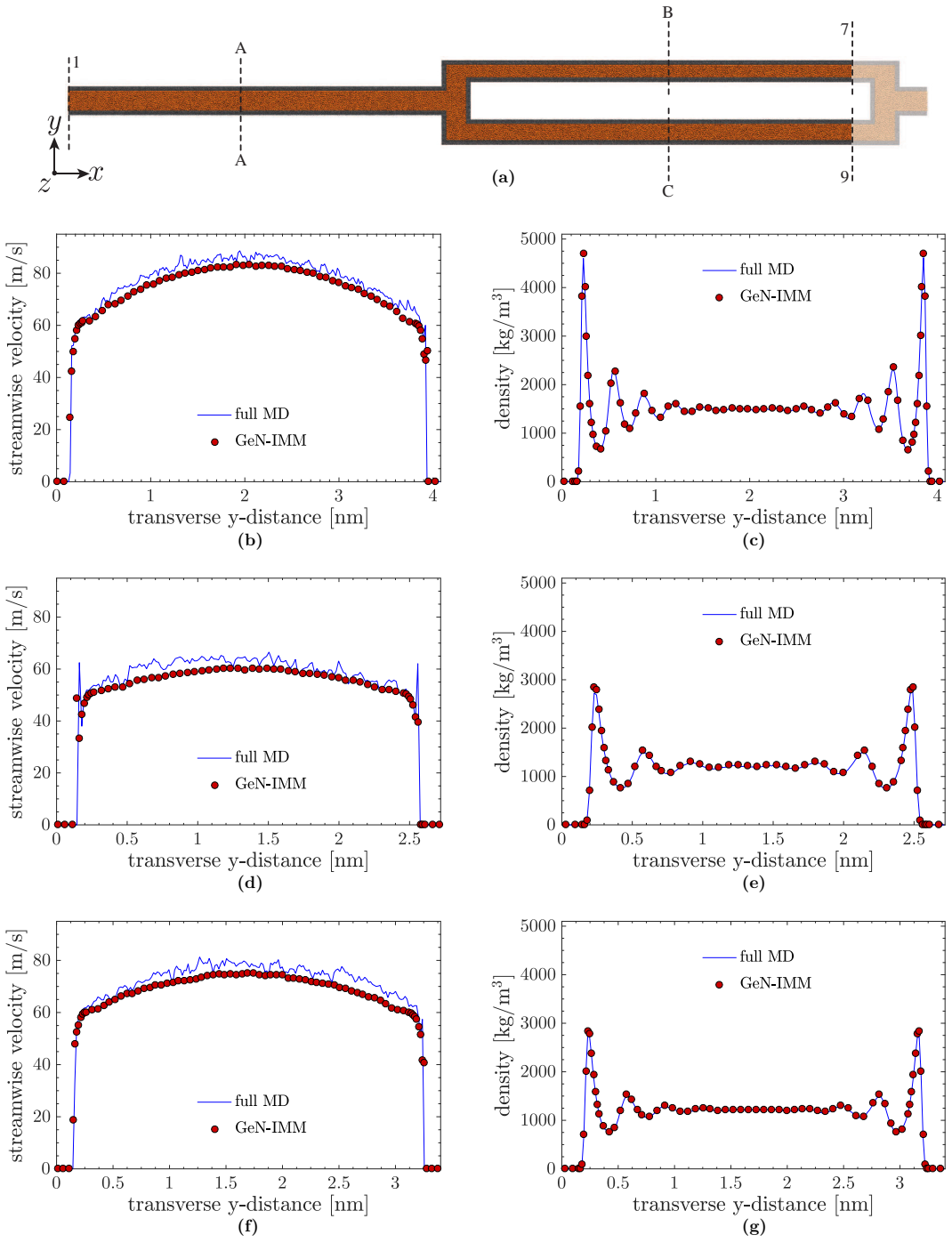

Figure 2.14: Bifurcating network case B1 (bifurcating configuration): **(a)** schematic showing location of channel measurement planes; transverse profiles of streamwise velocity and density at plane A-A **(b & c)**, plane B-B **(d & e)**, and plane C-C **(f & g)**. Measured in the GeN-IMM MD micro-elements (at iteration 5) and the full MD simulation.

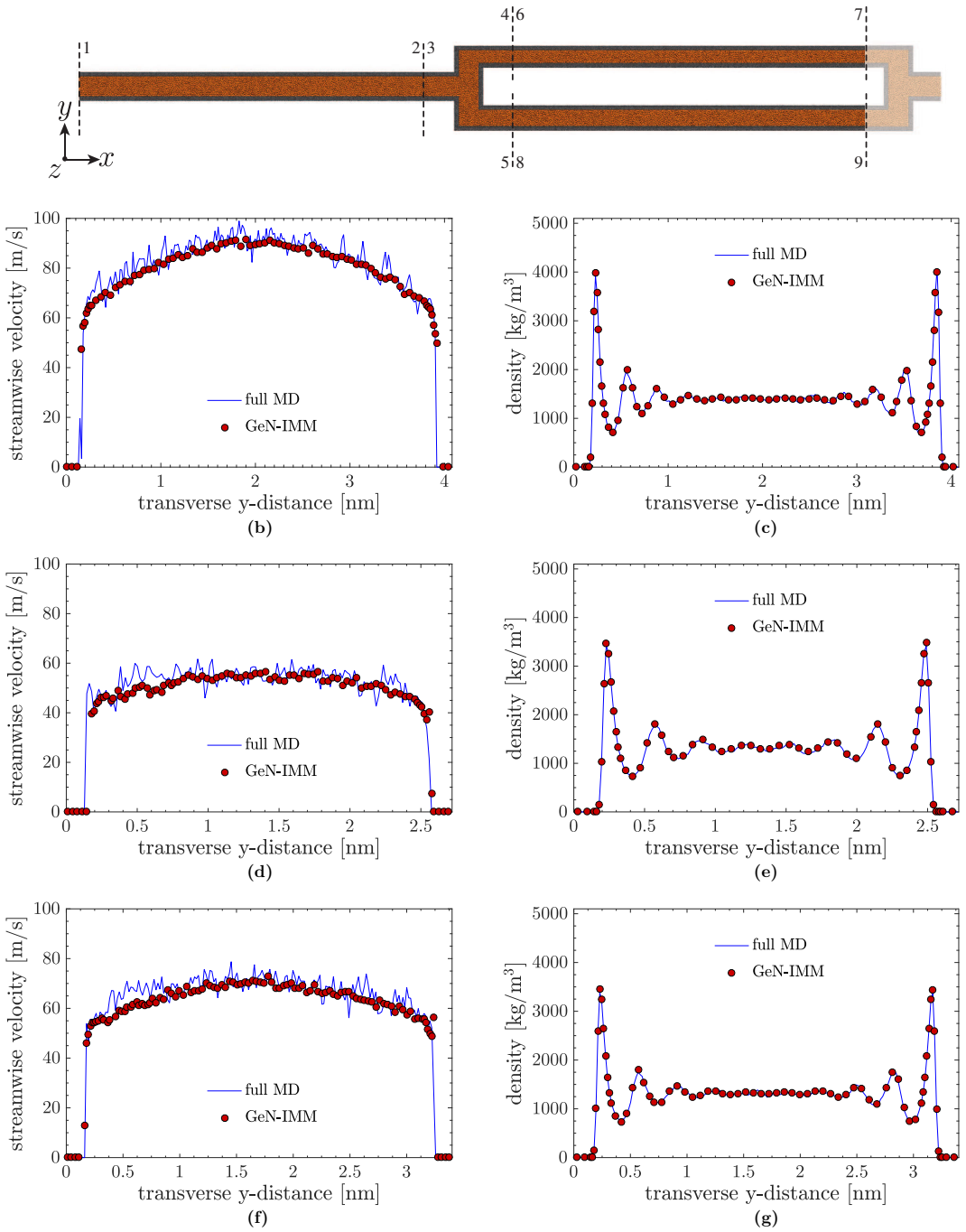

Figure 2.15: Bifurcating network case B1 (bifurcating configuration): **(a)** schematic showing location of channel measurement planes; transverse profiles of streamwise velocity and density at internal boundaries 2|3 **(b & c)**, 4|6 **(d & e)**, and 5|8 **(f & g)**. Measured in the GeN-IMM MD micro-element (at iteration 5) and the full MD simulation.

Case B2 - mixing configuration

Tables 2.7 and 2.8 show the mass flow rate and pressure data for case B2. For this case, the final errors are around 4% for the mass flow rate and 1.5% for pressure, compared to an initial prediction error of 53%. In a complex network such as this, it

Table 2.7: Bifurcating network case B2: mass flow rate measurements for the GeN-IMM MD micro-elements (iteration 5) and the full MD solution. Relative error calculated as $|\dot{m}_F - \dot{m}_i|/|\dot{m}_R| \times 100$.

Boundary #	Full MD $\dot{m}_F$ (ng/s)	GeN-IMM $\dot{m}_i$ (ng/s)	Relative error e_i (%)
1	1.3179	1.4165	3.85
2	1.3179	1.4165	3.85
3	1.3179	1.4166	3.86
4	-1.2381	-1.2437	0.22
5	2.5565	2.6606	4.07
6	-1.2381	-1.2412	0.12
7	-1.2381	-1.2412	0.12
8	2.5565	2.6486	3.60
9	2.5565	2.6486	3.60

Table 2.8: Bifurcating network case B2: pressure measurements for the GeN-IMM MD micro-elements (iteration 5) and the full MD solution. Relative error calculated as $|\dot{m}_F - \dot{m}_i|/|\dot{m}_R| \times 100$.

Boundary #	Full MD P_F (MPa)	GeN-IMM P_i (MPa)	Relative error e_i (%)
1	427.02	427.40	0.05
2	313.43	306.56	0.98
3	313.43	306.02	1.06
4	351.41	341.09	1.49
5	218.86	211.13	1.10
6	351.41	340.09	1.62
7	699.15	699.08	0.01
8	218.86	211.22	1.09
9	45.78	45.89	0.02

is difficult to isolate the probable cause for the increase in error. Four components are simultaneously converging to a mass conservative solution that obeys the pressure boundary conditions, with each component solving for values of internal boundary

pressure, mass flow rate and mean density, while large pressure drops generate pressure non-linearities and variations in viscosity, and the noise present in MD creates statistical uncertainty in measurements.

One possible reason for the increase in error size is the range and magnitude of the pressures involved in this case. While in MD simulations, a high pressure gradient is needed to overcome thermal fluctuations, large pressure differences can lead to non-linearities in pressure and density along the channel. The net flow-conductance through the bifurcating network in case B2 is lower than it is in case B1, so in order to achieve relatively noise-free mass flow rate measurements, a larger pressure drop and a higher inlet pressure is required. In MD, pressure non-linearity arises from varying viscous pressure losses due to the density-dependent viscosity. The rate of viscosity variation increases with increasing density (and thus pressure), so the pressure non-linearity that occurs in component #3 of case B2 is greater than it is in any other component of any case or network, which can be seen in Fig. 2.16. Despite the large pressure and density range, the GeN-IMM still gives a good approximation, particularly in component #4, where the density varies greatly.

As shown for the straight channel network, the pressure non-linearity can be resolved by using multiple components to describe a channel. Figure 2.17 presents the GeN-IMM solution for case B2 with channel component #3 divided into two smaller components, each simulated with a single MD micro-element — this will be referred to as case B2b. The pressure and density distributions of the GeN-IMM solution now much more accurately represent the full molecular simulation, although the density is still slightly over-predicted. Interestingly however, this has had no effect on the converged values of mass flow rate or pressure, which still exhibit up to 4% and 1.5% error, respectively, mirroring the result for the straight channel network when two micro-elements were used. This is unintuitive because one would expect that as the pressure drop over component #3 is unchanged and the density has decreased in case B2b, the mass flow rate would decrease. That the mass flow rate remains the same between case B2 and B2b can be explained by the fact that viscosity is varying with density (and the rate of this variation is increased at large densities), so the lower density leads to a lower viscosity, and the mass flow rate is approximately unchanged. This fact may be a cause for the increase in error between case B2 and case B1, as it would be difficult for the algorithm to converge to the correct density when multiple values produce the same mass flow rate.

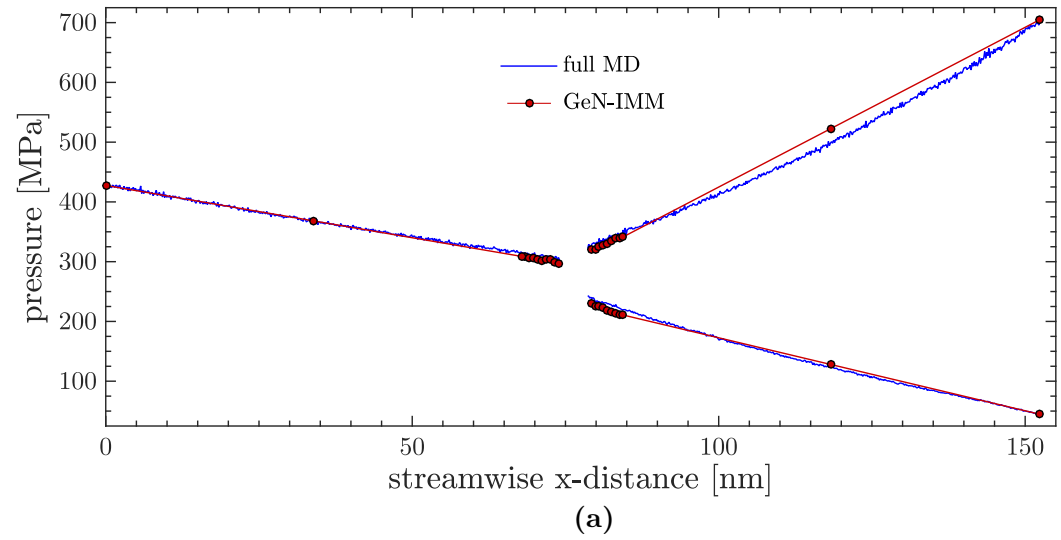

Figure 2.16: Bifurcating channel network case B2: longitudinal profiles of **(a)** pressure and **(b)** density (averaged over the cross-section). Measured in the GeN-IMM MD micro-elements (at iteration 5) and the full MD simulation. The GeN-IMM density profile in the channel section is generated using the equation of state (2.6)

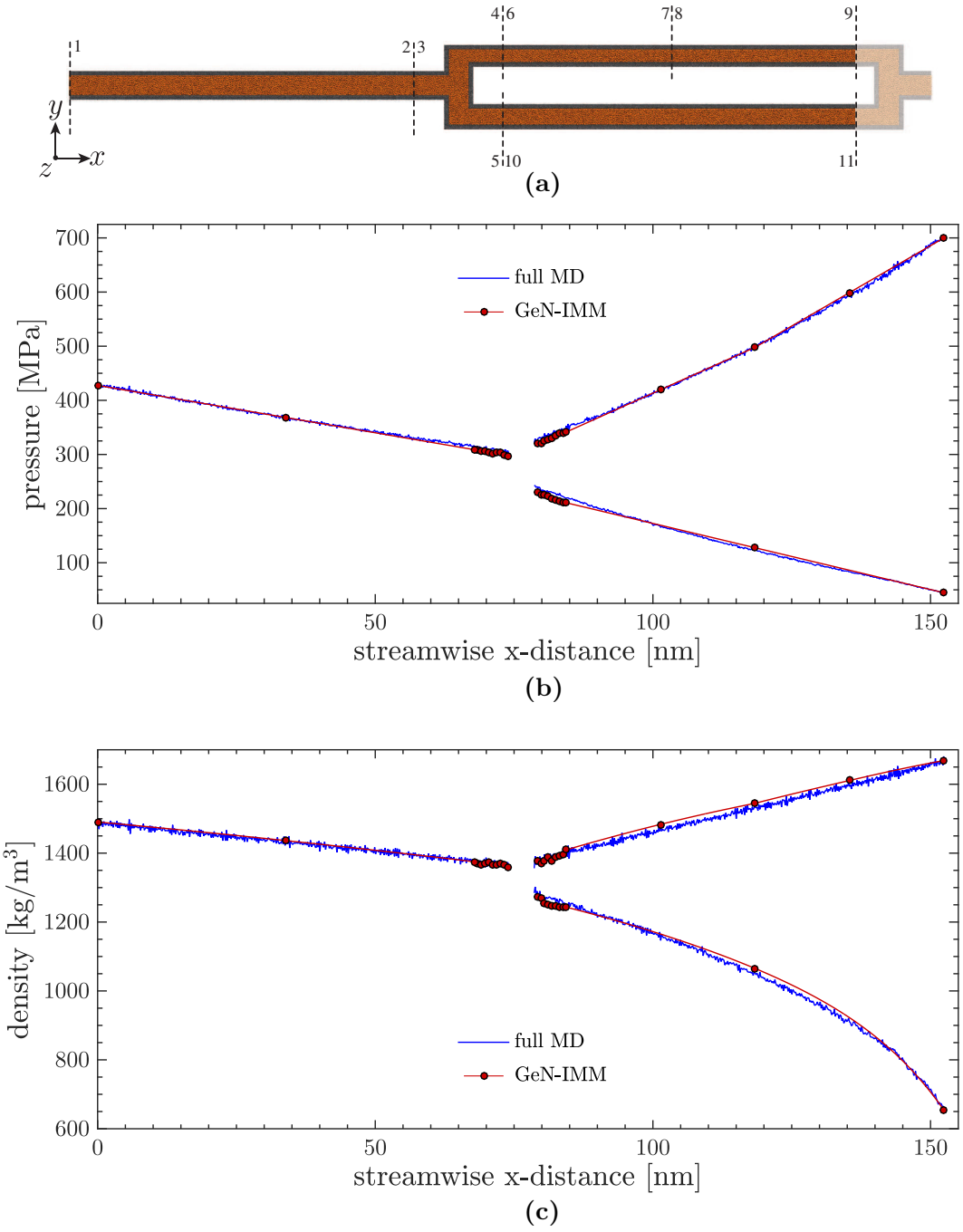

Figure 2.17: Bifurcating channel network case B2b: **(a)** boundary locations using two micro-elements for component #3; longitudinal profiles of **(b)** pressure and **(c)** density (averaged over the cross-section). Measured in the GeN-IMM MD micro-elements (at iteration 5) and the full MD simulation. The GeN-IMM density profile in the channel section is generated using the equation of state described in the methodology

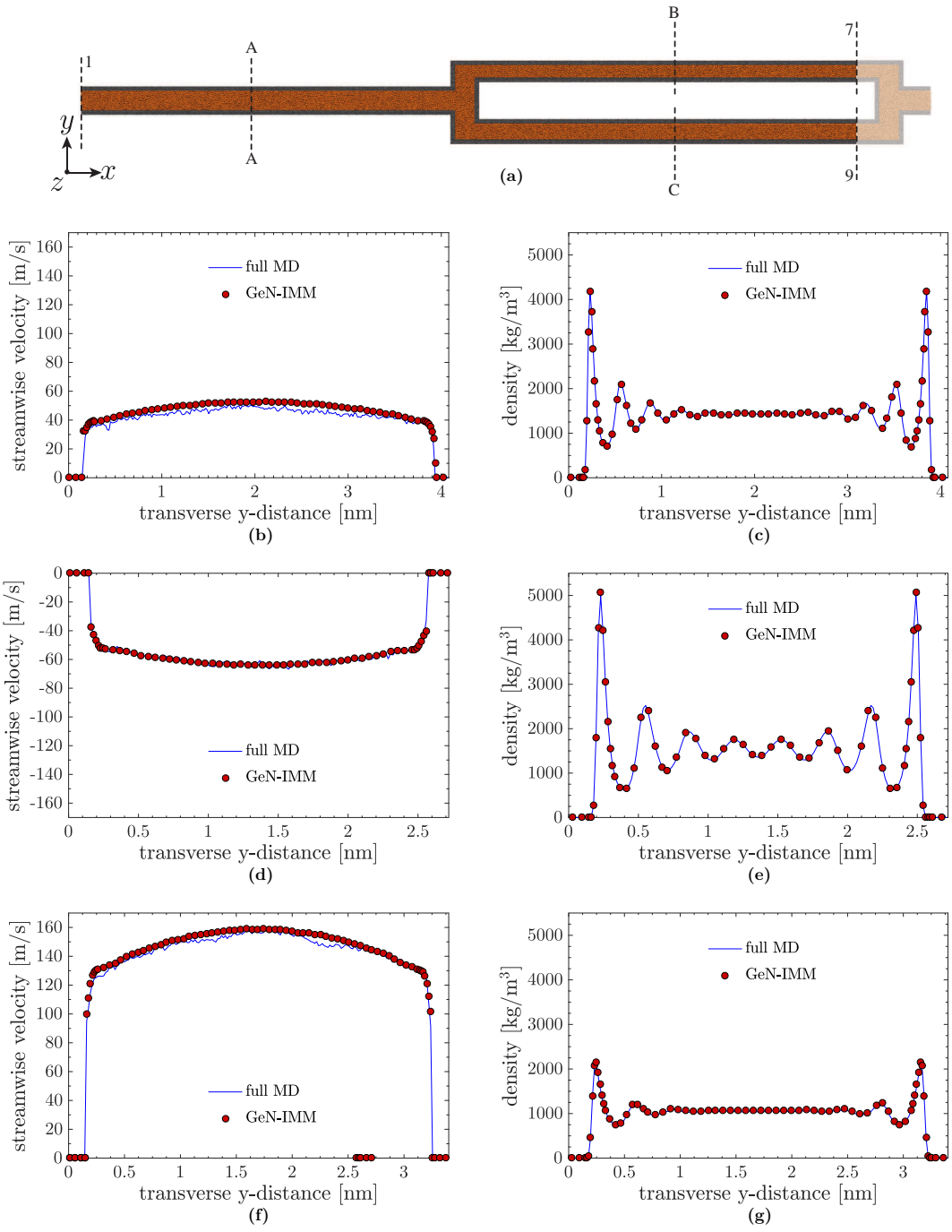

Figure 2.18: Bifurcating channel network case B2 (mixing configuration): **(a)** schematic showing location of channel measurement planes; transverse profiles of streamwise velocity and density at plane A-A **(b & c)**, plane B-B **(d & e)**, and plane C-C **(f & g)**. Measured in the GeN-IMM MD micro-elements (at iteration 5) and the full MD simulation.

One apparent anomaly from Figs. 2.16 and 2.17 is that the GeN-IMM pressure and density profiles in component #1 seem to show strong agreement with the full MD profiles, yet the mass flow rate through component #1 (shown in Table 2.7) does not. The reason for this is that mass flow rate is proportional to the pressure drop over a component (i.e. the pressure difference between its inlet and outlet boundaries), and the pressure drop over component #1 is very small (≈ 114 MPa). So, a small discrepancy between the GeN-IMM and full MD solutions for boundary pressure (≈ 7 MPa) is relatively large compared to the pressure drop and has a considerable effect on the mass flow rate.

The transverse profiles of the streamwise velocity and density for case B2 are displayed in Fig. 2.18 and, despite the overall increase in error for this case, the GeN-IMM solution shows decent agreement with the full MD simulation. As the mass flow rates in components #1 and #4 are larger in the GeN-IMM solution than in the full MD simulation, it follows that the streamwise velocities exhibited are also slightly larger over the entire profile. The velocity profile for component #3 is negative because the fluid flows in the negative x direction.

2.3 Summary

This chapter has presented the methodology and verification for the general networks internal-flow multiscale method (GeN-IMM) which enables the accurate and efficient simulation of compressible fluid flows within complex, non-serial nanoscale geometries. Molecular dynamics (MD) has been used as the micro solver, while the conservation of mass and the continuity of pressure between components provides the macro solution. The advantage of this approach is that non-continuum/non-equilibrium effects such as velocity slip and molecular layering can be accurately captured within the GeN-IMM solution, which a conventional Navier-Stokes solution could not predict. The solver coupling occurs through the exchange of mass flow rate and pressure information from micro to macro, and through the application of body force and density controls from macro to micro.

In the test networks, the GeN-IMM solutions converged after three iterations to mass flow rate and pressure errors of $< 4\%$ and $< 2\%$, respectively (when compared to full MD simulations of the same network). The hybrid approach provided computational speed-ups over full MD of between 2 and 4 times.

The new method has some clear advantages over full molecular simulations: 1) it is more efficient than a full MD simulation, and the computational speed-up will be even greater for larger networks (as the scale separation is larger); and 2) it

is ideally suited to be run on a small cluster of CPUs/GPUs (either simultaneously or sequentially, if resources are limited) since the micro-elements are relatively small simulations that can be run independently at each iteration.

The drawbacks of the GeN-IMM are that it is currently limited to isothermal and steady flows, and that the speed-up in complicated networks is reduced due to the requirement for artificial regions to be simulated to enable periodicity (when using MD as the micro solver). However, it should be noted that as the size of the network increases, the relative size of the artificial regions decreases, so greater savings are made. It is conservatively suggested, as a rule of thumb, that artificial regions should be the same size as the real regions in junction micro-elements, and that each region should have a development length of at least four times that predicted by laminar macroscopic flow theory. This should ensure that no disturbance propagates into the flow field and the flow through all components is fully developed.

Chapter 3

Design Applications of the GeN-IMM

In Chapter 2, the general networks internal-flow multiscale method (GeN-IMM) was proposed and developed as a simulation tool for complex networks that exhibit a high degree of scale separation; however, its function extends beyond this. In this chapter, the application of the GeN-IMM to the design of nanofluidic networks is considered by 1) enabling the geometrical features of the network, i.e. the channel heights and lengths, to be variables that are the output of the iterative scheme; and 2) facilitating this by permitting a range of different macroscopic properties to be fixed as *generalised constraints* for the hybrid method, rather than being limited to fixing the network geometry and pressure at external boundaries. This effectively removes the need for a trial-and-error approach to determine inlet/outlet pressure and channel geometry when other macroscopic properties are known.

The new generalised constraints introduced are applied to mass flow rate, shear stress, and volume. Mass flow rate control is essential for enabling precise chemical reactions to be performed in lab-on-a-chip applications. It is also important for nanoscale drug delivery applications [Emerich and Thanos, 2006], where the dosage must be large enough for the drug to take effect, but not so large as to damage healthy cells and cause adverse side effects. The ability to specify shear stress as a constraint in the design of nanoscale networks also has many uses. Cell response studies show that a low shear stress environment can reduce the damage to shear-sensitive cells [Ma et al., 2002] and increase the probability of cells binding to surfaces [Aunins et al., 2003]. Conversely, a high shear stress may be desirable to minimise blocking problems in networks where the channel heights are constricted. Volume constraints may represent an economical limitation, or could be used as part

of an optimisation principle (see part 2 of this thesis), while some other property (e.g. mass flow rate) is maximised or minimised.

3.1 Methodology

The main aim of the hybrid method is the same as before: the network is decomposed into components so that channels can be simulated by smaller micro-elements for computational savings. Channel and junction components are simulated in the same manner as before, but the way that the boundary conditions, design constraints, and iterative scheme are defined is more generalised. In order for the GeN-IMM solution to correspond to that of the full network, the values of mass flow rate ($\dot{m}$), pressure (P), and channel height (H) at the internal boundaries i and j of neighbouring components p and q must be equal, i.e.

$$\dot{m}_{i,p} = -\dot{m}_{j,q}, \tag{3.1}$$

$$P_{i,p} = P_{j,q}, \tag{3.2}$$

$$H_{i,p} = H_{j,q}. \tag{3.3}$$

It is again noted that the mass flow rates in equation (3.1) are equal and opposite because mass flow rate is deemed to be positive if it flows out of the component. Unlike in Chapter 2, the channel height is now a variable that is described at every boundary. Varying heights along a channel component can be accommodated by the IMM procedure, as seen in Borg et al. [2013a]; Patronis et al. [2013], but for simplification, in this thesis it is assumed that the height is constant along the length of each channel component, i.e.

$$H_{i,q_c} = H_{j,q_c} = H_{q_c}, \tag{3.4}$$

where the subscript c indicates that component q is a channel (rather than a junction). From hereon, for convenience, channel components will be considered to have only one height variable H_{q_c}. In addition to being consistent at internal boundaries, the macroscopic variables must also meet the values set by the generalised constraints. In Chapter 2, these constraints referred only to the fixed channel heights and lengths, and the external boundary conditions placed on pressure. In this extended version of the GeN-IMM, values of mass flow rate, pressure, and height can

be constrained at any boundary, i.e.

$$\dot{m}_{i,q} = \dot{m}_B, \tag{3.5}$$

$$P_{i,q} = P_B, \tag{3.6}$$

$$H_{i,q} = H_B, \tag{3.7}$$

where the subscript B denotes a generalised constraint. In some instances, generalised constraints are applied over the entire component, rather than at a single boundary. Constraints fixing channel length L, mean wall shear stress τ, and volume V are described in this way:

$$L_{q_c} = L_B, \tag{3.8}$$

$$\tau_{q_c} = \tau_B, \tag{3.9}$$

$$\sum_{q=1}^{Q_v} V_q = V_B, \tag{3.10}$$

where Q_v is the number of components over which the volume constraint acts. This means that the fixed volume may refer to a single component ($Q_v = 1$), or it may be the total volume of multiple components ($Q_v > 1$). Length constraints only apply to channel components and, for practicality, shear stress constraints are likewise restricted, hence the subscript c in equations (3.8) and (3.9). For straight channels, the generalised constraint for shear stress can be rearranged in terms of boundary pressure, height, and length by a force balance:

$$\tau_{q_c} = \frac{(P_{i,q_c} - P_{j,q_c})\, H_{q_c}}{2L_{q_c}}. \tag{3.11}$$

Through basic geometry, volume constraints can also be redefined. For junction components, the exact form of this equation will vary with the nature of the component; for channel components:

$$\sum_{q=1}^{Q_v} V_q = \sum_{q=1}^{Q_v} H_{q_c} L_{q_c}. \tag{3.12}$$

By generalising the application of constraints, it is now possible to over- or under-constrain a single component. For a full description of how constraints must be specified, see Appendix G. It should be noted that the constraints expressed in Chapter 2 can be reclaimed by opting to fix the channel heights, the channel lengths, and the pressures at external boundaries.

The GeN-IMM is still only applicable to steady-state flows, so the net mass flow rate through all boundaries of one component is zero:

$$\sum_{i=1}^{W_q} \dot{m}_{i,q} = 0, \tag{3.13}$$

where W_q is the total number of boundaries of the q^{th} component. As in Chapter 2, equation (3.13) maintains local mass conversion, and combined with equation (3.1), global mass conservation is ensured.

The unknown variables must be solved by iterative refinement, using equation (2.5), and are considered to be the output of the GeN-IMM procedure. In Chapter 2, these variables were the pressures at internal boundaries and the mass flow rate(s), but in this generalisation they may be any combination of mass flow rate, pressure, height, and length. This means that the iterative refinement process must take into account the geometry of the components, i.e. the height and length of channel components; and the height of each boundary for junction components. This is accomplished by expressing each flow-conductance coefficient $K_{ij,q}$ as a function of the component geometry and an unknown prefactor. Note, the value of the prefactors (and hence the flow-conductance coefficients) only affects the convergence rate of the GeN-IMM solution, not the converged result. The prefactors can be updated every iteration by the method detailed in Appendix C.

For channel components, the form of this function is relatively simple. From observation of the approximate Poiseuille solution for rectangular ducts [White, 1974], a prediction is made that the flow conductance will vary linearly in response to 1) a change in the cube of the height, and 2) a change in the reciprocal of the length, i.e.

$$K_{ij,q_c} = \lambda_q \left(\frac{H_{q_c}^3}{L_{q_c}} \right), \tag{3.14}$$

where λ_q is the channel component prefactor for the q^{th} component.

Estimating the flow conductance between two boundaries of a junction is more challenging. Here it is assumed that the total conductance between the two boundaries is composed of two conductance components in series: two notional channels of equal length and of height equal to each boundary. The conductance in each of these notional channels is proportional to the cube of its height, as per equation (3.14). There are certainly more elaborate means to do this (e.g. introducing lengths of each notional channel to more accurately represent the geometry of the junction), but given that greater accuracy only improves the convergence rate, the

more straightforward approach is preferred here. Following basic flow-circuit rules, the total flow conductance is

$$K_{ij,q} = \Omega_{ij,q} \left(\frac{H_{i,q}^3 H_{j,q}^3}{H_{i,q}^3 + H_{j,q}^3} \right), \tag{3.15}$$

where $\Omega_{ij,q}$ is the junction prefactor between the i^{th} and j^{th} boundaries of the q^{th} component. It should be noted that in this extended version of the GeN-IMM, equation (2.5) is often non-linear (e.g. when height is a variable), as are the constraints for shear stress (equation (3.11)) and volume (equation (3.12)). This means the system of equations cannot be solved completely by a simple matrix inversion procedure. In this instance, a smaller system of equations is solved using initial estimates for variables that cause non-linearity (one non-linear equation is removed from the system for each variable that is estimated). From this solution, new estimates for the temporarily-fixed variables are found using the relevant non-linear equations, and the system of linear equations is solved once more with the updated estimates. This creates a second iterative procedure which will hereon be referred to as the iterative matrix solution, to distinguish it from the iterative refinement procedure that the GeN-IMM employs. Note, the iterative matrix solution has virtually no computational cost compared to the iterative refinement procedure. The iterative matrix solution continues until the non-linear variables are no longer updated. Equation (2.5) ensures that as the molecular dynamics (MD) micro-elements converge to global mass conservation and pressure continuity, the variables of mass flow rate, pressure, height, and length will cease to be updated in subsequent iterative refinements.

Fluid compressibility is accounted for in exactly the same way as described in Chapter 2, using equation of state (2.6). The forcing for channel components is also calculated exactly as before, using equation (2.8). For junction components, the body force-generated pressure jumps $\Phi_{i,q}$ are determined from the iterative refinement equation (2.9), with the flow-conductance coefficients now a function of the varying geometry:

$$D_{ij,q} = \Psi_{ij,q} \left(\frac{H_{i,q}^3 H_{j,q}^3}{H_{i,q}^3 + H_{j,q}^3} \right), \tag{3.16}$$

where $\Psi_{ij,q}$ is the artificial prefactor between the boundaries i and j in component q.

3.1.1 Algorithm

The iterative algorithm for the extended version of the GeN-IMM is as follows:

1. Approximate the prefactors λ_{q_c}, $\Omega_{ij,q}$, and $\Psi_{ij,q}$, and make initial estimates for the unknown heights and lengths.

2. Calculate the initial flow-conductance coefficients $K_{ij,q}$ and $D_{ij,q}$ for each component. The terms in angular brackets in equations (2.5) and (2.9) are assumed to be zero.

3. Solve the set of linear equations, using the iterative matrix solution procedure, for the predicted mass flow rates $\dot{m}_{i,q}$, pressures $P_{i,q}$, heights $H_{i,q}$, lengths L_{q_c}, and junction pressure jumps $\Phi_{i,q}$.

4. Solve equation (2.6) for the mean mass densities $\bar{\rho}_q$ in all components. If this is the first iteration, the terms in angle brackets are assumed to be zero.

5. Solve equation (2.8) for the channel component body forces F_q.

6. Run all micro-element MD simulations with the new heights, lengths, body forces, and mean densities until steady state. At steady state, measure the time-averaged mass flow rate $\langle \dot{m}_{i,q} \rangle$ at every boundary. In addition, for junctions measure the pressure $\langle P_{i,q} \rangle$ at every boundary, and for channels measure the mean pressure $\langle \bar{P}_q \rangle$ over the micro-element. These measured properties are used in equations (2.5), (2.6), and (2.9) for the next iteration. Note, for channel components, the term $(P_{i,q} - P_{j,q})$ is obtained directly from equation (2.8).

7. Update the prefactors λ_{q_c}, $\Omega_{ij,q}$, and $\Psi_{ij,q}$, and hence the flow-conductance coefficients $K_{ij,q}$ and $D_{ij,q}$.

8. Repeat from step 2 until a convergence criterion is met for the variables Γ at a given boundary (if the variable is mass flow rate, pressure, or height) or component (if the variable is length):

$$\zeta_{i,q} < \zeta^{\text{tol}}, \quad \text{with} \quad \zeta_{i,q} = \left| \frac{\Gamma_l - \Gamma_{l-1}}{\Gamma_l} \right|, \tag{3.17}$$

   where ζ^{tol} is a predetermined convergence tolerance and $\Gamma = \dot{m}_{i,q},\ P_{i,q},\ H_{i,q},$ or L_q.

3.2 Results and discussion

This extended version GeN-IMM is tested on compressible pressure-driven flows through the straight channel and bifurcating channel geometries introduced in Chapter 2, but with different combinations of constraints. This means that by comparing the GeN-IMM solution to the full MD simulation, the comparative accuracy between the extended GeN-IMM and the original hybrid method can be directly analysed. Although the full MD simulations are the same as in Chapter 2, the results will demonstrate that the extended GeN-IMM will converge to the correct macroscopic system properties for a wide variety of user-input generalised constraints, and have the potential to make large computational savings. In addition, for some cases, the constraints are properties that cannot be constrained in a full MD simulation, i.e. they are measured outputs such as mass flow rate or wall shear stress. In these instances, using a full MD simulation is completely impractical as a trial-and-error process would be required to obtain the desired properties. For all the cases in this chapter, the full MD simulations are run in parallel on 48 CPUs, while the micro-elements are run on single GPUs. This also means that the GeN-IMM is less reliant on supercomputer resources than the equivalent full MD simulation.

3.2.1 A straight channel network

In the full MD simulation, the channel length is $L_2 = 102$ nm, the channel height is $H_2 = H_3 = H_4 = H_5 = 3.4$ nm, the inlet and outlet reservoir heights are $H_1 = H_6 = 6.8$ nm, and the inlet and outlet pressures are $P_1 = 648$ MPa and $P_6 = 295$ MPa, respectively. The depth (in the z-direction) is a constant 6.8 nm along the entire network. Four test cases are considered with the generalised hybrid setup shown in Fig. 3.1. Each case uses different generalised constraints and has different outputs as the solution to the GeN-IMM iterative procedure. The cases are labelled S2-S5, with case S1 being the straight channel example from Chapter 2. In all cases, the entrance/exit regions of the reservoir components are constant and sufficient to allow fully developed flow in the channel component. The length of the channel micro-element is a constant $L_2' = 4.08$ nm (even if the length of the channel component is a variable), and the depth of all micro-elements is a constant 6.8 nm in each case. In all cases, the initial flow-conductance coefficients $K_{ij,q}$ and $D_{ij,q}$ are the same as those used in case S1 (i.e. those in Table 2.1).

(a) Multiscaled Network

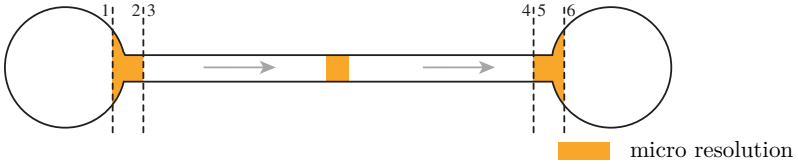

(b) Hybrid Simulation

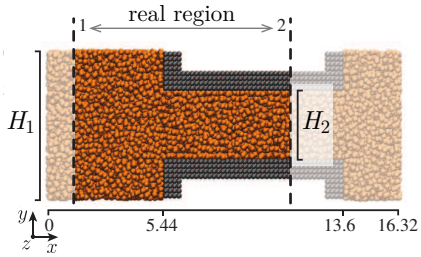

(i) MD micro-element #1: inlet reservoir

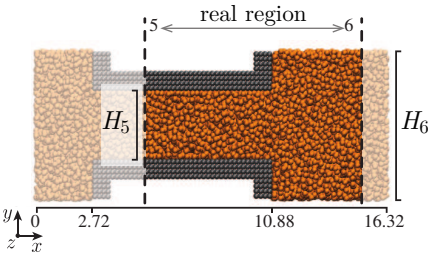

(iii) MD micro-element #3: outlet reservoir

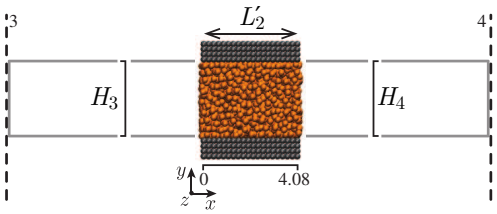

(ii) MD micro-element #2: channel

(c) Full MD Simulation

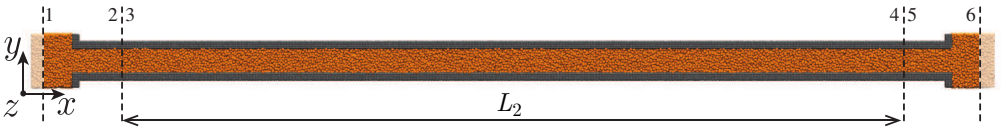

Figure 3.1: **(a)** Schematic of the straight channel multiscale network, with **(b)** the generalised hybrid MD GeN-IMM decomposition, and **(c)** the full MD network setup. Dimensions are in nanometers. The boundary numbers are labelled above each image.

Case S2 setup

The generalised constraints for case S2 are a fixed inlet pressure $P_1 = 648$ MPa, a fixed mass flow rate $\dot{m}_1 = \dot{m}_2 = \dot{m}_3 = \dot{m}_4 = \dot{m}_5 = \dot{m}_6 = 1.5389$ ng/s, a fixed channel height $H_2 = H_3 = H_4 = H_5 = 3.4$ nm, and a fixed channel length $L_2 = 102$ nm. This differs from case S1 by constraining mass flow rate instead of outlet pressure, making the outputs of the GeN-IMM solution the pressures at the internal boundaries and the outlet. The state of convergence is determined using $\Gamma = P$ in equation (3.17) applied at boundary #6, as this is the least constrained boundary (i.e. it is furthest from the inlet where the pressure is fixed). The initial prefactor estimates are shown in Table 3.1.

Table 3.1: Initial prefactors λ_{q_c}, $\Omega_{ij,q}$, and $\Psi_{ij,q}$ for the straight channel network case S2.

Component # q	Boundary # i,j	prefactor λ_{q_c} ($\times 10^{-2}$ s/m)	prefactor $\Omega_{ij,q}$ ($\times 10^{6}$ s/m^2)	prefactor $\Psi_{ij,q}$ ($\times 10^{6}$ s/m^2)
1	1,2	-	-1.2269	-3.1443
2	3,4	-2.7789	-	-
3	5,6	-	-1.7790	-1.9512

Case S3 setup

The generalised constraints for case S3 are a fixed inlet pressure $P_1 = 648$ MPa, a fixed outlet pressure $P_6 = 295$ MPa, a fixed mass flow rate $\dot{m}_1 = \dot{m}_2 = \dot{m}_3 = \dot{m}_4 = \dot{m}_5 = \dot{m}_6 = 1.5389$ ng/s, and a fixed channel length $L_2 = 102$ nm. The outputs of the GeN-IMM solution are the channel height and the pressures at the internal boundaries. The state of convergence is determined using $\Gamma = H$ in equation (3.17).

Table 3.2: Initial prefactors λ_{q_c}, $\Omega_{ij,q}$, and $\Psi_{ij,q}$ for the straight channel network case S3.

Component # q	Boundary # i,j	prefactor λ_{q_c} ($\times 10^{-2}$ s/m)	prefactor $\Omega_{ij,q}$ ($\times 10^{6}$ s/m^2)	prefactor $\Psi_{ij,q}$ ($\times 10^{6}$ s/m^2)
1	1,2	-	-0.4026	-1.0317
2	3,4	-0.6784	-	-
3	5,6	-	-0.5837	-0.6402

The initial prefactor estimates are shown in Table 3.2. As the channel height in this case is unknown, an intentionally poor initial prediction of $H_2 = H_3 = H_4 = H_5 = 5.44$ nm (60% error) is made to demonstrate that the speed and accuracy of the GeN-IMM solution is not strongly dependent on the accuracy of the initial estimations.

Case S4 setup

The generalised constraints for case S4 are a fixed inlet pressure $P_1 = 648$ MPa, a fixed outlet pressure $P_6 = 295$ MPa, a fixed mass flow rate $\dot{m}_1 = \dot{m}_2 = \dot{m}_3 = \dot{m}_4 = \dot{m}_5 = \dot{m}_6 = 1.5389$ ng/s, and a fixed channel height $H_2 = H_3 = H_4 = H_5 = 3.4$ nm. The outputs of the GeN-IMM solution are the channel length and the pressures at the internal boundaries. The state of convergence is determined using $\Gamma = L$ in equation (3.17). The initial prefactor estimates are shown in Table 3.3. As the channel length in this case is unknown, an intentionally poor initial prediction of $L_2 = 170$ nm (67% error) is made to further demonstrate that the speed and accuracy of the GeN-IMM solution is not strongly dependent on the accuracy of the initial estimations.

Table 3.3: Initial prefactors λ_{q_c}, $\Omega_{ij,q}$, and $\Psi_{ij,q}$ for the straight channel network case S4.

Component #	Boundary #	prefactor		
q	i,j	λ_{q_c} ($\times 10^{-2}$ s/m)	$\Omega_{ij,q}$ ($\times 10^{6}$ s/m^2)	$\Psi_{ij,q}$ ($\times 10^{6}$ s/m^2)
1	1,2	-	-1.2269	-3.1443
2	3,4	-4.6315	-	-
3	5,6	-	-1.7790	-1.9512

Case S5 setup

The generalised constraints for case S5 are a fixed inlet pressure $P_1 = 648$ MPa, a fixed outlet pressure $P_6 = 295$ MPa, a fixed wall shear stress $\tau_2 = 4.7883$ MPa, and a fixed channel volume $V_2 = 2358.24$ nm^3. As the GeN-IMM is specifically for high-aspect-ratio networks, a volume constraint over the channel component is also approximately equal to a volume constraint over the entire domain. The outputs of the GeN-IMM solution are the channel height, the channel length, and the pressures at the internal boundaries. The state of convergence is determined using $\Gamma = \dot{m}$ in equation (3.17) as mass flow rate is slower to converge than channel height or

length. The initial prefactor estimates are shown in Table 3.4. In this case the channel height and length are unknown, so intentionally poor initial predictions of $H_2 = H_3 = H_4 = H_5 = 5.44$ nm (60% error) and $L_2 = 170$ (67% error) are made.

Table 3.4: Initial prefactors λ_{q_c}, $\Omega_{ij,q}$, and $\Psi_{ij,q}$ for the straight channel network case S5.

Component #	Boundary #	prefactor		
q	i,j	λ_{q_c} ($\times 10^{-2}$ s/m)	$\Omega_{ij,q}$ ($\times 10^{6}$ s/m^2)	$\Psi_{ij,q}$ ($\times 10^{6}$ s/m^2)
1	1,2	-	-0.4026	-1.0317
2	3,4	-1.1307	-	-
3	5,6	-	-0.5837	-0.6402

Results

The GeN-IMM measured mass flow rate and pressure results (at iteration 5) for cases S2-S5 are shown in Tables 3.5-3.8. Strong agreement is shown between the hybrid method solution and the full MD simulation, with errors of $< 1\%$ at almost all boundaries for all cases. In case S5, where the mass flow rate is not a constraint, the initial mass flow rate error was 47%. Similarly, in case S2 the outlet boundary pressure is not fixed and had an initial error of 53%.

Table 3.5: Straight channel network cases S2-S5: mass flow rate measurements for the GeN-IMM MD micro-elements (at iteration 5) and the full MD solution.

Boundary #	Full MD	GeN-IMM			
	$\dot{m}_F$ (ng/s)	Case S2 $\dot{m}_i$ (ng/s)	Case S3 $\dot{m}_i$ (ng/s)	Case S4 $\dot{m}_i$ (ng/s)	Case S5 $\dot{m}_i$ (ng/s)
1	1.5389	1.5457	1.5394	1.5346	1.5479
2	1.5387	1.5456	1.5393	1.5347	1.5481
3	1.5389	1.5517	1.5523	1.5498	1.5248
4	1.5389	1.5517	1.5522	1.5498	1.5248
5	1.5389	1.5342	1.5358	1.5487	1.5223
6	1.5387	1.5342	1.5358	1.5487	1.5222

Table 3.6: Straight channel network cases S2-S5: relative measured mass flow rate error between the GeN-IMM MD micro-elements (at iteration 5) and the full MD solution. Relative error calculated as $|\dot{m}_F - \dot{m}_i|/|\dot{m}_R| \times 100$.

Boundary #	GeN-IMM			
	Case S2 e_i (%)	Case S3 e_i (%)	Case S4 e_i (%)	Case S5 e_i (%)
1	0.45	0.04	0.28	0.59
2	0.45	0.04	0.27	0.61
3	0.83	0.87	0.71	0.92
4	0.83	0.87	0.71	0.92
5	0.30	0.20	0.64	1.08
6	0.29	0.19	0.65	1.07

Table 3.7: Straight channel network cases S2-S5: pressure measurements for the GeN-IMM MD micro-elements (at iteration 5) and the full MD solution.

Boundary #	Full MD	GeN-IMM			
	P_F (MPa)	Case S2 P_i (MPa)	Case S3 P_i (MPa)	Case S4 P_i (MPa)	Case S5 P_i (MPa)
1	648.01	647.60	647.57	648.49	647.67
2	606.07	604.53	603.72	604.54	604.50
3	606.07	604.90	604.61	604.36	606.14
4	318.77	315.96	317.43	318.06	318.43
5	318.77	316.03	317.90	317.88	317.96
6	295.06	293.70	294.89	295.04	295.16

Table 3.8: Straight channel network cases S2-S5 relative measured pressure error between the GeN-IMM MD micro-elements (at iteration 5) and the full MD solution. Relative error calculated as $|P_F - P_i|/|P_R| \times 100$.

Boundary #	GeN-IMM			
	Case S2 e_i (%)	Case S3 e_i (%)	Case S4 e_i (%)	Case S5 e_i (%)
1	0.06	0.07	0.07	0.05
2	0.24	0.36	0.23	0.24
3	0.18	0.22	0.26	0.01
4	0.43	0.21	0.11	0.05
5	0.42	0.13	0.14	0.12
6	0.21	0.03	0.00	0.01

The errors recorded at the final iteration are of similar magnitude to those in case S1, suggesting that the GeN-IMM is robust for a wide variety of generalised constraints and outputs. The final relative errors are sufficiently small that they can be accounted for by the noise inherent in MD simulations. Cases S3-S5 also have unconstrained channel geometry: the height in cases S3 and S5, and the length in cases S4 and S5. After five iterations, the channel height in cases S3 and S5 is 3.4007 nm and 3.3978 nm, respectively, compared to 3.4 nm in the full MD simulation. This produces relative errors of 0.02% and 0.06%, respectively, compared to initial errors of 60%. In cases S4 and S5, the channel length after five iterations is 101.45 nm and 102.07 nm, respectively, compared to 102 nm in the full MD simulation. This produces relative errors of 0.54% and 0.06%, respectively, compared to initial errors of 67%.

For all cases, convergence occurs to a tight tolerance of $\zeta^{\text{tol}} = 0.02$ after three iterations (just as in case S1 — see Fig. 2.7), as shown in Fig. 3.2 using equation (3.17). Using the formula described in Chapter 2, each case has a speed-up $\tau_F/\tau_G = 3.9$ compared to the full MD simulation, although this does not take into account the costly trial-and-error process required for a full molecular simulation to meet the desired macroscopic constraints. As noted in chapter 2, this speed-up is modest due to the necessity to keep the test case small so that the full MD simulation is computationally tractable.

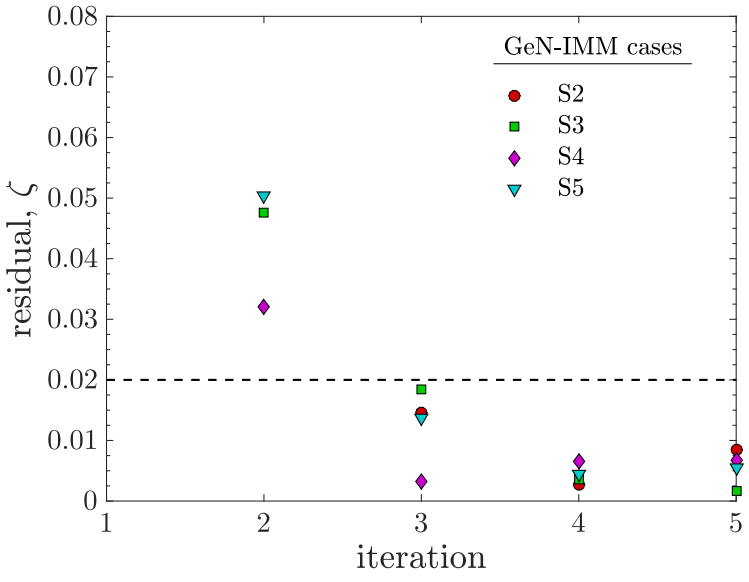

Figure 3.2: straight channel network cases S2-S5: convergence of the GeN-IMM, with $\Gamma = P$, $\Gamma = H$, $\Gamma = L$, and $\Gamma = \dot{m}$ for cases S2, S3, S4, and S5, respectively. The horizontal line is the prescribed tolerance ζ^{tol}.

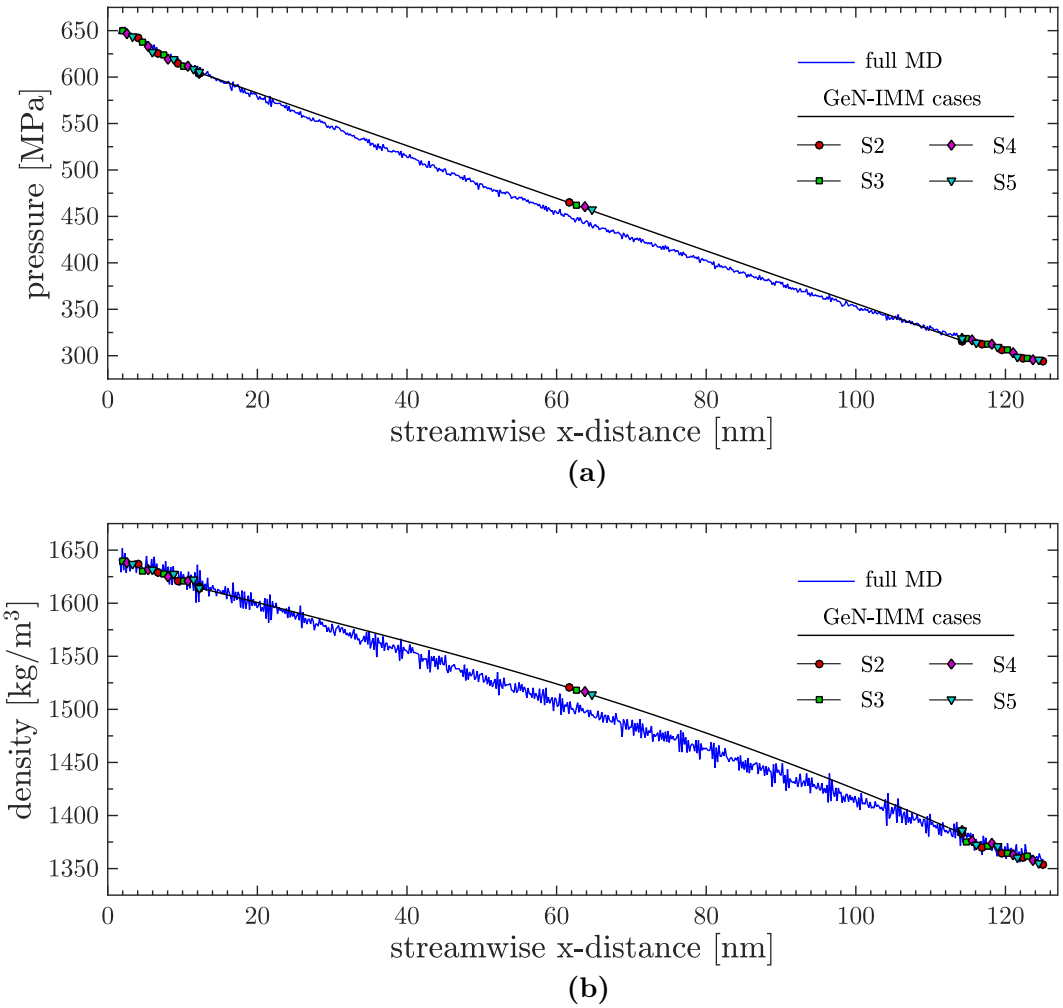

Figure 3.3: Straight channel network cases S2-S5:longitudinal profiles of **(a)** pressure and **(b)** density (averaged over the cross-section). Measured in the GeN-IMM MD micro-elements (at iteration 5) and the full MD simulation. The GeN-IMM density profile in the channel section is generated using the equation of state (2.6).

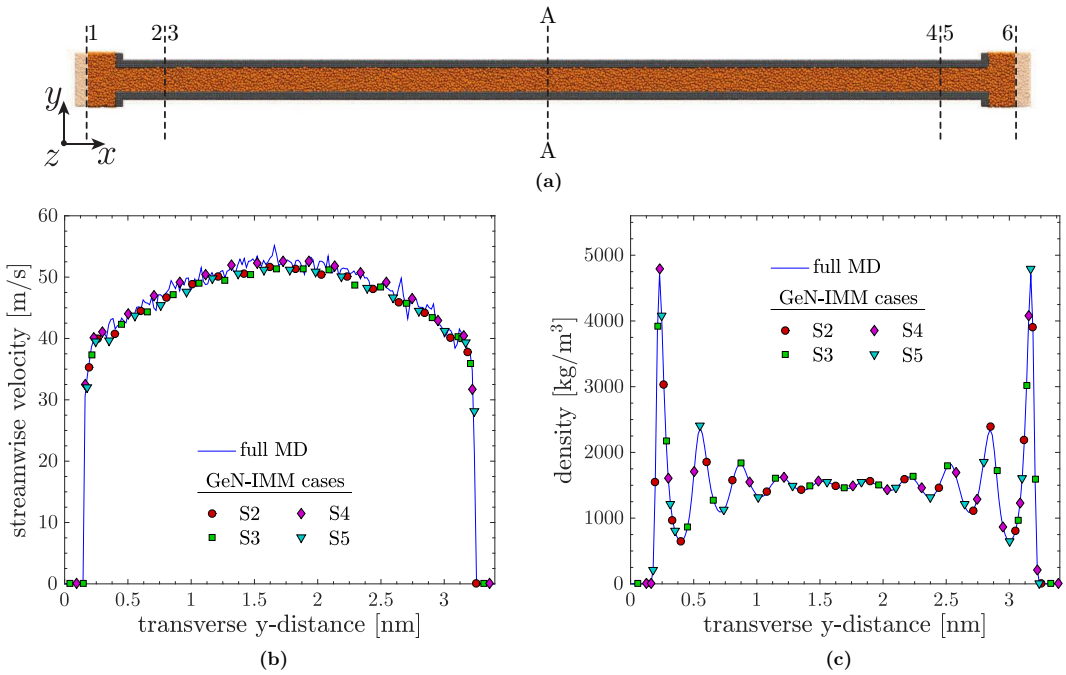

Figure 3.4: Straight channel network cases S2-S5: **(a)** schematic showing the location of plane A-A; transverse profiles of **(b)** streamwise velocity and **(c)** density. Measured in the GeN-IMM MD micro-elements (at iteration 5) and the full MD simulation.

Longitudinal and transverse profiles are plotted in Fig. 3.3 and Fig. 3.4, respectively, to demonstrate that this extended version of the GeN-IMM still accurately represents the full MD simulation and captures non-continuum/non-equilibrium effects. All GeN-IMM profiles are plotted at iteration 5 and, for concision, all four cases S2-S5 are plotted together. In Fig. 3.3 excellent agreement is found between the GeN-IMM junction micro-element profiles and those from the full MD simulation. In the full MD simulation, the pressure and density profiles in the channel are not exactly linear, and (as in Chapter 2) this cannot be accurately captured in the GeN-IMM solution using a single micro-element. In each case, the channel micro-element measures the pressure at the midpoint in the channel; in Fig. 3.3, the location of the channel micro-elements have been laterally adjusted for clarity. The GeN-IMM transverse profiles for streamwise velocity and density in Fig. 3.4 also show excellent agreement with those from the full MD simulation, showing the accurate modelling of velocity slip and density-layering.

3.2.2 A bifurcating channel network

For the bifurcating network, one new test case (B3) is performed to solve for the conditions of the full MD simulation in case B1 (the bifurcating configuration). In this full MD simulation, the external boundary pressures are $P_1 = 565$ MPa, $P_7 = 135$ MPa, and $P_9 = 140$ MPa; the channel lengths are $L_1 = L_3 = L_4 = 68$ nm; and the channel heights are $H_1 = H_2 = H_3 = 4.08$ nm, $H_4 = H_6 = H_7 = 2.72$ nm, and $H_5 = H_8 = H_9 = 3.40$ nm. The full MD and generalised hybrid setup are shown in Fig. 3.5. For both the full and hybrid setup, the depth is constant at 5.44 nm. In component #2, the entrance/exit regions are constant and sufficiently large such that flow in the channel components is fully developed, as detailed in Chapter 2 and Appendix F. All channel micro-elements have a constant length of $L'_1 = L'_3 = L'_4 = 4.08$ nm (even if the length of the channel component is variable).

The GeN-IMM generalised constraints for case B3 are chosen to best demonstrate the generality of the method and its use as a design tool. The external boundary pressures are fixed to the aforementioned values; the mass flow rate through channel components #3 and #4 are fixed to $\dot{m}_4 = \dot{m}_6 = \dot{m}_7 = 0.9258$ ng/s and $\dot{m}_5 = \dot{m}_8 = \dot{m}_9 = 1.4691$ ng/s, respectively; the channel height in component #1 is fixed to $H_1 = H_2 = H_3 = 4.08$ nm; the channel lengths in components #3 and #4 are fixed to $L_3 = L_4 = 68$ nm; and the total volume of the three channel components #1, #3, and #4 is fixed to $V_1 + V_3 + V_4 = 3773.18$ nm^3. This means the outputs of the GeN-IMM solution are the internal boundary pressures, the length of the inlet channel component (#1), and the height of the outlet channel components (#3 and #4). The setup demonstrates some major benefits of the extended GeN-IMM by 1) removing the trial-and-error process necessary to meet desired mass flow rate constraints; and 2) enabling the quick and accurate design of multiple different physical properties (channel length, height, *and* pressure) that satisfy user-desired constraints. The initial flow-conductance coefficient estimates are the same as those used in cases B1 and B2 (i.e. those in Table 2.4). The initial prefactor estimates are shown in Table 3.9 using initial predictions for unknown channel geometry of $H_4 = H_6 = H_7 = 5.44$ nm (100% error), $H_5 = H_8 = H_9 = 5.44$ nm (60% error), and $L_1 = 102$ nm (50% error).

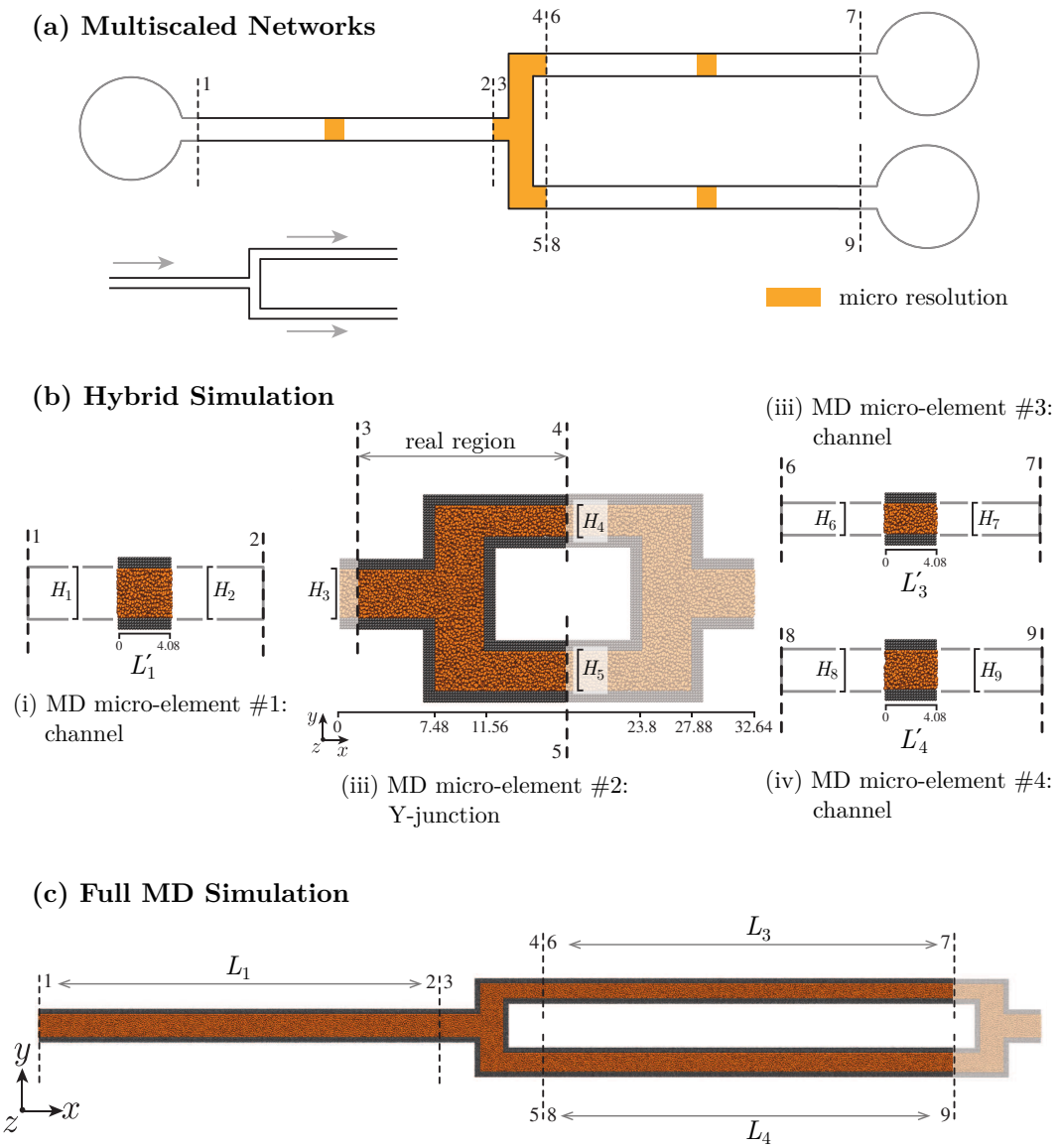

Figure 3.5: **(a)** Schematic of the bifurcating channel multiscale network with **(b)** the generalised hybrid GeN-IMM decomposition and **(c)** the full MD setup. Dimensions are in nanometers. The boundary numbers are also labelled in each image.

Table 3.9: Initial prefactors λ_{q_c}, $\Omega_{ij,q}$, and $\Psi_{ij,q}$ for the bifurcating channel network case B3.

Component # q	Boundary # i,j	prefactor λ_{q_c} ($\times 10^{-2}$ s/m)	prefactor $\Omega_{ij,q}$ ($\times 10^{5}$ s/m^2)	prefactor $\Psi_{ij,q}$ ($\times 10^{5}$ s/m^2)
1	1,2	-2.5953	-	-
2	3,4	-	-3.0867	-3.1698
2	3,5	-	-4.3799	-4.1969
2	4,5	-	-0.7754	-1.0445
3	6,7	-0.3062	-	-
4	8,9	-0.4891	-	-

The measured mass flow rate and pressure results for the GeN-IMM solution (at iteration 5) are shown in Tables 3.10 and 3.11, respectively. At all boundaries, the relative error to the full MD simulation is $< 1\%$, which presents a slight improvement from case B1 where the relative mass flow rate errors were between 1% and 2%. This improvement is expected because, in case B3, the target mass flow rates are specified as generalised constraints in two channels, and calculated by simple mass continuity in the third channel, so are not unknowns for the GeN-IMM to solve.

Table 3.10: Bifurcating channel network case B3: mass flow rate measurements for the GeN-IMM MD micro-elements (at iteration 5) and the full MD solution. Relative error calculated as $|\dot{m}_F - \dot{m}_i|/|\dot{m}_R| \times 100$.

Boundary #	Full MD $\dot{m}_F$ (ng/s)	GeN-IMM $\dot{m}_i$ (ng/s)	Relative error e_i (%)
1	2.3942	2.3968	0.11
2	2.3942	2.3968	0.11
3	2.3942	2.4049	0.44
4	0.9258	0.9247	0.05
5	1.4691	1.4808	0.49
6	0.9258	0.9253	0.02
7	0.9258	0.9253	0.02
8	1.4691	1.4713	0.09
9	1.4691	1.4713	0.09

Table 3.11: Bifurcating channel network case B3: pressure measurements for the GeN-IMM MD micro-elements (at iteration 5) and the full MD solution. Relative error calculated as $|P_F - P_i|/|P_R| \times 100$.

Boundary #	Full MD P_F (MPa)	GeN-IMM P_i (MPa)	Relative error e_i (%)
1	564.84	565.26	0.07
2	332.28	335.19	0.51
3	332.28	334.37	0.37
4	262.71	268.21	0.97
5	257.16	261.43	0.76
6	262.71	267.12	0.78
7	135.38	134.80	0.10
8	257.16	262.13	0.88
9	139.64	139.67	0.01

After five iterations, the channel length in component #1 converges to $L_1 = 67.06$ nm, compared to 68 nm in the full MD simulation: a relative error of 1.38%. This can be compared to a relative error of 50% for the initial channel length prediction. The heights of the outlet channels converge to $H_4 = H_6 = H_7 = 2.74$ nm and $H_5 = H_8 = H_9 = 3.44$ nm in components #3 and #4, respectively, compared to 2.72 nm and 3.4 nm in the full MD simulation. This produces relative errors of 0.61% and 1.16% for components #3 and #4, respectively, compared to initial prediction errors of 100% and 60%. The magnitude of these errors are in agreement with those found in Chapter 2, where the output variables all erred by $< 2\%$.

To determine convergence rate, equation (3.17) uses $\Gamma = L$ for component #1 (where the main output of the GeN-IMM solution is channel length), and $\Gamma = H$ for components #3 and #4 (where the main output is channel height). Figure 3.6 shows that all three geometric variables approximately converge to a tolerance of $\zeta^{\text{tol}} = 0.02$ after three iterations (although, in component #3, $\zeta = 0.0205$ is slightly above the prescribed tolerance). For component #2, convergence is considered by analysing the pressures at internal boundaries #3, #4, and #5. Figure 3.7 shows that convergence occurs comfortably after 2 iterations to a tolerance of $\zeta^{\text{tol}} = 0.02$. The faster convergence of pressure, compared to the geometrical variables, is likely due to the fixed upper and lower pressure limits at the external boundaries providing moderate constraints to the pressures at internal boundaries. Using the formula described in Chapter 2, case B3 has a speed-up $\tau_F/\tau_G = 2.1$ compared to the full MD simulation.

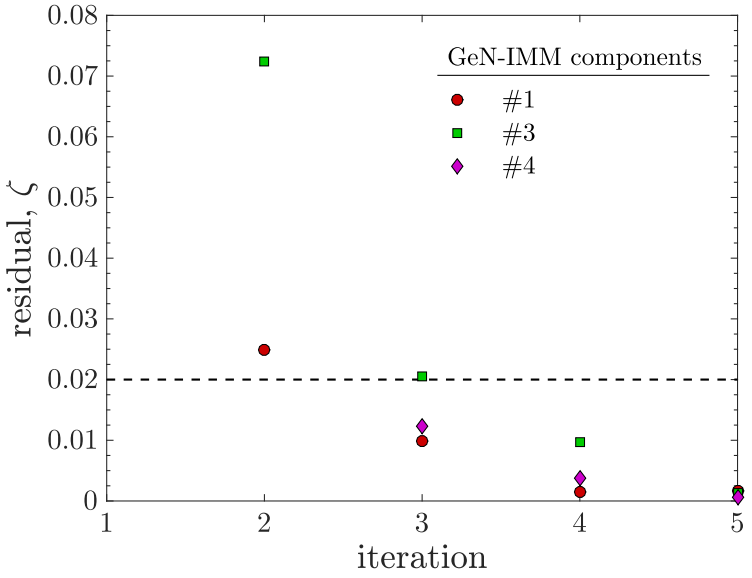

Figure 3.6: Bifurcating channel network case B3: geometric variable convergence of the GeN-IMM, with $\Gamma = L$ for component #1, and $\Gamma = H$ for components #3, and #4. The horizontal line is the prescribed tolerance ζ^{tol}.

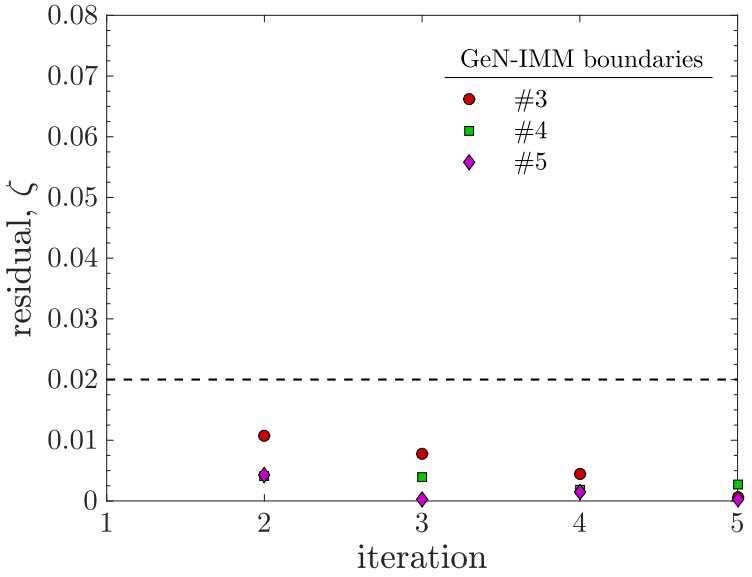

Figure 3.7: Bifurcating channel network case B3: internal boundary pressure convergence ($\Gamma = P$) of the GeN-IMM. The horizontal line is the prescribed tolerance ζ^{tol}.

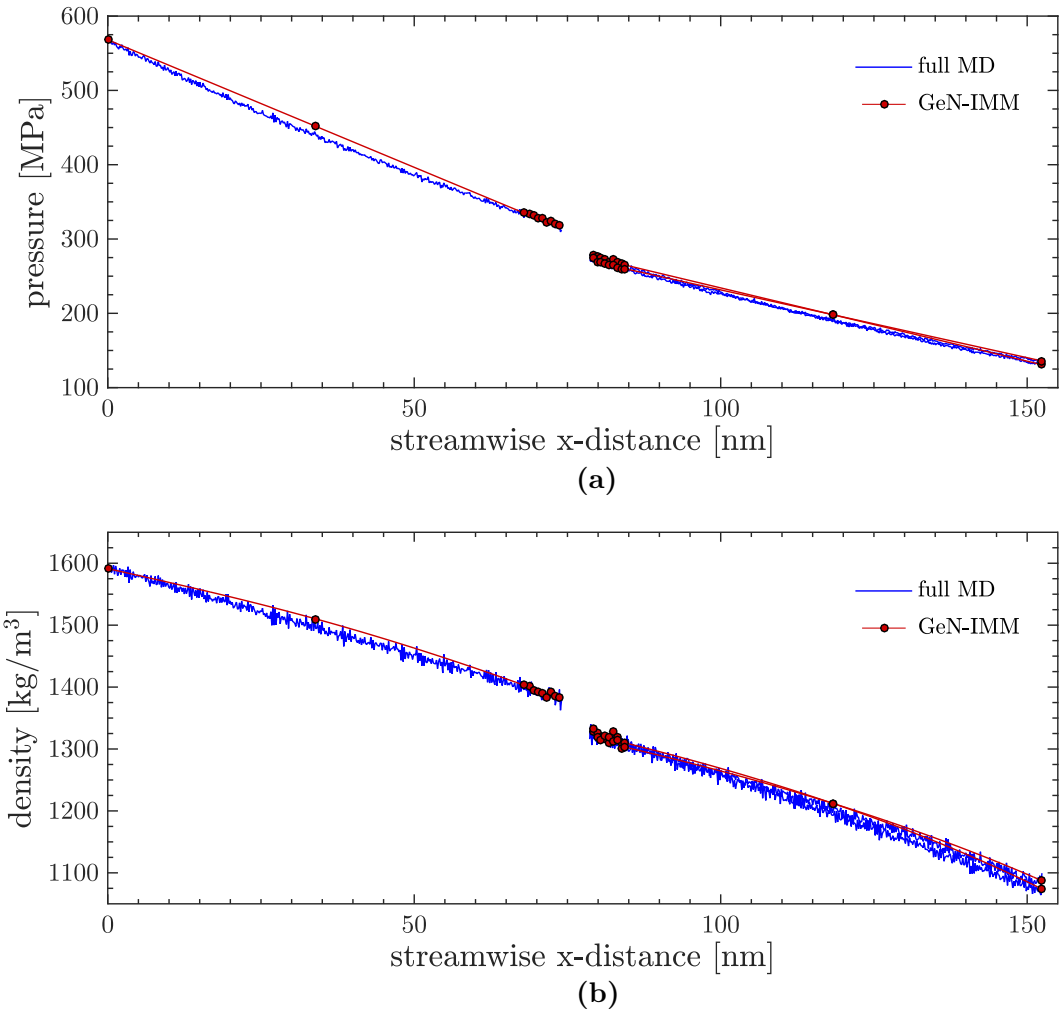

Figure 3.8: Bifurcating channel network case B3: longitudinal profiles of **(a)** pressure and **(b)** density (averaged over the cross-section). Measured in the GeN-IMM MD micro-elements (at iteration 5) and the full MD simulation. The GeN-IMM density profile in the channel section is generated using the equation of state (2.6).

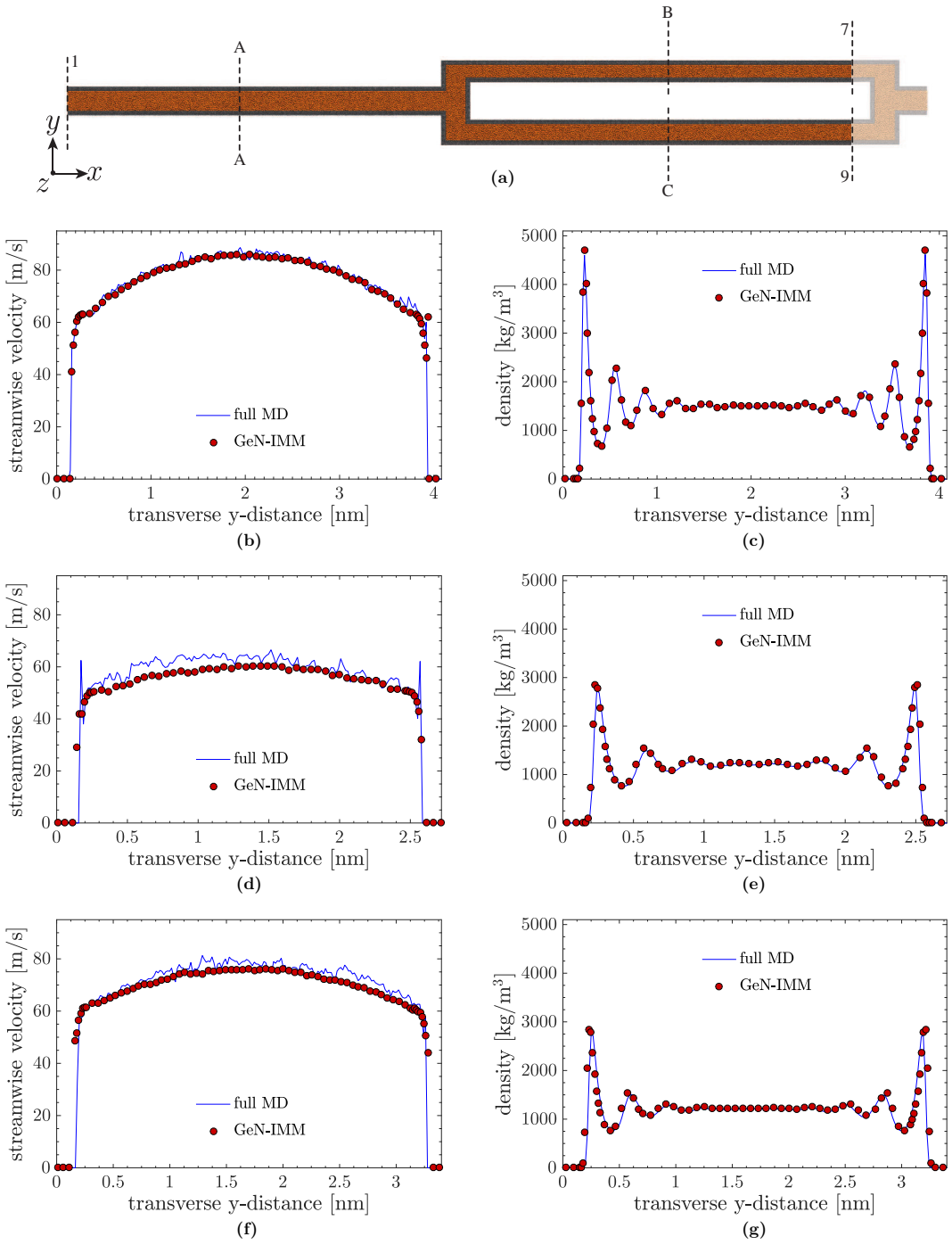

Figure 3.9: Bifurcating channel network case B3: **(a)** schematic showing location of measurement planes; transverse profiles of streamwise velocity and density at plane A-A **(b & c)**, plane B-B **(d & e)**, and plane C-C **(f & g)**. Measured in the GeN-IMM MD micro-elements (at iteration 5) and the full MD simulation.

The longitudinal pressure and density profiles for case B3 are displayed in Fig. 3.8. Once again, good agreement is found between the GeN-IMM solution and the full MD simulation. The two outlet pressures are similar in magnitude so the pressure and density profiles in components #3 and #4 overlap considerably.

Transverse profiles of streamwise velocity and density for case B3 iterations are shown in Fig. 3.9. In components #3 and #4, where there is a small error in the channel heights, the profiles are laterally adjusted so the centre of the channel is at the same location for the GeN-IMM micro-element and full MD measurements. The GeN-IMM micro-element velocity profiles show excellent agreement with the full MD simulation and present a minor improvement to the GeN-IMM velocity profiles in case B1. This is likely due to the increased accuracy of the mass flow rate at all boundaries in case B3. The density profiles also show good agreement between the hybrid and full simulations, but err slightly near the walls in components #3 and #4 due to the small discrepancy in channel height.

3.3 Summary

This chapter has presented an extension to the general networks internal-flow multiscale method (GeN-IMM), enabling its use as a design tool for high-aspect-ratio nanofluidic networks of arbitrary complexity. By allowing channel heights and lengths, and inlet and outlet pressures, to be outputs of the iterative procedure instead of fixed values, it removes the need for a costly trial-and-error process. To facilitate this generalisation of the hybrid method, a wide variety of macroscopic properties can be constrained, including mass flow rate and shear stress, which are critical properties to control in drug delivery and cell response applications, respectively.

The new methodology is verified against full MD simulations of the test networks introduced in Chapter 2. Four new cases with a variety of constraints were applied to the straight channel network (S2-S5). All cases converged to a solution after three iterations for a computational speed-up of 3.9, with an error relative to the full MD simulation of $< 1\%$ for all variables. One new case (B3) was applied to the bifurcating network. This case also displayed convergence after three iterations, for a speed-up of 2.1, and the relative error for all variables was $< 2\%$, and mostly $< 1\%$. The convergence rate and error magnitude of all the new cases exactly matched the GeN-IMM results in Chapter 2, demonstrating that this further generalisation of the method has not adversely affected its efficiency or precision.

Part II

Optimisation Principles for Fluidic Branching Networks

Abbreviations

Latin

A	Cross-sectional area $[m^2]$
a	Driving power constant $[kg/s]$
b	Branching position $[m]$ or maintenance power constant $[kg/s^3]$
C	Rectangular shape coefficient $[-]$
C_1, C_2, C_3	Constants [various]
$\mathcal{C}$	First-order slip coefficient $[-]$
D	Hydraulic diameter $[m]$
d	daughter channel outlet position $[m]$
f	Volumetric flow rate $[m^3/s]$
f_d	Darcy friction factor $[-]$
h	Channel depth $[m]$
$\mathcal{K}$	Murray's law constant $[s^{-1}]$
$\mathcal{K}'$	Minimum power constant $[m \cdot s^3 \cdot kg^{-1}]$
Kn	Knudsen number $[-]$
k	Flow resistance per unit length $[m^{-2} \cdot s^{-1}]$

L	Channel length $[m]$
$\mathcal{L}$	Characteristic length $[m]$
m	Metabolic coefficient $[kg \cdot m^{-1} \cdot s^{-3}]$ or flow consistency index $[Pa \cdot s]$
N	Number of daughter channels $[-]$
$\mathcal{P}$	Perimeter $[m]$
p	Parent channel inlet position $[m]$
Q	Mass flow rate $[kg/s]$
R	Channel internal radius $[m]$
R_{ext}	Channel external radius $[m]$
$\mathcal{R}$	Area-perimeter shape coefficient $[-]$
r	Radial coordinate $[m]$
S	Cross-sectional shape coefficient $[-]$
t	Time $[s]$
u	Streamwise velocity $[m/s]$
u_s	Slip velocity $[m/s]$
V	Volume $[m^3]$
W_f	Power to drive the fluid flow $[W]$
W_m	Power to maintain the fluid $[W]$
W_t	Total power $[W]$
w	Dimensionless wall thickness $[-]$
x, y, z	Cartesian coordinates $[m]$

Greek

α	Cross-section aspect ratio $[-]$
β	Network aspect ratio $[-]$
Γ	Daughter-parent area ratio $[-]$
δL	Infinitesimal length increment $[m]$
ΔP	Pressure drop $[Pa]$
η	Slip length $[m]$
θ	Branching angle $[^\circ]$ or azimuth $[^\circ]$
λ	Mean free path $[m]$
μ	Dynamic viscosity $[Pa \cdot s]$
ρ	Mass density $[kg/m^3]$
τ	Shear stress $[Pa]$
τ_w	Wall shear stress $[Pa]$
Φ	Daughter-daughter pressure gradient ratio $[-]$
Ψ	Daughter flow-rate fraction $[-]$
Ω	Daughter-parent length ratio $[-]$

Subscripts

b	Branching point
d	Daughter channel
i, j	Daughter channel index
p	Parent channel

Subscripts

b	Cross-section aspect-ratio index or flow behaviour index
n	Flow behaviour index

Accents

$\tilde{}$	Dimensionless value

Acronyms

LVDSMC	Low-variance deviational simulation Monte Carlo

Chapter 4

Introduction and Background

The optimal branching of fluidic networks has been the subject of numerous studies due to its importance in understanding the behaviour of biological vessels and maximising the efficiency of artificial systems through the application of biomimetic principles. Like the laws of Poiseuille and Fick, the first branching principles arose from a physiological context after noting that both large and small vessels are required in animal vasculature: the former to maximise advective transport (Poiseuille flow), and the latter to maximise surface area and minimise distances for diffusion (a Fickian process). It was posited that in an 'ideal' tissue there should be an optimal way to link the large (parent) and small (daughter) vessels together such that fluidic transport is maximised for the least amount of work. The first known attempt at such a general rule was by Young [1809], in which he proposed a symmetric bifurcating system where the diameter of each daughter branch is "about 4/5 of that of the trunk, or more accurately $1 : 1.26$." It was not mentioned whether this ratio stemmed from empirical or theoretical insight, nor is it remarked upon that it is approximately equal to $1 : 2^{1/3}$, but it subsequently appeared many times in the 20^{th} century. Despite having been attributed to Hess [1917], Blum [1919], and Thompson [1942] at various points in history, the most general derivation and most commonly cited origin of the minimum work branching principle was made by Murray [1926a,b], which for a symmetrically bifurcating channel reduces to the rules of Young [1809], Hess [1917], and Blum [1919]. In fact, in Murray's original paper, the optimisation is for a single channel and no daughter/parent ratio is explicitly stated, although a relationship is heavily implied. This relation, derived in the next section, is hereon referred to as *Murray's law*.

4.1 Murray's law

Murray [1926a] surmised that there were two competing factors contributing to the energy cost of blood flow through the arterial system: 1) the energy required to drive the flow, which increases as the vessel radius decreases; and 2) the energy required to metabolically maintain the fluid, which increases with increasing vessel radius. Thus to minimise the total power requirement, the vessel could be neither too large nor too small. Assuming the flow is laminar, Newtonian, steady, and fully developed, Poiseuille's law can be used to describe the flow through a cylindrical vessel:

$$\Delta P = \frac{8\mu L f}{\pi R^4}, \tag{4.1}$$

where ΔP is the pressure drop over the vessel, μ is the viscosity of the fluid, L is the vessel length, f is the volumetric flow rate, and R is the vessel radius. The power W_f required for the flow to overcome the viscous drag is then

$$W_f = f\Delta P = \frac{8\mu L f^2}{\pi R^4}. \tag{4.2}$$

This is offset by the maintenance 'cost of blood' W_m which increases linearly with the blood volume:

$$W_m = mL\pi R^2, \tag{4.3}$$

where m is an all-encompassing metabolic coefficient that includes the chemical cost of keeping the blood constituents fresh and functional, and the general cost owing to the weight of blood. The total power requirement $W_t = W_f + W_m$ is then

$$W_t = \frac{af^2}{R^4} + bR^2, \tag{4.4}$$

where $a = 8\mu L/\pi$ and $b = m\pi L$. For a constant volumetric flow rate, and given values of a and b, the total power will be a function of a single variable: the vessel radius R. The minimum power is then found by differentiating with respect to R and equating to zero:

$$\frac{\mathrm{d}W_t}{\mathrm{d}R} = \frac{-4af^2}{R^5} + 2bR = 0. \tag{4.5}$$

Rearranging equation (4.5) gives

$$f = \mathcal{K}R^3, \tag{4.6}$$

where $\mathcal{K} = \sqrt{b/2a}$. Thus for any vessel considered independently, equation (4.6) describes the optimal relation between volumetric flow rate and vessel radius, such that the power requirement is minimised. If the fluid viscosity and metabolic coefficient are constant throughout a network, then $\mathcal{K}$ is constant. It was hypothesised that, in this instance, equation (4.6) should hold for all vessels, or as Murray [1926a] put it: "We see one of the simplest requirements for maximum efficiency in the circulation – namely that the blood flow past any section shall everywhere bear the same relation to the cube of the radius of the vessel at that point". The relation this statement implies was, to the author's knowledge, first explicitly written in Murray's later paper on optimal bifurcating angles [Murray, 1926c], and was later popularised by many authors ([Rosen, 1967; Kamiya and Togawa, 1972; Milsum and Roberge, 1973; Rashevsky, 1973; Kamiya et al., 1974; Hutchins et al., 1976; Zamir, 1976a,b, 1977, 1978; Hooper, 1977; Uylings, 1977; Sherman, 1981]). The conservation of mass at the branching point gives

$$f_p = \sum_{i=1}^{N} f_{d_i}, \tag{4.7}$$

where the subscripts p and d_i denote the parent and i^{th} of N daughters, respectively. If equation (4.6) applies to every vessel in a branching system, then substituting in equation (4.7) gives the ubiquitous Murray's law:

$$R_p^3 = \sum_{i=1}^{N} R_{d_i}^3. \tag{4.8}$$

Equation (4.6) is also sometimes referred to as Murray's law, but as this thesis focuses on branching networks, Murray's law will refer exclusively to equation (4.8). As it was derived from the optimisation of a single channel, Murray's law does not make any assumptions regarding the form of the branching system, i.e. whether branching is symmetric or not, or whether branching is bifurcating or not. However, as will be shown in Chapters 5 and 6, Murray's law is in fact sub-optimal for asymmetric branching as, in this case, the optimal solution for each channel considered independently is not the same as the global optimum for the network. As noted by Sherman [1981], for a symmetric bifurcating network (i.e. $N = 2$ and $R_{d_i} = \text{const}$), equation (4.8) reduces to the $1 : 2^{1/3}$ daughter-parent radius ratio rule of Young [1809].

Murray's law has been shown to compare well against quantitative data for a range of biological networks whose primary function is fluidic transport: in the cardiovascular systems of multiple animals, including man, monkey, dog, pig, rabbit

and rat [Hutchins et al., 1976; Zamir et al., 1979; Zamir and Brown, 1982; Zamir and Medeiros, 1982; Zamir et al., 1983, 1984; Sherman, 1981; Mayrovitz and Roy, 1983; Zamir and Chee, 1986; LaBarbera, 1990; Kassab and Fung, 1995]; in the bronchial trees of lungs in humans and dogs [Miller, 1893, 1937; Weibel and Gomez, 1962; Weibel, 1963; Wilson, 1967; Horsfield and Cumming, 1967, 1968; Horsfield et al., 1976; Horsfield, 1978]; in the chick embryo [Taber et al., 2001]; and in the leaf veins of plants [McCulloh et al., 2003, 2004; McCulloh and Sperry, 2005]. In general, statistical estimates from biological data samples have found the exponent in equation (4.8) to vary mostly between 2.7 and 3.2 [Suwa et al., 1963; Hutchins et al., 1976; Sherman, 1981].

Sherman [1981] suggested that Murray's law could also be applied to inorganic systems, making it a useful biomimetic design tool. Murray's law describes the power balance between the competing costs of driving and maintaining the fluid (equations (4.2) and (4.3), respectively); for inorganic systems, the problem lies in determining a maintenance cost in terms of the internal vessel radius, as there is likely no metabolic requirement for the fluid. However, this is also the case for air transport through the bronchial tree and water transport through lumen, both of which have shown to be decently approximated by Murray's law. In these instances, the maintenance cost represents the need for general upkeep of the vessel and the burden due to the weight of the fluid and vessel, i.e. it is more accurately a function of the external vessel radius. Sherman [1981] posited that it will often be the case that the vessel wall width is approximately linearly proportional to the internal radius. In this case, the external radius can be expressed as $R_{ext} = (1 + w)R$, where wR is the wall thickness, and Murray's law can be reclaimed by incorporating the factor $(1 + w)$ into the metabolic coefficient m in equation (4.3). This means that Murray's law can be applied to a range of systems so long as either 1) the fluid, 2) the vessel wall, or 3) a combination of the two can be ascribed some form of maintenance cost.

4.2 Extensions of Murray's law and other optimisation principles

Since the original derivation of Murray's law, it has been noted that the application of other optimisation principles, not just that of minimum work, result in the $2^{1/3}$ law of Young [1809] for symmetric branching, e.g. minimising the total mass of the network [Williams et al., 2008], minimising pumping power [Gosselin and Bejan, 2005], minimising the entropy generation [Zimparov et al., 2006], minimising the

volume [Kamiya and Togawa, 1972], maintaining a constant shear stress in all channels [Zamir, 1977], and minimising the flow resistance [Cohn, 1954, 1955; Sherman, 1981; Bejan, 2000; Bejan et al., 2000]. In addition, a number of optimisations have been presented that extend the principles of Murray and other authors to consider different geometries, scales, and fluid models.

4.2.1 Non-circular cross sections

While most biological networks exhibit circular cross-sectional areas, Emerson et al. [2006] extended Murray's law to networks of rectangular and trapezoidal cross-sectional area in order to apply the biomimetic principle to the design of microfluidic networks and lab-on-a-chip systems. These devices are becoming increasingly prominent in engineering due to their high performance and functionality, including being utilised for microreactors [Renault et al., 2012], tissue engineering [Diaz Lantada et al., 2013], fuel cells [Senn and Poulikakos, 2004], and electronic cooling [Chen and Cheng, 2002; Wang et al., 2006]. Having noted from Zamir [1977] and Sherman [1981] that an output of Murray's law is for the shear stress to remain constant throughout the network, non-circular cross sections were considered by maintaining a constant average shear stress around the wetted perimeter. This enabled analytical expressions for optimal branching to be stated in terms of an equivalent hydraulic diameter. The analysis uses Poiseuille's law, with the total resistance through multilevel bifurcating networks obtained using the analogy between pipe friction and electrical resistance (where the pressure drop is analogous to the potential difference and the flow rate analogous to the electrical current), combined with the assumption that channel lengths are proportional to their hydraulic diameters. Analytical expressions were compared to computational fluid dynamics simulations that solve the non-linear Navier-Stokes equations, and excellent agreement is shown for Reynolds numbers below ~ 30.

The limitation of this method is that for nanofluidic networks (length scales below $\sim$ 10 nm) and rarefied gas flows (Knudsen numbers above ~ 0.1), the no-slip condition breaks down and the fluid no longer behaves as a continuum, i.e. Poiseuille's law and the Navier-Stokes equations are not valid. In addition, the assumption that shear stress remains constant through the network is incorrect (see Chapter 5). This means that as lab-on-a-chip devices become increasingly small to further improve on efficiency and process control, the optimal solutions presented by Emerson et al. [2006] become inaccurate. Furthermore, as will be shown in Chapter 6, the assumption that the channel length varies linearly with its hydraulic diameter is oversimplified and not always precise.

4.2.2 Non-continuum flows

The influence of non-continuum effects in optimal branching networks is not a well developed research area, but is an increasingly important one for the biomimetic design of artificial systems. Gosselin and da Silva [2007] produced a numerical solution for dendritic structures by maximising mass flow rate for a constant pressure drop and network volume. The setup consists of a fixed number of users positioned equidistantly around the perimeter of a circular disk, with the fluid source located at the disk centre. Using an expression for mass flow rate proposed by Karniadakis et al. [2005], which is valid for Knudsen numbers up to ~ 10, multilevel symmetric bifurcating networks of cylindrical pipes were globally optimised for the branching points and pipe diameters using a genetic algorithm toolbox in MATLAB®. The results showed a departure from the continuum solutions for both the optimal radius ratio (i.e. Murray's law) and the optimal branching angle (see §4.2.4) as rarefaction increased.

The limitation of these results is that they 1) are only valid for channels of circular cross section, 2) are only valid up to a Knudsen number of ~ 10, 3) are only valid for bifurcating networks, and 4) only afford a numerical solution. In chapter 5, a generalised analytical branching law is derived that is applicable for any cross-sectional shape, any number of daughter channels, and any length scale/Knudsen number, all the way up to the free-molecular limit.

4.2.3 Non-Newtonian fluids and turbulent flows

In reality, whole blood (plasma and cells) is a non-Newtonian fluid that exhibits shear thinning characteristics, i.e. its viscosity decreases with increased shear-strain rate. To more accurately consider vascular networks, the minimum work principle of Murray's law has been applied to non-Newtonian fluid flows [Revellin et al., 2009; Tesch, 2010] through the use of the popular power-law fluid model [Ostwald, 1925; de-Waele, 1923]. While the maintenance cost remained unchanged (i.e. equation (4.3)), the cost of driving the fluid through a pipe was based on the flow of a power law fluid, rather than Poiseuille flow. By analytically optimising for a single channel, both studies found that $f \propto R^3$ regardless of the shear thinning or shear thickening behaviour of the fluid, and thus equation (4.8) is maintained for the whole range of non-Newtonian fluids.

The optimisation of turbulent fluidic networks, which can be found in the upper airways of the lung [Olsen et al., 1970], in blood flow through the aorta [Stein and Sabbah, 1976], and in a number of hydraulic and pneumatic engineering

applications, was first considered by Uylings [1977] using the principle of minimum work. Replacing the Poiseuille equation with the Darcy-Weisbach equation, the cost of driving turbulent flow through a pipe was analytically determined, while the maintenance cost remained unchanged from its laminar flow form. By optimising for a single channel, Uylings [1977] found that for fully-rough-wall turbulent flow, the flow rate is proportional to $R^{7/3}$, leading to the relation

$$R_p^{7/3} = \sum_{i=1}^{N} R_{d_i}^{7/3}, \tag{4.9}$$

for branching networks. Other authors [Bejan et al., 2000; Williams et al., 2008] have since obtained the same relation using the principles of minimum resistance and minimum mass, but only for symmetric branching (i.e. $R_{d_i} = \text{const}$).

The studies of Revellin et al. [2009], Tesch [2010], and Uylings [1977] share the same problem with Murray's original law in that the independent optimisation of a single channel does not result in the global optimum for asymmetric branching. In chapter 6, the generalised law (developed in Chapter 5) is applied to non-Newtonian and full-rough-wall turbulent fluidic networks to demonstrate that the previous literature is sub-optimal for asymmetric branching and that optimal branching is dependent on the shear thinning/thickening behaviour of a non-Newtonian fluid.

4.2.4 Optimal angles

Optimal branching angles were first considered by applying the principle of virtual work to a two-level bifurcating network with the positions of the parent channel inlet (p) and daughter channel outlets (d_1 and d_2) fixed [Murray, 1926c]. Consider the network shown in Fig. 4.1, with channel lengths L_p, L_{d_1}, and L_{d_2}, and channel radii R_p, R_{d_1}, and R_{d_2} for the parent, first daughter, and second daughter channels, respectively. Assuming laminar, Newtonian, steady, and full-developed flow, substituting equation (4.6) into equation (4.4) gives a relationship between the minimum power requirement per unit length and the radius:

$$\frac{\mathcal{K}' W_t}{L} = R^2, \tag{4.10}$$

where $\mathcal{K}' = 3\pi m/2$. Supposing the network in Fig. 4.1 represents the condition for minimum work, Murray [1926c] surmised that increasing the length of the parent channel by an infinitesimal distance δL_p would incur a power cost in the parent channel of $\delta L_p R_p^2$, while the cost of the daughter channels approximately reduce by $\delta L_p R_{d_1}^2 \cos\theta_{d_1}$ and $\delta L_p R_{d_2}^2 \cos\theta_{d_2}$, respectively. By the principle of virtual work,

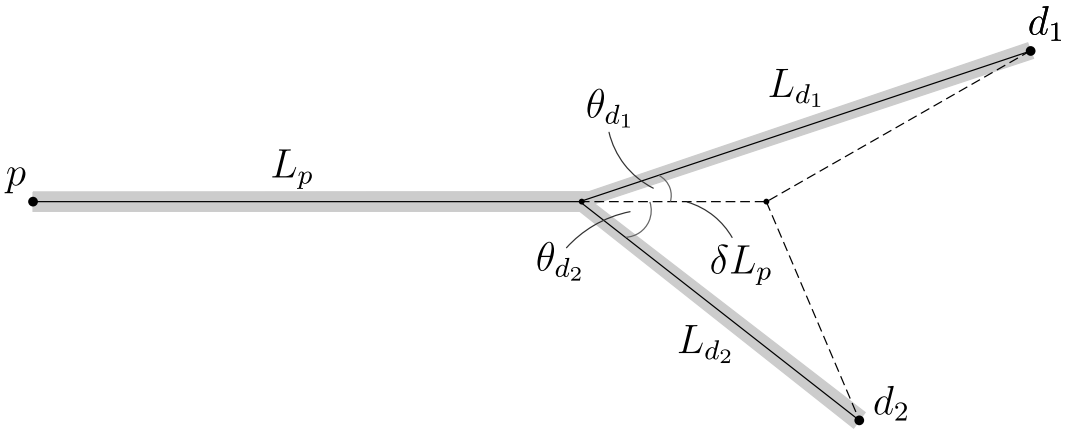

Figure 4.1: Schematic showing the asymmetric bifurcation of a network, with a fixed parent inlet position at p and fixed daughter outlet positions at d_1 and d_2.

which states that the virtual work is zero for all virtual movements of a system from static equilibrium (i.e. $\delta W_t = 0$), the following three equation can be derived by infinitesimally increasing the lengths of each channel in turn:

$$\delta L_p R_p^2 = \delta L_p R_{d_1}^2 \cos\theta_{d_1} + \delta L_p R_{d_2}^2 \cos\theta_{d_2}, \tag{4.11}$$

$$\delta L_{d_1} R_{d_1}^2 = -\delta L_{d_1} R_{d_2}^2 \cos\theta + \delta L_{d_1} R_p^2 \cos\theta_{d_1}, \tag{4.12}$$

$$\delta L_{d_2} R_{d_2}^2 = -\delta L_{d_2} R_{d_1}^2 \cos\theta + \delta L_{d_2} R_p^2 \cos\theta_{d_2}, \tag{4.13}$$

where $\theta = \theta_{d_1} + \theta_{d_2}$. Combining equations (4.11)-(4.13) gives the optimal branching angle:

$$\cos\theta = \frac{R_p^4 - R_{d_1}^4 - R_{d_2}^4}{2R_{d_1}^2 R_{d_1}^2}. \tag{4.14}$$

For symmetric branching, equation (4.14) becomes

$$\cos\theta = \frac{R_p^4 - 2R_d^4}{2R_d^4}, \tag{4.15}$$

and substituting in Murray's law (equation (4.8)) for the daughter-parent radius ratio (i.e. the $2^{1/3}$ rule) gives

$$\cos\theta = 2^{1/3} - 1, \tag{4.16}$$

or $\theta \approx 74.93°$.

Other authors have since performed analytical optimisations for a symmetrically bifurcating network under the same flow conditions. The optimisation principles can broadly be divided into three categories: the minimisation of work [Uylings,

1977], the minimisation of drag force [Zamir, 1976a], and the minimisation of volume [Horsfield and Cumming, 1967; Kamiya and Togawa, 1972]. The result of the minimum volume optimisation is the same as that of minimum work, i.e. equation (4.16). For the minimum drag force (which produces the same result as minimising surface area) the optimisation gives $\cos\theta = 2^{-1/3} - 1$ or $\theta \approx 101.91°$. The limitation of these methods is that they are only accurate for macroscopic networks, where the continuum approximation is valid, and only for channels with a circular cross section. In chapter 6, the generalised law is extended to consider the optimal branching angles for a symmetrically bifurcating network of channels with any cross-sectional shape, at any length scale.

Chapter 5

The Generalised Law for Branching Networks of all Shapes and Sizes

Despite the overall acceptance of Murray's law, and its numerous subsequent developments, it will be demonstrated in this chapter that it is in fact sub-optimal for asymmetric branching. In addition, there are two major barriers that prevent Murray's law from being relevant to the design of many artificial fluidic networks: 1) it is not applicable to arbitrary cross sections; and 2) it is not applicable at the micro/nanoscale, where a fluid can no longer be accurately described as a continuous material [Gad-el Hak, 1999].

5.1 Analytical solutions

The conditions for optimal branching can be generalised as a maximisation of flow conductance per unit volume, for a variety of constraint combinations. For a two-level network (consisting of a single parent channel branching into multiple daughter channels) this can be expressed as

$$\underset{\Gamma_j \in [0,\infty]}{\arg\max} \left[\frac{Q}{\Delta P V} \right] \text{ subject to fixed } \begin{cases} Q, \Delta P \\ V, \Delta P \\ V, Q \end{cases} \tag{5.1}$$

where Q is the mass flow rate through the parent channel, ΔP is the total pressure drop (from inlet of the parent to the outlet of the daughters), V is the network

volume and

$$\Gamma_j = \frac{A_{d_j}}{A_p} \tag{5.2}$$

is the j^{th} daughter-parent cross-sectional area ratio. Note, the three constraint options (pressure-drop minimisation, volume minimisation, and flow-rate maximisation) all lead to an identical optimal relation. For the optimisation, it is assumed that the channel lengths L are large compared to the size of the parent-daughters junction so that 1) the localised pressure losses at the junction are negligible compared to the pressure drops over individual channels, and 2) the volume of the network can be considered to be the sum of the channel volumes:

$$V = A_p L_p + \sum_{i=1}^{N} A_{d_i} L_{d_i}. \tag{5.3}$$

The channel lengths are treated as being independent of the optimal daughter-parent area ratio (as found in Murray's optimisation [Murray, 1926a]), i.e. $\mathrm{d}L/\mathrm{d}\Gamma_j = 0$. This will be verified later. Consider the optimisation of the j^{th} daughter channel: inserting equation (5.3) into the fitness function of equation (5.1), differentiating with respect to Γ_j and equating to zero gives

$$\frac{\mathrm{d}}{\mathrm{d}\Gamma_j}\left(\frac{\Delta P V}{Q}\right) = L_p \frac{\mathrm{d}A_p}{\mathrm{d}\Gamma_j} + \sum_{i=1}^{N} L_{d_i} \frac{\mathrm{d}A_{d_i}}{\mathrm{d}\Gamma_j} = 0, \tag{5.4}$$

noting that, for all constraint combinations, $\mathrm{d}(\Delta P)/\mathrm{d}\Gamma_j = 0$ and $\mathrm{d}Q/\mathrm{d}\Gamma_j = 0$. The pressure drop over the parent and each of the i daughter channels can be expressed in terms of the mass flow rate:

$$\Delta P_p = Q L_p k_p, \tag{5.5}$$

$$\Delta P_{d_i} = \Psi_i Q L_{d_i} k_{d_i}, \tag{5.6}$$

where $\Psi_i = Q_{d_i}/Q$ is the fraction of the total flow rate taken by the i^{th} daughter channel and k is flow resistance per unit length, e.g. $k_p = \Delta P_p/(QL_p)$. The pressure drop over the entire network $\Delta P = \Delta P_p + \Delta P_{d_i}$ is then

$$\Delta P = Q\left(L_p k_p + \Psi_i L_{d_i} k_{d_i}\right). \tag{5.7}$$

As $\mathrm{d}(\Delta P)/\mathrm{d}\Gamma_j = \mathrm{d}Q/\mathrm{d}\Gamma_j = 0$, differentiating equation (5.7) with respect to Γ_j gives

$$L_p \frac{\mathrm{d}k_p}{\mathrm{d}\Gamma_j} + \Psi_i L_{d_i} \frac{\mathrm{d}k_{d_i}}{\mathrm{d}\Gamma_j} = 0. \tag{5.8}$$

Substituting equation (5.8) into equation (5.4), via the chain rule, gives the generalised optimal area ratio

$$\left.\frac{\mathrm{d}A}{\mathrm{d}k}\right|_p = \sum_{i=1}^{N} \frac{1}{\Psi_i} \left.\frac{\mathrm{d}A}{\mathrm{d}k}\right|_{d_i}, \tag{5.9}$$

which, for brevity, will be referred to as the *generalised law* to distinguish it from Murray's law. This generalised law is valid for any cross-sectional shape, for any fluid (e.g. non-Newtonian), and for any Reynolds number (e.g. for turbulent flow). It should be noted that the subscript j is not present in equation (5.9), so this relationship is not specific to a particular daughter channel; it relates properties of *all* daughter channels to that of the parent.

For clarity, the generalised law has been derived here with the assumption that the pressure drop over all daughter channels is equal. It is possible, though, that a non-uniform distribution of downstream pressure could exist. In this case, the derivation is identical to that above, except that the pressure drop ΔP featuring in equations (5.1) and (5.7) is replaced with the total pressure drop over a reference parent-daughter branch. The final result is independent of the choice of reference branch, and identical to equation (5.9).

When the branching is symmetric, $\Psi_i = 1/N$ for all i daughter channels, and equation (5.9) simplifies to

$$\left.\frac{\mathrm{d}A}{\mathrm{d}k}\right|_p = N^2 \left.\frac{\mathrm{d}A}{\mathrm{d}k}\right|_d. \tag{5.10}$$

The focus of this chapter is laminar and Newtonian flows, and the next section considers some important cases where A can be expressed easily as an analytical function of k.

5.1.1 The continuum-flow limit

At the continuum-flow limit, the steady Navier-Stokes momentum equation describes laminar flow through a long channel with an arbitrary cross-sectional shape, i.e.

$$\frac{\Delta P}{L} = -\mu \nabla^2 u\,, \tag{5.11}$$

where μ is the dynamic viscosity and u is the streamwise channel velocity. This can be non-dimensionalised using $\Delta P/L$, μ and cross-sectional area A, such that

$$1 = -\tilde{\nabla}^2 \tilde{u}, \tag{5.12}$$

where

$$u = \tilde{u}A\left(\frac{\Delta P}{L}\right)\frac{1}{\mu}; \qquad \nabla^2 = \frac{\tilde{\nabla}^2}{A}, \tag{5.13}$$

and tilde denotes a dimensionless quantity or operator. The axes of the cross-sectional plane are defined as y, z, and

$$y = \tilde{y}\sqrt{A}; \qquad z = \tilde{z}\sqrt{A}. \tag{5.14}$$

Provided the boundary conditions are fixed (which is the case for the continuum-flow limit, where the no-slip boundary condition applies), the solution of equation (5.12), $\tilde{u}(\tilde{y}, \tilde{z})$, is independent of A, ΔP, L, and μ, and is thus a property of the cross-sectional shape alone. Similarly, so is

$$S = \iint_A \tilde{u}\,(\tilde{y}, \tilde{z})\ \mathrm{d}\tilde{y}\,\mathrm{d}\tilde{z}\,. \tag{5.15}$$

An expression for the mass flow rate is obtained by integrating the fluid momentum over the cross-sectional area

$$Q = \rho \iint_A u\,\mathrm{d}y\,\mathrm{d}z, \tag{5.16}$$

where ρ is the mass density. Substitution of equations (5.13)-(5.15) into (5.16) gives the mass flow rate for an arbitrary cross-sectional shape:

$$Q = \rho A^2\left(\frac{\Delta P}{L}\right)\frac{S}{\mu}, \tag{5.17}$$

and flow resistance per unit length:

$$k = \frac{\mu}{\rho S A^2}. \tag{5.18}$$

It is assumed that the pressure drop over the network is small such that the viscosity and density are constants. For channels with a circular cross section $S = 1/8\pi$, and equation (5.17) becomes the Hagen-Poiseuille flow rate. In this chapter, it is also assumed that the cross-sectional shape is constant throughout the network, i.e. $S = \text{const}$. Substituting (5.18) into the generalised law (5.9) and cancelling the constant terms gives

$$A_p^3 = \sum_{i=1}^{N} \frac{1}{\Psi_i} A_{d_i}^3. \tag{5.19}$$

From equation (5.6), it can be seen that

$$\frac{\Delta P_{d_i}}{\Psi_i L_{d_i} k_{d_i}} = \text{const} \tag{5.20}$$

for all daughter channels. Combining equations (5.18) and (5.20) produces the cross-sectional area relationship between the i^{th} and j^{th} daughter channels:

$$A_{d_i} = A_{d_j} \sqrt{\frac{\Psi_i \Phi_{ij}}{\Psi_j}}, \tag{5.21}$$

where

$$\Phi_{ij} = \frac{\left(\Delta P_{d_j}/L_{d_j}\right)}{\left(\Delta P_{d_i}/L_{d_i}\right)} \tag{5.22}$$

is the pressure gradient ratio between the j^{th} and i^{th} daughter channels. Note that as the shape property S cancels in equation (5.21), the generalised law will be independent of the cross-section shape of the channels at the continuum-flow limit. Substituting equation (5.21) into equation (5.19) and rearranging for Γ_j as defined by equation (5.2) gives

$$\Gamma_j = \sqrt{\Psi_j} \left[\sum_{i=1}^{N} \Phi_{ij} \sqrt{\Psi_i \Phi_{ij}} \right]^{-1/3}. \tag{5.23}$$

Equation (5.23) relates the area of the parent channel to the area of the j^{th} daughter channel in an optimised two-level network at the continuum-flow limit. It is valid for any cross-sectional shape, provided the shape is constant through the network. Equation (5.23) is only equivalent to Murray's law (which is $\Gamma_j = \Psi_j^{2/3}$ when posed in terms of an area ratio) if the daughter channels branch symmetrically, i.e. $\Psi_i = \Psi_j = 1/N$ and $\Phi_{ij} = 1$. By inserting these constraints into equation (5.23), the symmetric generalised law branching relation for the continuum-flow limit is

$$\Gamma = N^{-2/3}. \tag{5.24}$$

This means that for symmetric branching, Murray's law is valid for any cross-sectional shape, not just circles. The reason Murray's law produces a sub-optimal result for asymmetric branching is that it was derived to optimise a single channel in isolation. Over time this has been misinterpreted as a general branching law (for symmetric *and* asymmetric configurations) due to the prevalence of the form shown in equation (4.8). However, as shown above (and verified later), for asymmetric branching, the global optimum is not the same as the optimum for each channel

considered separately.

By combining equations (5.17) and (5.24) with a force balance relating the pressure drop to the wall shear:

$$A\Delta P = L\tau_w \mathcal{P}, \tag{5.25}$$

where $\mathcal{P}$ is the perimeter of the section and τ_w is the wall shear stress, it can be shown that the wall shear stress is constant through the network at the continuum-flow limit for symmetric branching, i.e.

$$\tau_d = \tau_p, \tag{5.26}$$

agreeing with previous studies [Zamir, 1977].

5.1.2 The plug-flow limit

For the other limiting case of scale, channel flow becomes plug-like as the velocity profile is dominated by velocity slip at the walls. The wall slip velocity u_s and wall shear stress τ_w are near-uniform around the perimeter of the cross section, and can be related by

$$\tau_w = \frac{u_s \mu}{\eta}, \tag{5.27}$$

where η is the slip length determined by the fluid-solid interaction. Note, the value of η does not affect the optimal area ratio solution at the plug-flow limit, and thus accurate knowledge of it is not required. As the flow tends to the plug-flow limit, the mass flow rate is simply

$$Q = \rho A u_s. \tag{5.28}$$

Combining equations (5.27), (5.28) with a force balance (equation (5.25)) gives

$$Q = \rho \eta A^{3/2} \left(\frac{\Delta P}{L}\right) \frac{\mathcal{R}}{\mu}, \tag{5.29}$$

and flow resistance per unit length:

$$k = \frac{\mu}{\rho \eta \mathcal{R} A^{3/2}}, \tag{5.30}$$

where $\mathcal{R} = \sqrt{A}/\mathcal{P}$ is a property of the cross-sectional shape (like S). As before, considering the case where the shape remains the same throughout the network, equations (5.30) and (5.20) can be substituted into the generalised law (5.9) to get

the plug-flow limit:

$$\Gamma_j = \Psi_j^{2/3} \left[\sum_{i=1}^{N} \Phi_{ij} \left(\Psi_i \Phi_{ij} \right)^{2/3} \right]^{-2/5}. \tag{5.31}$$

For symmetric branching, the plug-flow limit becomes

$$\Gamma = N^{-4/5}. \tag{5.32}$$

By substituting equations (5.29) and (5.25) into equation (5.32), it can be seen that, even in the case of symmetric branching, the wall shear stress is not constant through the network at the plug-flow limit:

$$\tau_d = N^{-1/5} \tau_p. \tag{5.33}$$

5.1.3 A slip-flow approximation

In the transition between the continuum- and plug-flow limits, the flow is neither completely dominated by velocity slip, nor is the slip velocity zero. A solution of the Navier-Stokes equations with a Navier slip boundary condition ($\tau_w = u_s \mu / \eta$) is referred to as a slip solution. For the sake of simplicity, the slip solutions will be derived for symmetric branching only. A simple approximation to the exact slip solution, for any cross section, can be obtained by assuming that the shear stress, and thus the velocity slip, is constant around the perimeter, i.e.

$$Q \approx \frac{\rho \Delta P A^2}{L \mu \mathcal{P}} \left(S\mathcal{P} + \eta \right). \tag{5.34}$$

This gives the exact mass flow rate of the slip solution for a circular cross section (which has a uniform shear stress) and accurate approximations for rectangles of any aspect ratio (within 3% of results from a finite-difference slip solver). Note, the slip solution is itself an approximation, and particularly for gas flows must be treated with caution, as discussed later. Equation (5.34) can be rearranged to give the flow resistance per unit length:

$$k = \frac{\mu \mathcal{P}}{\rho A^2 \left(S\mathcal{P} + \eta \right)}. \tag{5.35}$$

Inserting equation (5.35) into the (symmetric) generalised law (equation (5.10)) for parent and daughter channels, produces the general slip solution for the optimal

daughter-parent area ratio for all cross-sectional shapes, across all length-scales:

$$\Gamma^3 \left[\frac{\eta \left(2\mathcal{P}_p - A_p \frac{\mathrm{d}\mathcal{P}}{\mathrm{d}A}\Big|_p \right) + \mathcal{P}_p^2 \left(A_p \frac{\mathrm{d}S}{\mathrm{d}A}\Big|_p + 2S_p \right)}{\left(S_p \mathcal{P}_p + \eta \right)^2} \right] = N^{-2} \left[\frac{\eta \left(2\mathcal{P}_d - A_d \frac{\mathrm{d}\mathcal{P}}{\mathrm{d}A}\Big|_d \right) + \mathcal{P}_d^2 \left(A_d \frac{\mathrm{d}S}{\mathrm{d}A}\Big|_d + 2S_d \right)}{\left(S_d \mathcal{P}_d + \eta \right)^2} \right]. \quad (5.36)$$

In this chapter, it is assumed that the cross-sectional shape S is constant throughout the network, so $S_p = S_d$ and $\mathrm{d}S/\mathrm{d}A = 0$ in equation (5.36).

Circular cross section

For a circular cross section, $A = \pi R^2$, $S = 1/8\pi$, $\mathcal{P} = 2\sqrt{\pi A}$, and $\mathrm{d}\mathcal{P}/\mathrm{d}A = \sqrt{\pi/A}$. Substituting these values into equation (5.36) and simplifying produces

$$\Gamma^{5/2} = N^{-2} \left(\frac{\tilde{R}_p \sqrt{\Gamma} + 3}{\tilde{R}_p + 3} \right) \left(\frac{\tilde{R}_p + 4}{\tilde{R}_p \sqrt{\Gamma} + 4} \right)^2, \quad (5.37)$$

where $\tilde{R}_p = R_p/\eta$ is the dimensionless radius of the parent channel.

Rectangular cross section

For rectangular cross-sections of variable depth h and constant aspect ratio $\alpha = A/h^2$, $\mathcal{P} = 2(\alpha + 1)h$, $\mathrm{d}\mathcal{P}/\mathrm{d}A = (\alpha + 1)h/A$, and an accurate approximation of S (from White [1974]) is

$$S \approx \frac{1}{4\alpha^b} \left[\frac{1}{3} - \frac{64}{\pi^5 \alpha^b} \tanh \left(\frac{\pi \alpha^b}{2} \right) \right] \text{ where } b = \begin{cases} 1 \text{ for } \alpha \geq 1 \\ -1 \text{ for } \alpha < 1 \end{cases} \quad (5.38)$$

Equation (5.38) only includes the first term of an infinite series, but as the denominators of higher terms increase exponentially, the expression is sufficient. Substituting these values into equation (5.36) and simplifying gives an optimal area relation of

$$\Gamma^{5/2} = N^{-2} \left(\frac{4C\tilde{h}_p \sqrt{\Gamma} + 3}{4C\tilde{h}_p + 3} \right) \left(\frac{C\tilde{h}_p + 1}{C\tilde{h}_p \sqrt{\Gamma} + 1} \right)^2, \quad (5.39)$$

where $\tilde{h}_p = h_p/\eta$ is the dimensionless depth of the parent channel and $C = 2S(\alpha+1)$ is a constant.

5.2 Numerical verification and discussion

An accurate numerical optimisation procedure is used to demonstrate the following: a) Murray's law is sub-optimal for asymmetric branching; b) the generalised law (equation (5.9)) is applicable to asymmetric branching, arbitrary cross-sectional shapes, and for all scales; c) the scale limits of the generalised law, identified as the continuum-flow limit (equation (5.24)) and the plug-flow limit (equation (5.32)), are valid and precise for all shapes considered; d) the approximate slip solutions to the generalised law (equations (5.37) and (5.39)) provide reasonable accuracy, even for rarefied gas flows.

The numerical optimisation procedure verifies the analytical results by algorithmically finding the parent and daughter areas that, in combination, maximise the mass flow rate through the network for the following fixed properties: total volume, pressure drop(s), channel lengths, mass-flow-rate distribution (between daughters), and fluid/flow properties. The model of the network assumes that channels are sufficiently long such that localised pressure losses at the parent-daughters junction can be considered negligible compared to the pressure drop over the channels themselves. This allows a model for a two-level network to be constructed from predictions of mass flow rate through individual channels, coupled by a common branching pressure P_b and the requirement for mass continuity.

The numerical optimisation procedure is based on calculations that use non-dimensional mass flow rates, i.e.

$$\tilde{Q} = \frac{Q\mu L}{\rho A^2 \Delta P}. \tag{5.40}$$

These mass flow rate are obtained either from published sources, from high-resolution finite-difference slip solutions, from exact analytical expressions, or from stochastic particle calculations (for dilute gases). For each shape and physical model an interpolant is constructed that provides the non-dimensional mass flow rate for any given area, $\tilde{Q}(A)$. From this, equation (5.40) can be evaluated for parent and daughter channels (assuming the pressure drops over all daughter channels are equal):

$$\Delta P_p = \frac{Q\mu L_p}{\tilde{Q}(A_p)\rho A_p^2}, \tag{5.41}$$

$$\Delta P_d = \frac{Q\mu L_d}{N\tilde{Q}(A_d)\rho A_d^2}. \tag{5.42}$$

Combining equations (5.41) and (5.42) and substituting for the total pressure drop $\Delta P = \Delta P_p + \Delta P_d$ produces a model of the mass flow rate through a two-level

network for a particular cross-sectional shape and physical model:

$$Q = \frac{\rho \Delta P}{\mu} \left[\frac{L_p}{\tilde{Q}(A_p) {A_p}^2} + \frac{L_d}{N \tilde{Q}(A_d) A_d^2} \right]^{-1}. \tag{5.43}$$

For symmetric branching, $\Psi_i = 1/N$ and the volume constraint requires $L_p A_p = V - N A_d L_d$; for asymmetric branching, equation (5.43) must be solved simultaneously for each daughter i, and with the general volume expression of equation (5.3). The optimal parent and daughter areas are then found using an interior-point constrained optimization algorithm [Waltz et al., 2005] in MATLAB®.

If the pressure drops acting over the daughter channels are different then the numerical procedure becomes more complicated as a simple expression for mass flow rate in terms of the total pressure drop ΔP (i.e. equation (5.43)) will not exist as the branching pressure is unknown. In this case, a more brute force approach is required, which is outlined in Appendix H.

5.2.1 Asymmetric bifurcations

To demonstrate that Murray's law is sub-optimal, the first set of numerical optimisation results are for an asymmetrically bifurcating network of channels with arbitrary cross-sectional shape at the continuum-flow limit. The numerical optimisation uses mass flow rates calculated from a standard central-difference solution of the laminar Navier-Stokes equations (5.11) with a Navier slip boundary condition. For Murray's law, mass conservation provides the closure $R_{d_i}^3 = R_{d_j}^3 (1 - \Psi_j)/\Psi_j$, which leads to

$$\Gamma_j = \Psi_j^{2/3}. \tag{5.44}$$

In Fig. 5.1, to induce asymmetry, the daughter flow-rate fraction Ψ_j is varied while the daughter-daughter pressure gradient ratio is kept constant at $\Phi_{ij} = 1$.

Each method shows that the greater the fraction of flow through the daughter channel, the greater the optimum daughter's area (relative to the parent), as is intuitive. The results confirm the finding that Murray's law is, in fact, only valid for symmetric bifurcations ($\Psi_j = 0.5$); for a flow-rate percentage of 10% ($\Psi_j = 0.1$), Murray's law under predicts the optimum daughter area by as much as 26%. In contrast, the generalised law is accurate for all values of Ψ_j. This corroborates the evaluation that Murray's law has been mistakenly applied to asymmetrically branching networks, where the optimised result for each individual channel is not optimal for the network as a whole.

This can be further demonstrated by inducing asymmetry by varying the

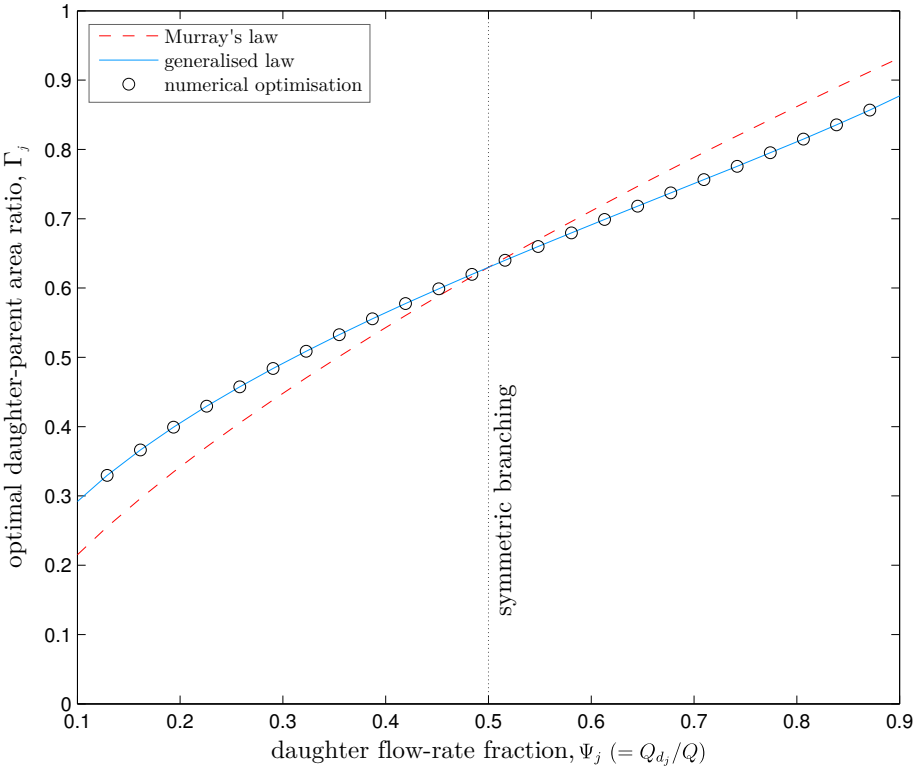

Figure 5.1: Optimal daughter-parent area ratio Γ_j against daughter flow-rate fraction Ψ_j at the continuum-flow limit, in a two-level bifurcating network of channels with arbitrary, but constant, shape and equal daughter channel pressure gradients ($\Phi_{ij} = 1$). Plotted for Murray's law (equation (5.44)), the generalised law (equation (5.23)), and results from the numerical optimisation.

daughter-daughter pressure gradient ratio Φ_{ij}, while the daughter flow-rate fraction is kept constant at $\Psi_j = 0.5$, as shown in Fig. 5.2. Murray's law does not consider Φ_{ij} to be a variable that affects the optimal daughter-parent area ratio Γ_j and shows a notable departure from the numerical optimisation results; e.g. for a pressure gradient ratio of $\Phi_{ij} = 2$, Murray's law over predicts the optimum daughter area by 24%. In contrast, the generalised law is accurate for all values of Φ_{ij} and, as expected, shows that the optimal area of the j^{th} daughter channel decreases when it has a larger pressure gradient relative to the other daughter channel, as the mass flow rate flowing through each daughter must be equal (because $\Psi_j = \Psi_i = 0.5$). This result is the same whether the pressure gradient is altered by varying the relative daughter channel lengths or the pressure drops. The results in Figs. refasymFig and 5.2 are consistent regardless of the daughter and parent channel length magnitudes,

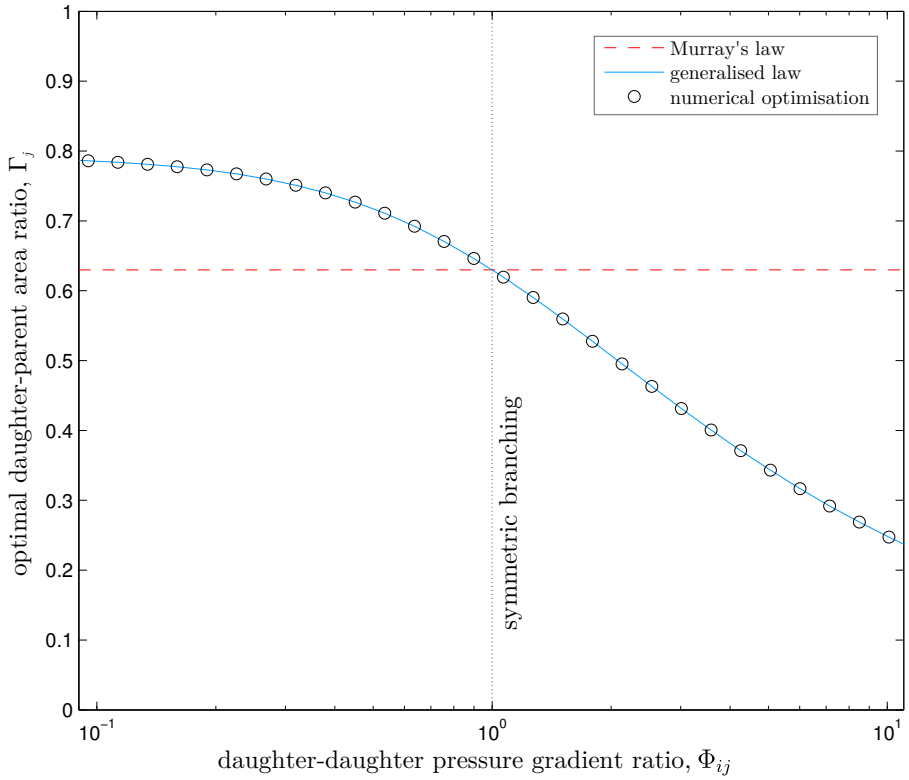

Figure 5.2: Optimal daughter-parent area ratio Γ_j against daughter-daughter pressure gradient ratio $\Phi_{ij} = (\Delta P_{d_j}/L_{d_j})/(\Delta P_{d_i}/L_{d_i})$ at the continuum-flow limit, in a two-level bifurcating network of channels with arbitrary, but constant, shape and equal mass flow rate taken by each daughter channel ($\Psi_j = 0.5$). Comparison of Murray's law (equation (5.44)), the generalised law (equation (5.23)), and the results from the numerical optimisation.

demonstrating that the optimal daughter-parent area ratio is independent of the lengths, as was asserted in the analytical solution. Figures 5.1 and 5.2 both show that as the extent of asymmetry increases, Murray's law provides a poorer estimate of the optimal area ratio.

5.2.2 Different shapes and sizes

Murray's original derivation was for circular channel sections at the continuum-flow limit. The next set of numerical optimisation results are presented to verify that the generalised law is valid for a variety of cross-sectional shapes across all length scales. Again, the numerical optimisation uses mass flow rates calculated from a central-difference solution of the laminar Navier-Stokes equations with velocity slip. The

results from the analytical and numerical optimisations, for symmetric bifurcations (i.e. $N = 2$), are presented in Fig. 5.3.

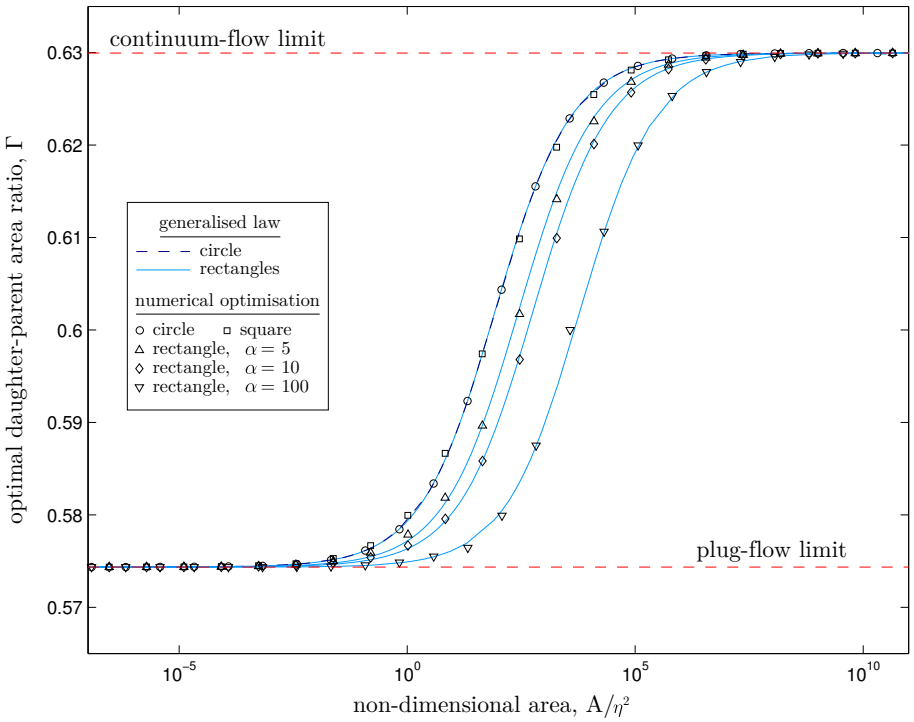

Figure 5.3: Optimal daughter-parent area ratio Γ against non-dimensional parent area for a symmetrically bifurcating network with a constant cross-sectional shape. Comparison of the approximate slip solution to the generalised law (equations (5.37) and (5.39)) and numerical optimisation using data from a Navier-Stokes slip solver. Plotted for circles, squares, and rectangles of aspect ratio $\alpha = 5$, $\alpha = 10$, and $\alpha = 100$.

For large parent areas, relative to the square of the slip length η, the optimum daughter-parent area ratio converges to the continuum-flow limit of the generalised law (equation (5.24)) for all shapes considered. The same is true for the other extreme of scale: the optimum area ratio for all shapes converges to the plug-flow limit of the generalised law (equation (5.32)) for small parent areas.

In the transition between these limits, the approximate slip solutions to the generalised law are also highly accurate. The difference between the analytical solutions and the numerical optimisations is less than 0.1% across the entire range of scales for all shapes tested. Clearly, predictions for the optimum dimensions are not particularly sensitive to errors introduced by the approximation of (5.34).

In Fig. 5.3, it is observed that for networks of channels with rectangular

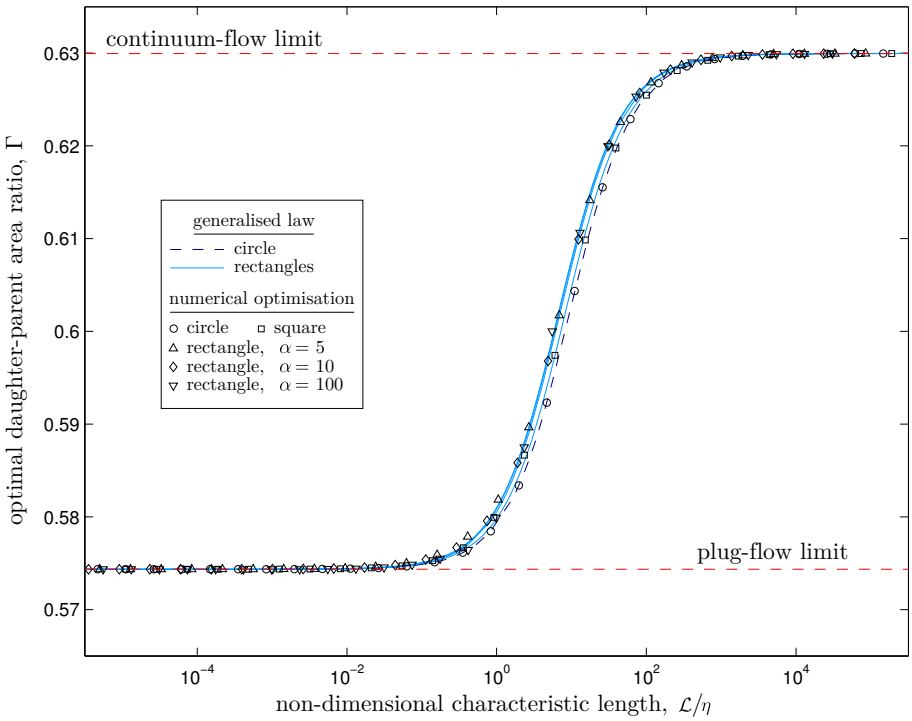

Figure 5.4: Optimal daughter-parent area ratio Γ (for a constant aspect ratio) against non-dimensional characteristic length for a symmetrically bifurcating network. Comparison of the approximate slip solution to the generalised law (equations (5.37) and (5.39)) and numerical optimisation using data from a Navier-Stokes slip solver. Plotted for circles, squares, and rectangles of aspect ratio $\alpha = 5$, $\alpha = 10$, and $\alpha = 100$.

cross sections, the aspect ratio affects the range of areas for which Γ is in the transition period between the continuum- and plug-flow limits. This occurs because the influence of slip is governed by the size of the *smallest* cross-sectional length scale (hereon referred to as the characteristic length $\mathcal{L}$) relative to the slip length. So, for the same cross-sectional area, the characteristic length of a rectangle with a high-aspect-ratio is less than the characteristic length of a low-aspect-ratio rectangle. This means that optimal branching of high-aspect-ratio channels will depart from the continuum-flow limit and approach the plug-flow limit at larger parent areas than for optimal branching in low-aspect-ratio channels. This is further evidenced by plotting Γ against the non-dimensional characteristic length. Figure 5.4 shows that, despite the wide range of aspect ratios, all of the shapes tested depart from the continuum-flow limit and approach the plug-flow limit at approximately the same non-dimensional characteristic length. For the circular cross-section networks, the

characteristic length is taken to be the diameter.

5.2.3 Rarefied gas flow

The numerical optimisation is now performed for symmetric branching of rarefied gas flows. For dilute gases, the slip length can be related to the mean free path λ via $\eta = \mathcal{C}\lambda$, where $\mathcal{C} = 1.11$ is the first-order slip coefficient for the hard-sphere model of gases with purely diffuse molecular reflection at walls [Hadjiconstantinou, 2003]. The mass-flow-rate data is obtained from a variety of sources, including the author's own simulations, computed using a version of low-variance deviational simulation Monte Carlo (LVDSMC) [Radtke et al., 2011] [1]. In Fig. 5.5, additional mass-flow-rate data is procured from the solution of the linearised Boltzmann equation [Loyalka and Hamoodi, 1990, 1991] and the S-model [Sharipov, 1996] to verify the accuracy of the LVDSMC results.

The results of the analytical and numerical optimisations, for circular cross-sections, are presented in Fig. 5.5. To demonstrate that the generalised law is valid for any number of daughter branches ($N \geq 2$), Γ is plotted for $N = 2$, $N = 3$ and $N = 5$ and, for clarity, is normalised with respect to the continuum-flow limit ($N^{-2/3}$). Again, the agreement between the numerical optimisation and the plug-flow limit of the generalised law is excellent for each case considered. It is perhaps unexpected that a slip solution to the generalised law should converge to the same result as that of kinetic theory and LVDSMC at the free-molecular limit, given the approximate nature of slip boundary condition at such scales. However, as $\tilde{R}_p \to 0$, Γ in equation (5.37) becomes independent of the slip length η, and is thus unaffected by any inaccuracy in the slip model. Due to computational cost, molecular simulations are not performed for sufficiently large areas to see the solution meet the continuum-flow limit; but, since the results from kinetic theory converge to the solution of the slip model, agreement at the continuum-flow limit is also expected. It is well known that when the Knudsen number $\mathrm{Kn} = \lambda/\mathcal{L}$ is much greater than $\sim$0.1, slip solutions become inaccurate, explaining the departure in Γ between the limits. The kinetic-theory and LVDSMC results all show a minimum in Γ beneath the plug-flow/free-molecular limit. This is possibly a manifestation of the Knudsen minimum [Knudsen, 1909], a rarefied gas phenomenon that occurs when the diffusive flux starts to dominate the convective flux as length scale decreases [Mitra and Chakraborty, 2012].

[1] The author's LVDSMC simulations used periodic boundary conditions in the streamwise direction, 10 deviational particles per cell, a cell size of $\Delta x = \lambda/5$, and a time-step of $\Delta t = \Delta x/\bar{c}$, where $\bar{c}$ is the most probable thermal velocity.

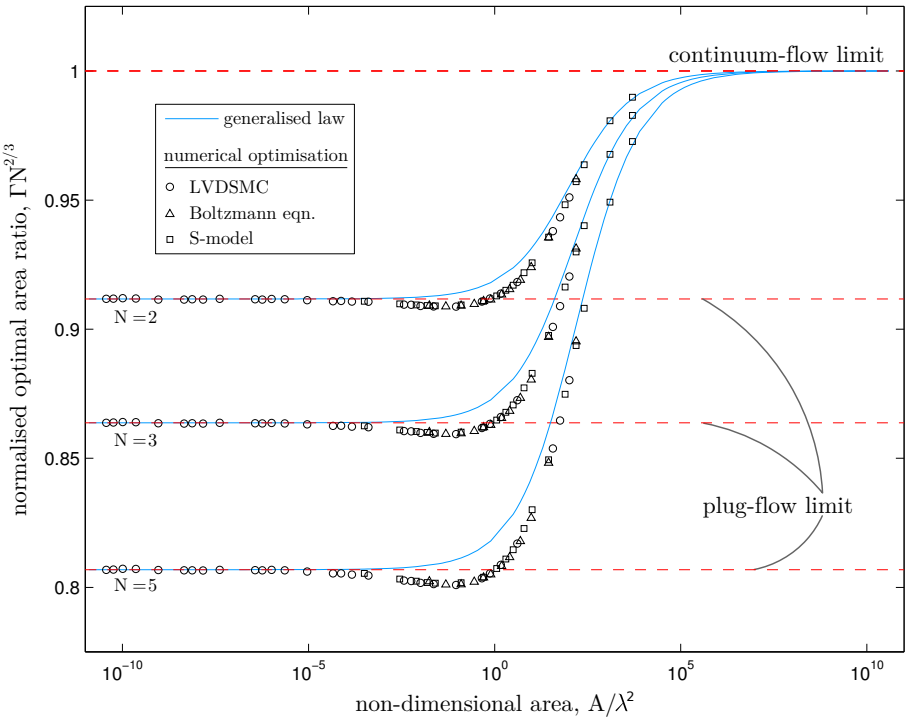

Figure 5.5: Normalised optimal daughter-parent area ratio against non-dimensional parent area for a symmetrically branching network of channels with a circular cross section. Comparison of the analytical slip solution to the generalised law (equation (5.37)) and the numerical optimisation using data from kinetic theory [Loyalka and Hamoodi, 1990; Sharipov, 1996] and LVDSMC. Plotted for $N = 2$, $N = 3$ and $N = 5$.

Similar results are also found in networks with rectangular geometries, as shown in Fig. 5.6. Again, the LVDSMC numerical optimisation agrees with the slip solution at the plug-flow limit for multiple numbers of daughter branches, and separates from the slip solution between the length-scale limits. Minimum values of Γ, below that of the plug-flow limit, are also exhibited. This minimum occurs at a larger area for the higher aspect ratio network, likely due to relative size of the characteristic length. The departure from the slip solution at the minimum increases with aspect ratio. This provides further evidence for a link between the Γ minimum and the Knudsen minimum, as the depth of the Knudsen minimum is also noted to increase with aspect ratio [Mitra and Chakraborty, 2012].

Note, although equations (5.37) and (5.39) are only approximate between the scale limits, the precise result of the numerical optimisation can be reclaimed by expressing the kinetic theory mass flow rate data in terms of flow resistance per unit

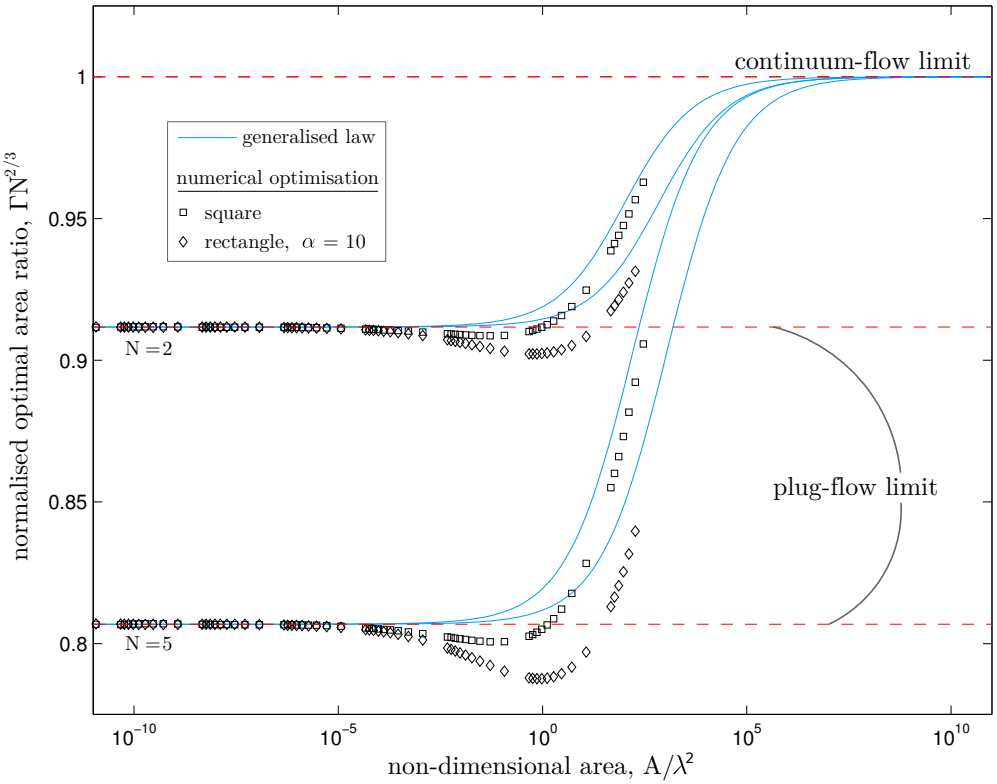

Figure 5.6: Normalised optimal daughter-parent area ratio against non-dimensional parent area for a symmetrically branching network of channels with a rectangular cross section. Comparison of the analytical slip solution to the generalised law (equation (5.37)) and the numerical optimisation using data from kinetic theory [Loyalka and Hamoodi, 1990; Sharipov, 1996] and LVDSMC. Plotted for squares and rectangles of aspect ratio $\alpha = 10$ at $N = 2$ and $N = 5$.

length, $k(A)$. By interpolating between data points, the (symmetric) generalised law in equation (5.10) can be evaluated, but this does not afford an analytical relation.

5.3 Summary

In this chapter, a generalised optimisation principle has been derived that leads to analytical expressions for the optimum daughter-parent area ratio Γ for any shape, at any length scale, and for any number of daughter branches.

Analytical solutions have been verified with a numerical optimisation and shown that, for symmetric branching at the continuum-flow limit, this is equivalent to Murray's law, where $\Gamma = N^{-2/3}$. However, when applied to an asymmetrically branching network, i.e. when the flow rate is not evenly divided between daughter

channels (or the daughter channels do not have equal pressure gradients), it has been shown that Murray's law is sub-optimal. This is because, for asymmetric branching, the global optimisation of the entire network is not equal to the local optimisation of each individual channel, which Murray's law presumes.

Unlike the generalised law presented, Murray's law is also sub-optimal for slip flows and plug flows that occur at smaller length scales, where the optimal daughter-parent area ratio converges to $\Gamma = N^{-4/5}$. The new optimal design relation proposed can be used as a biomimetic design principle to be applied to a variety of micro and nanofluidic networks that require non-circular geometry, due to manufacturing constraints, and are designed for increasingly smaller scales in order to achieve a greater degree of control, functionality, and analytical and economic efficiency.

Chapter 6

Applications of the Generalised Law

In this chapter, the generalised law, which is recalled as

$$\left.\frac{\mathrm{d}A}{\mathrm{d}k}\right|_p = \sum_{i=1}^{N} \frac{1}{\Psi_i} \left.\frac{\mathrm{d}A}{\mathrm{d}k}\right|_{d_i}, \quad \text{for asymmetric branching,} \tag{6.1}$$

$$\left.\frac{\mathrm{d}A}{\mathrm{d}k}\right|_p = N^2 \left.\frac{\mathrm{d}A}{\mathrm{d}k}\right|_d, \quad \text{for symmetric branching,} \tag{6.2}$$

is applied to more complicated fluidic networks to further demonstrate its utility for a range of technologically and biologically important applications. The optimisation principle is considered for three distinct branching cases: 1) rectangular cross-sectional networks which have a constant depth rather than a constant shape — a common constraint for lab-on-a-chip fabrication procedures; 2) networks for non-Newtonian fluid flows — the most prominent application being blood flow; and 3) networks for turbulent fluid flows — important for a number of hydraulic and pneumatic engineering applications. In addition, to further aid network design, the optimal branching angle and daughter-parent channel length ratios will be analysed for a range of shapes and length scales.

In each section, an analytical solution will be derived from the generalised law and numerically verified by the procedures outlined in §5.2 and Appendix H. While the generalised law is accurate for all cases, it will be shown that 1) Murray's law is inaccurate for constant-depth networks; 2) The misinterpretation of Murray's law as an asymmetric branching rule has endured in subsequent literature for non-Newtonian fluids and turbulent flows; and 3) Murray's law only accurately finds the optimal branching angle at the continuum-flow limit.

6.1 Constant-depth networks

As noted by Emerson et al. [2006], in some circumstances it is desirable or necessary for the shape to vary between parent and daughter channels. In most lab-on-a-chip fabrication procedures (e.g. photolithograpy, wet or dry etching, or surface micromachining) the depth remains constant throughout the device, and thus the shape of the cross-section must vary. A multi-depth approach to fabrication does exist [Lim et al., 2003], but it is relatively complex.

6.1.1 Analytical solution

For a constant-depth network, the optimal branching behaviour depends on the change in shape between the parent and daughter channels, which is a function of the aspect ratio $\alpha = A/h^2$ for rectangular channels. This leads to two aspect-ratio limits for Γ (at each of the continuum- and plug-flow length-scale limits), as illustrated in Fig. 6.1. For simplicity, only symmetric branching is considered.

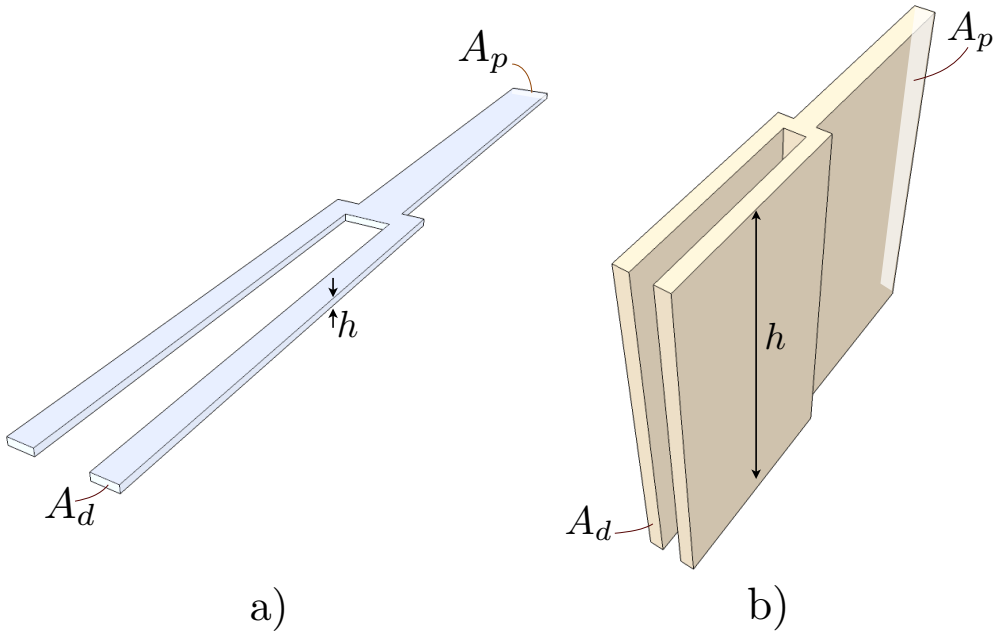

Figure 6.1: Schematic showing the symmetric bifurcation of constant-depth rectangular channels of a) high aspect ratio ($\alpha \gg 1$); and b) low aspect ratio ($\alpha \ll 1$).

Continuum-flow limit

At the continuum-flow limit, it is recalled from §5.1.1 that the flow resistance per unit length k is

$$k = \frac{\mu}{\rho S A^2}, \tag{6.3}$$

and, for a variable aspect ratio α, the shape property S for a rectangle can be written as

$$S \approx \frac{h^{2b}}{4A^b}\left[\frac{1}{3} - \frac{64h^{2b}}{\pi^5 A^b}\tanh\left(\frac{\pi A^b}{2h^{2b}}\right)\right] \text{ where } b = \begin{cases} 1 \text{ for } \alpha \geq 1 \\ -1 \text{ for } \alpha < 1 \end{cases} \tag{6.4}$$

where h is the constant network depth. It is clear from equation (6.4) that, at the aspect-ratio limits, the shape property reduces to

$$S = \frac{h^2}{12A}, \text{ for } \alpha \gg 1; \tag{6.5}$$

$$S = \frac{A}{12h^2}, \text{ for } \alpha \ll 1. \tag{6.6}$$

As S is no longer a constant, the generalised law must consider the change in shape between parent and daughter channels:

$$\frac{\mathrm{d}S}{\mathrm{d}A} = \frac{-bh^{2b}}{4A^{b+1}}\left[\frac{1}{3} - \frac{128h^{2b}}{\pi^5 A^b}\tanh\left(\frac{\pi A^b}{2h^{2b}}\right) + \frac{32}{\pi^4}\operatorname{sech}^2\left(\frac{\pi A^b}{2h^{2b}}\right)\right]. \tag{6.7}$$

At the aspect-ratio limits, equation (6.7) reduces to

$$\frac{\mathrm{d}S}{\mathrm{d}A} = -\frac{h^2}{12A^2}, \text{ for } \alpha \gg 1; \tag{6.8}$$

$$\frac{\mathrm{d}S}{\mathrm{d}A} = \frac{1}{12h^2}, \text{ for } \alpha \ll 1. \tag{6.9}$$

Substituting equations (6.3), (6.5), and (6.8) into the symmetric generalised law (equation(6.2)), via the chain rule, gives the high-aspect-ratio continuum-flow limit:

$$\Gamma = N^{-1}. \tag{6.10}$$

Incidentally, this limit is equal to da Vinci's rule of tree branching [Eloy, 2011]. Similarly, substituting equations (6.3), (6.6), and (6.9) into the symmetric generalised law gives the low-aspect-ratio continuum-flow limit:

$$\Gamma = N^{-1/2}. \tag{6.11}$$

These limits are both different to the continuum-flow limit derived for constant-aspect-ratio networks in Chapter 5, which was equivalent to Murray's law for symmetric branching.

Plug-flow limit

At the plug-flow limit, it is recalled from §5.1.2 that the flow resistance per unit length k for a rectangular cross section is

$$k = \frac{2\mu h\,(\alpha+1)}{\rho\eta A^2}, \tag{6.12}$$

where the perimeter is

$$\mathcal{P} = 2h\,(\alpha+1)\,. \tag{6.13}$$

Noting again that $\alpha = A/h^2$, it is clear from equation (6.12) that, at the aspect-ratio limits, k reduces to

$$k = \frac{2\mu}{\rho\eta h A}, \text{ for } \alpha \gg 1; \tag{6.14}$$

$$k = \frac{2\mu h}{\rho\eta A^2}, \text{ for } \alpha \ll 1. \tag{6.15}$$

Substituting equation (6.14) into the symmetric generalised law gives

$$\Gamma = N^{-1}, \tag{6.16}$$

for the high-aspect-ratio plug-flow limit. Interestingly, the high-aspect-ratio limits are the same for continuum and plug flow. Similarly, substituting equation (6.15) into the symmetric generalised law gives

$$\Gamma = N^{-2/3}, \tag{6.17}$$

for the low-aspect-ratio plug-flow limit. Once again, these limits are both different to the plug-flow limit for constant-aspect-ratio networks derived in Chapter 5.

A slip-flow approximation

In the transition between the length-scale limits, a slip solution — obtained by assuming that the shear stress (and thus velocity slip) is constant around the perimeter — was shown in Chapter 5 to be an accurate model. Substituting equation (6.13)

and $\mathrm{d}\mathcal{P}/\mathrm{d}A = 2/h$ into the general slip solution (equation (5.36)) gives

$$\Gamma^3 \left[\frac{2\tilde{h}\left(\alpha_p + 2\right) + 4\tilde{h}^2\left(\alpha_p + 1\right)\left(A_p \frac{\mathrm{d}S}{\mathrm{d}A}\Big|_p + 2S_p\right)}{\left(2\tilde{h}S_p\left(\alpha_p + 1\right) + 1\right)^2} \right] = N^{-2} \left[\frac{2\tilde{h}\left(\alpha_d + 2\right) + 4\tilde{h}^2\left(\alpha_d + 1\right)\left(A_d \frac{\mathrm{d}S}{\mathrm{d}A}\Big|_d + 2S_d\right)}{\left(2\tilde{h}S_d\left(\alpha_d + 1\right) + 1\right)^2} \right], \quad (6.18)$$

where $\tilde{h} = h/\eta$ is the non-dimensional network depth (η is the slip length), and the properties S and $\mathrm{d}S/\mathrm{d}A$ are defined by equations (6.4) and (6.7), respectively.

6.1.2 Numerical verification and discussion

The numerical optimisation (see §5.2) uses non-dimensional mass flow rates calculated from a standard central-difference solution of the steady state laminar Navier-Stokes equations with a Navier slip boundary condition. As branching is symmetric, equation (5.43) is solved with $\Psi_i = 1/N$ and the volume constraint $L_p A_p = V - 2A_d L_d$. The results from the analytical and numerical optimisations for a symmetrically bifurcating rectangular channel, of fixed depth h and variable width, are presented in figure 6.2.

Agreement between the numerical optimisation and the approximate slip solution to the generalised law (equation (6.18)) is excellent for all cases, with the difference being less than 0.5% across the entire range of scales. The results also show convergence to the limits derived in equations (6.10), (6.11), (6.16) and (6.17). It can be seen that when the non-dimensional depth $\tilde{h}$ is small, such that the slip length is relatively large, Γ varies only between the plug-flow limits for high and low aspect ratios (equations (6.16) and (6.17), respectively). The high-aspect-ratio limits are the same for continuum and plug flow. When $\tilde{h}$ is large and the aspect ratio decreases, Γ first tends to the low-aspect-ratio continuum-flow limit (equation (6.11)), until the area gets sufficiently small that the variable width is comparable to the slip length, at which point the solution converges again to the low-aspect-ratio plug-flow limit (equation (6.17)).

For constant-depth networks, which are often a fabrication requirement for lab-on-a-chip devices, Γ behaves very differently compared to constant-aspect-ratio networks. For the most part, when the depth is constant, the optimal daughter-parent area ratio increases with decreasing cross-sectional area — the opposite to the trend found in Chapter 5. In addition, the range of Γ values is wider, the

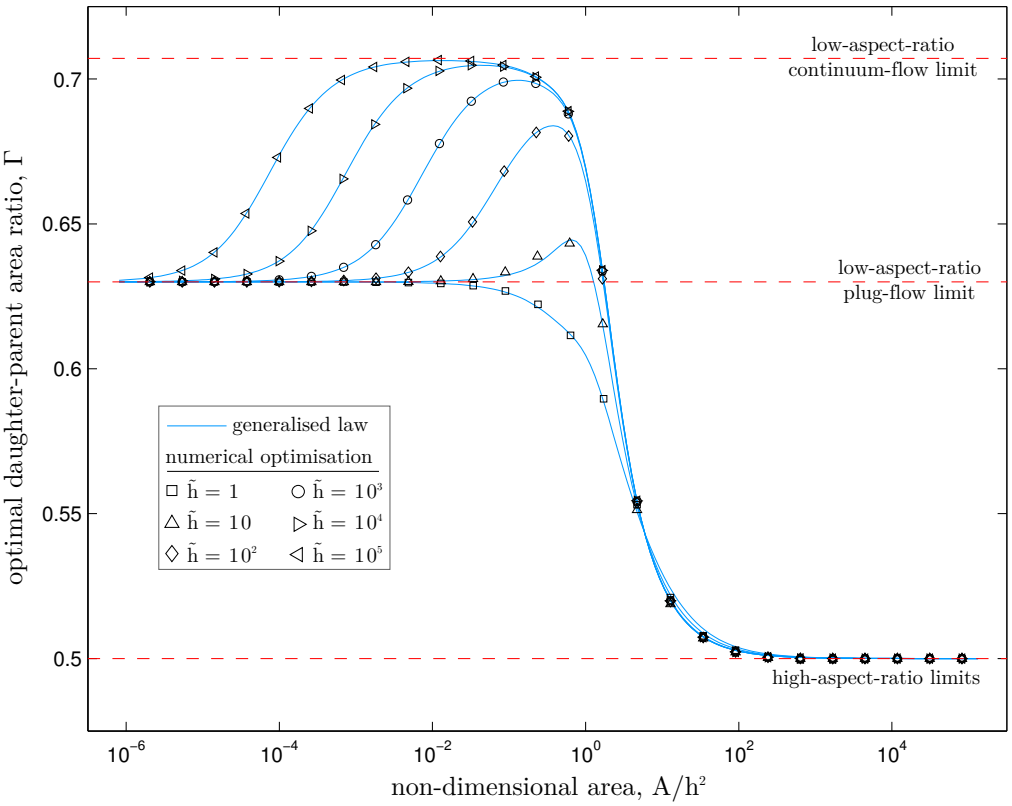

Figure 6.2: Optimal daughter-parent area ratio Γ against non-dimensional parent area A/h^2 (equal to aspect ratio α) for rectangles of a constant dimensionless depth $\tilde{h}$ in a symmetrically bifurcating network. Comparison of the approximate slip solution to the generalised law (equation (6.18)) and the numerical optimisation using data from a Navier-Stokes slip solver. Plotted for rectangles of depth $\tilde{h} = 1, 10, 10^2, 10^3, 10^4$, and 10^5.

minimum Γ is smaller, and the maximum Γ is larger for constant-depth networks: $0.5 \leq \Gamma \leq 0.71$, compared to $0.57 \leq \Gamma \leq 0.63$ for constant-aspect-ratio networks. However, there are still some similarities. At the low-aspect-ratio limits, the trend for constant-depth networks is the same as that shown in constant-aspect-ratio networks, with the optimal daughter-parent area ratio decreasing as cross-sectional area decreases.

6.2 Non-Newtonian fluid flows

"Oxygen transport is the oldest and the most advanced field of quantitative physiological inquiry" and was the initial focus of Murray's law [Murray, 1926a,b], under the assumption that a biological network would have evolved an efficient mode of

operation. In order to accurately apply the generalised law to blood flow, the non-Newtonian fluid flow properties that whole blood (plasma and cells) exhibits must be modelled. The predominant non-Newtonian fluid effect in blood (and other fluids) is the non-linear relationship between shear stress and shear strain rate, for which the power-law constitutive equation proposed by Ostwald [1925] and de-Waele [1923] is one of the most popular:

$$\tau = m \left(\frac{\mathrm{d}u}{\mathrm{d}r} \right)^n , \tag{6.19}$$

where m is the flow consistency index, $\mathrm{d}u/\mathrm{d}r$ is the shear strain rate, and n is the flow behaviour index. This relationship leads to an effective viscosity μ of

$$\mu = m \left(\frac{\mathrm{d}u}{\mathrm{d}r} \right)^{n-1} . \tag{6.20}$$

Power-law fluids can be divided into three classes based on their flow behaviour index: 1) pseudoplastic (shear thinning) fluids ($n < 1$) exhibit a decrease in viscosity with increased shear strain rate; 2) Newtonian fluids ($n = 1$) exhibit a constant viscosity; and 3) dilatant (shear thickening) fluids ($n > 1$) exhibit an increase in viscosity with increased shear strain stress. Blood is a pseudoplastic fluid, which enables it to flow efficiently through small capillaries due to the decrease in viscosity.

Although other literature exists on the subject of optimal non-Newtonian branching [Revellin et al., 2009; Tesch, 2010], their results are based on the assumption that Murray's law produces an optimal daughter-parent area ratio, which has been proven incorrect in Chapter 5. In both studies, the results showed that the optimal area ratio was independent of the flow behaviour index n for symmetric and asymmetric branching, reverting to the Newtonian Murray's law expression (equation (4.8)). The focus of this section is on blood flow, the smallest vessels of which have a radius $R \sim \mathcal{O}(\mu\mathrm{m})$. As such, the generalised law for non-Newtonian fluids will only be derived for circular cross sections at the continuum-flow limit.

6.2.1 Analytical solution

In cylindrical coordinates, the Navier-Stokes equation for laminar, steady, axisymmetric, and fully-developed flow through a circular cross section is

$$\frac{\Delta P}{L} = -\frac{1}{r} \frac{\mathrm{d}}{\mathrm{d}r} \left(\mu r \frac{\mathrm{d}u}{\mathrm{d}r} \right) , \tag{6.21}$$

where u is the streamwise velocity (the radial and swirl velocity components are assumed to be zero). Substituting equation (6.20) into equation (6.21) and integrating

with respect to r gives

$$\frac{\Delta P r}{2L} = -m\left(\frac{\mathrm{d}u}{\mathrm{d}r}\right)^n + C_1, \tag{6.22}$$

where C_1 is a constant. At the midpoint of the cross section, where $r = 0$, the velocity is at a maximum and thus $\mathrm{d}u/\mathrm{d}r = 0$; therefore $C_1 = 0$. Integrating with respect to r once more produces

$$u = -\left(\frac{\Delta P}{2Lm}\right)^{1/n}\left(\frac{n}{n+1}\right) r^{1+1/n} + C_2, \tag{6.23}$$

where C_2 is another constant. As this is at the continuum-flow limit, the no-slip boundary condition applies and the velocity is zero at the wall, i.e. $u(r = R) = 0$. Inserting this constraint into equation (6.23) produces the non-Newtonian velocity profile:

$$u = \left(\frac{\Delta P R}{2Lm}\right)^{1/n}\left(\frac{nR}{n+1}\right)\left[1 - \left(\frac{r}{R}\right)^{1+1/n}\right]. \tag{6.24}$$

By setting $n = 1$, the parabolic velocity profile of Hagen-Poiseuille flow can be reclaimed. Equation (6.24) also shows that for a shear thinning fluid like blood, the velocity profile becomes more blunt as n decreases. Note, however blunt the profile becomes, it will not be the same as a plug flow due to the no-slip boundary condition. The mass flow rate is obtained by integrating the fluid momentum over the cross-sectional area, which in cylindrical coordinates is

$$Q = \rho \int_0^R \int_0^{2\pi} ur \,\mathrm{d}r \,\mathrm{d}\theta, \tag{6.25}$$

where ρ is the mass density and θ is the azimuth. Substituting equation (6.24) into (6.25) gives

$$Q = \left(\frac{\Delta P R}{2Lm}\right)^{1/n}\left(\frac{n\rho\pi R^3}{3n+1}\right). \tag{6.26}$$

Again, it is noted that when $n = 1$, the Hagen-Poiseuille equation is recovered. Noting that $A = \pi R^2$, the flow resistance per unit length is

$$k = \left[2m\pi^{(n+1)/2}\left(\frac{3n+1}{n\rho}\right)^n Q^{n-1}\right] A^{-(3n+1)/2}. \tag{6.27}$$

For non-Newtonian fluids, there is a non-linear relationship between the pressure gradient and the mass flow rate, so k is a function of Q. It is recalled from §5.1 that Q is the mass flow rate through the parent channel, and $\Psi_i Q$ is the mass flow rate

through the i^{th} daughter channel. For all the constraint options of the optimisation described by equation (5.1), $\mathrm{d}Q/\mathrm{d}\Gamma = 0$, so evaluating equation (6.27) for parent and daughter channels and substituting the result into the asymmetric generalised law gives

$$A_p^{(3n+3)/2} = \sum_{i=1}^{N} \left(\frac{1}{\Psi_i^n} \right) A_{d_i}^{(3n+3)/2}. \tag{6.28}$$

Recalling from equation (5.20) that $\Delta P_{d_i}/(\Psi_i L_{d_i} k_{d_i}) = \text{const}$, and substituting equation (6.27) for k, the cross-sectional area relationship between the i^{th} and j^{th} daughters can be determined:

$$A_{d_i} = A_{d_j} \left[\left(\frac{\Psi_i}{\Psi_j} \right)^n \Phi_{ij} \right]^{2/(3n+1)}. \tag{6.29}$$

Substituting equation (6.29) into equation (6.28), and rearranging for the daughter-parent area ratio gives

$$\Gamma_j = \Psi_j^{2n/(3n+1)} \left[\sum_{i=1}^{N} \Phi_{ij} \left(\Psi_i^n \Phi_{ij} \right)^{2/(3n+1)} \right]^{-2/(3n+3)}. \tag{6.30}$$

Equation (6.30) relates the area of the parent channel to the area of the j^{th} daughter channel in an optimised network of circular channels transporting a non-Newtonian fluid. By setting $n = 1$, the asymmetric generalised law for Newtonian fluid flows at the continuum-flow limit (equation (5.23)) is retrieved. Equation (6.30) shows that Γ is dependent on the flow behaviour index n, contrary to results from previous studies on non-Newtonian fluidic branching based on Murray's law [Revellin et al., 2009; Tesch, 2010]. The optimal daughter-parent area ratio is only independent of n for symmetric branching, i.e. $\Psi_i = \Psi_j = 1/N$ and $\Phi_{ij} = 1$:

$$\Gamma = N^{-2/3}. \tag{6.31}$$

This is exactly the same as equation (5.24) for symmetric Newtonian branching flows and agrees with Revellin et al. [2009] and Tesch [2010] for symmetric non-Newtonian branching flows. Equation (6.30) can also be used to determine the optimal area ratio for the limits of the flow behaviour index n. For the shear-thickening-fluid limit, when $n \gg 1$, equation (6.30) reduces to

$$\Gamma_j = \Psi_j^{2/3}. \tag{6.32}$$

Interestingly, equation (6.32) is independent of daughter-daughter pressure gradient ratio Φ_{ij} and is exactly the same as the Murray's law asymmetric relation when posed in terms of areas (equation (5.44)). For the shear-thinning-fluid limit, when $n \ll 1$, equation (6.30) reduces to

$$\Gamma_j = \left[\sum_{i=1}^{N} \Phi_{ij}^3 \right]^{-2/3} . \tag{6.33}$$

At this limit, the optimal area ratio is independent of the daughter flow-rate fraction Ψ_j.

6.2.2 Numerical verification and discussion

The numerical optimisation procedure (see §5.2) uses mass flow rates calculated from equation (6.26), as it is an exact analytical expression. Evaluating equation (6.26) for parent and daughter channels, the mass flow rate through a two-level network (assuming that the pressure drops over the daughter channels are equal) is

$$Q = C_3 \left[\frac{L_p}{A_p^{(3n+1)/2}} + \frac{\Psi_i^n L_{d_i}}{A_{d_i}^{(3n+1)/2}} \right]^{-1/n} , \tag{6.34}$$

where C_3 is a constant that equals

$$C = \left(\frac{\Delta P}{2m\pi^{(n+1)/2}} \right)^{1/n} \left(\frac{n\rho}{3n+1} \right) . \tag{6.35}$$

As the flow behaviour index n is a constant within the optimisation, it is convenient to make the exponent in equation (6.34) small for the sake of numerical stability:

$$Q = C_3 \left[\frac{L_p}{A_p^{(3n+1)/2}} + \frac{\Psi_i^n L_{d_i}}{A_{d_i}^{(3n+1)/2}} \right]^{-n^b} \text{ where } b = \begin{cases} -1 \text{ for } n \geq 1 \\ 1 \text{ for } n < 1 \end{cases} \tag{6.36}$$

Equation (6.36) is solved simultaneously for each daughter i (instead of equation 5.43) with the general volume constraint of equation (5.3). If the pressure drops over the daughter channels are not equal, then the brute-force algorithm outlined in Appendix H is employed.

The first set of optimisation results are for an asymmetrically bifurcating network with equal pressure gradients applied in the daughter channels (i.e. $\Phi_{ij} = 1$), and demonstrates that the optimal daughter-parent area ratio Γ_j is dependent on the flow behaviour index n, contrary to the results of Revellin et al. [2009] and

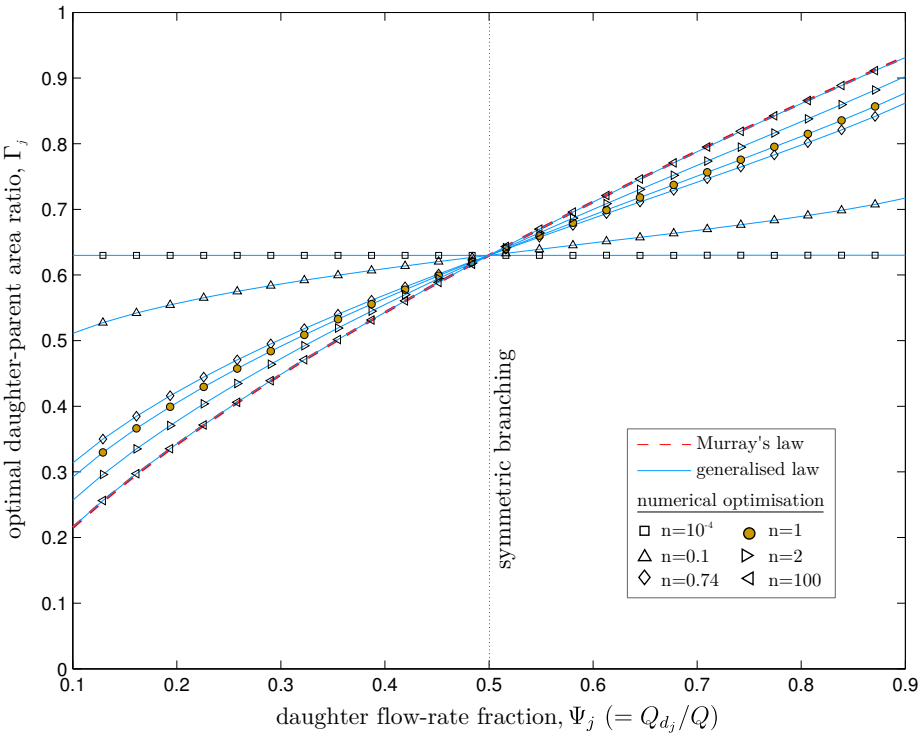

Figure 6.3: Optimal daughter-parent area ratio Γ_j against daughter flow-rate fraction Ψ_j, in a two-level bifurcating network of circular channels with equal daughter channel pressure gradients ($\Phi_{ij} = 1$). Comparison of Murray's law (equation (5.44)), the generalised law (equation (6.30)), and results from the numerical optimisation. Plotted for n =10^{-4}, 0.1, 0.74 (blood), 1 (Newtonian fluid), 2, and 100.

Tesch [2010]. Asymmetry is induced by varying the daughter flow-rate fraction Ψ_j. In Fig. 6.3, the Newtonian fluid case ($n = 1$) is highlighted with a filled marker and it is noted that this solution is the same as that shown in Fig. 5.1. It is observed that, for all n, the gradient ($\mathrm{d}\Gamma_j/\mathrm{d}\Psi_j$) increases monotonically with increasing n. When $n \gg 1$, the fluid approaches the shear-thickening-fluid limit (equation (6.32)) where Murray's law is correct for all Ψ_j. For smaller values of n, Murray's law is only correct for symmetric bifurcations ($\Psi_j = 0.5$) and becomes increasingly inaccurate as n decreases.; for a flow-rate percentage of 10% ($\Psi_j = 0.1$), Murray's law under predicts Γ_j by 66% for $n = 10^{-4}$. In contrast, the generalised law is accurate for all values of Ψ_j and n. The plot for $n = 0.74$ is an approximation of the optimal area ratio for blood flow, based on the measurements of a falling-ball viscometer [Eguchi and Karino, 2008]. When $n \ll 1$, the fluid approaches the shear-thinning-fluid limit (equation (6.33)) and Γ_j becomes independent of Ψ_j.

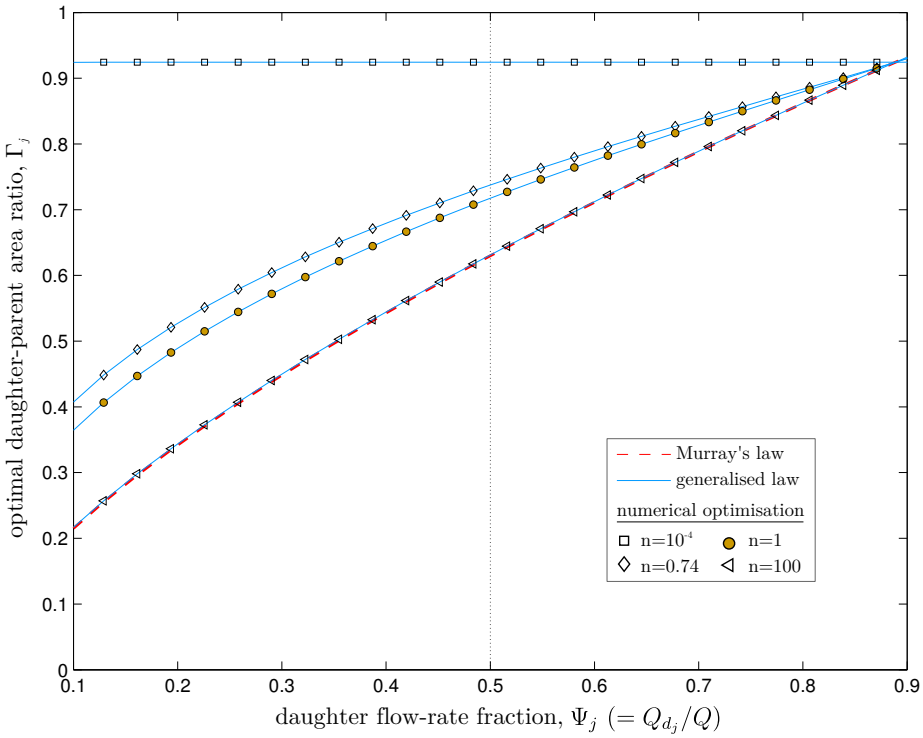

Figure 6.4: Optimal daughter-parent area ratio (Γ_j) against daughter flow-rate fraction (Ψ_j), in a two-level bifurcating network of circular channels with $\Phi_{ij} = 0.5$. Comparison of Murray's law (equation (5.44)), the generalised law (equation (6.30)), and results from the numerical optimisation. Plotted for n =10^{-4}, 0.74 (blood), 1 (Newtonian fluid), and 100.

The reason for the shear-thickening- and shear-thinning-fluid limits can be found by examining the mass flow rate of a non-Newtonian fluid. When $n \ll 1$, by raising all terms to the power of n, equation (6.26) tends towards $1 = \Delta P R/(2Lm)$ and the area ratio is only a function of the pressure gradient; hence Γ_j does not vary with Ψ_j. When the daughter-daughter pressure gradient ratio Φ_{ij} decreases, the area must increase to compensate. This is shown in Fig. 6.4, where $\Phi_{ij} = 0.5$: when $n \approx 0$, $\Gamma_j = 0.92$; compared to $\Gamma_j = 0.63$ when $\Phi_{ij} = 1$ in Fig. 6.3. Conversely, when $n \gg 1$, equation (6.26) tends towards $Q = \rho\pi R^3/3$ and the area ratio is only a function of the mass flow rate; hence Γ_j does not vary with Φ_{ij}. This expression, with $Q \propto R^3$, is equivalent to Murray's optimisation for a single channel (equation (4.6)), and thus leads to Murray's law when applied to a branching network, as shown in Figs. 6.3 and 6.4.

6.3 Turbulent flows

Turbulent fluidic networks can be found in the upper airways of the lung [Olsen et al., 1970] and, under some circumstances, in blood flow through the aorta [Stein and Sabbah, 1976], as well as in a number of civil engineering applications, including air conditioning, river and canal networks, hot water distribution, and a variety of hydraulic and pneumatic devices. Optimal branching of turbulent flows was first considered by Uylings [1977] by extending Murray's principle of minimum work, and has since been applied to symmetric branching using the minimisation of resistance [Bejan et al., 2000] and the minimisation of mass [Williams et al., 2008]. As subsonic turbulence only occurs at large physical scales (i.e. at large Reynolds numbers), only the continuum-flow limit will be considered in this section.

6.3.1 Analytical solution

Turbulent flow is described by the phenomenological Darcy-Weisbach equation which relates the pressure drop to the mean velocity in a channel of arbitrary cross-sectional shape:

$$\Delta P = \frac{f_d \rho L \bar{u}^2}{2D}, \tag{6.37}$$

where f_d is the Darcy friction factor, $\bar{u}$ is the mean streamwise velocity and $D = 4A/\mathcal{P}$ is the hydraulic diameter. Note that equation (6.37) is applicable to gravity-driven open channels, e.g. rivers, as well as closed pipes. In a river, the pressure drop is a function of the channel slope [Bejan et al., 2000] and $\mathcal{P}$ is the wetted perimeter. Making the substitutions $\mathcal{R} = \sqrt{A}/\mathcal{P}$ and $Q = \rho \bar{u} A$, equation (6.37) can be rewritten as

$$\Delta P = \frac{f L Q^2}{8 \rho \mathcal{R} A^{5/2}}, \tag{6.38}$$

and the flow resistance per unit length k is

$$k = \frac{f Q}{8 \rho \mathcal{R} A^{5/2}}. \tag{6.39}$$

As explained in the previous section, $\mathrm{d}Q/\mathrm{d}\Gamma_j = 0$ for all constraint options of the optimisation described by equation (5.1). For fully-rough-wall turbulent flow, the friction factor is also approximately constant, i.e. it is independent of the Reynolds number Re and the mass flow rate. So, substituting equation (6.39) into the asym-

metric generalised law gives

$$A_p^{7/2} = \sum_{i=1}^{N} \frac{1}{\Psi_i^2} A_{d_i}^{7/2}. \tag{6.40}$$

Combining equations (5.20) and (6.39) provides the cross-sectional area relationship between the i^{th} and j^{th} daughters:

$$A_{d_i} = A_{d_j} \left(\frac{\Psi_i^2 \Phi_{ij}}{\Psi_j^2} \right)^{2/5}. \tag{6.41}$$

Substituting equation (6.41) into equation (6.40) and rearranging for the daughter-parent area ratio gives

$$\Gamma_j = \Psi_j^{4/5} \left[\sum_{i=1}^{N} \Phi_{ij} \left(\Psi_i^2 \Phi_{ij} \right)^{2/5} \right]^{-2/7}. \tag{6.42}$$

Equation (6.42) relates the area of the parent channel to the area of the j^{th} daughter channel in an optimised two-level network for fully-rough-wall turbulent flow. It is valid for channels of any cross-sectional shape, provided the shape is constant through the network, and is only equivalent to the turbulent Murray's law [Uylings, 1977] (equation (4.9)) for symmetric branching, i.e. $\Psi_i = \Psi_j = 1/N$ and $\Phi_{ij} = 1$, where (6.42) reduces to

$$\Gamma = N^{-6/7}. \tag{6.43}$$

This also agrees with the symmetric branching turbulent flow results from Bejan et al. [2000] and Williams et al. [2008]. Comparing equation (6.43) to equation (5.24) shows that, for symmetric branching, the optimal daughter-parent area ratio is smaller for turbulent flow than it is for laminar flow.

6.3.2 Numerical verification and discussion

The numerical optimisation procedure (see §5.2) uses mass flow rates calculated from equation (6.38), as it is an exact analytical expression. Evaluating equation (6.38) for parent and daughter channels, the mass flow rate through a two-level network (assuming that the pressure drops over the daughter channels are equal) is

$$Q = \sqrt{\frac{8 \Delta P \rho \mathcal{R}}{f_d}} \left[\frac{L_p}{A_p^{5/2}} + \frac{\Psi_i^2 L_{d_i}}{A_{d_i}^{5/2}} \right]^{-1/2}. \tag{6.44}$$

Equation (6.44) is solved simultaneously for each daughter i (instead of equation 5.43) with the general volume constraint of equation (5.3). If the pressure drops over the daughter channels are not equal, then the brute-force algorithm outlined in Appendix H is employed. For the turbulent Murray's law [Uylings, 1977], the closure $R_{d_i}^{7/3} = R_{d_j}^{7/3}(1 - \Psi_j)/\Psi_j$ is provided by mass conservation, which leads to

$$\Gamma_j = \Psi_j^{6/7}. \tag{6.45}$$

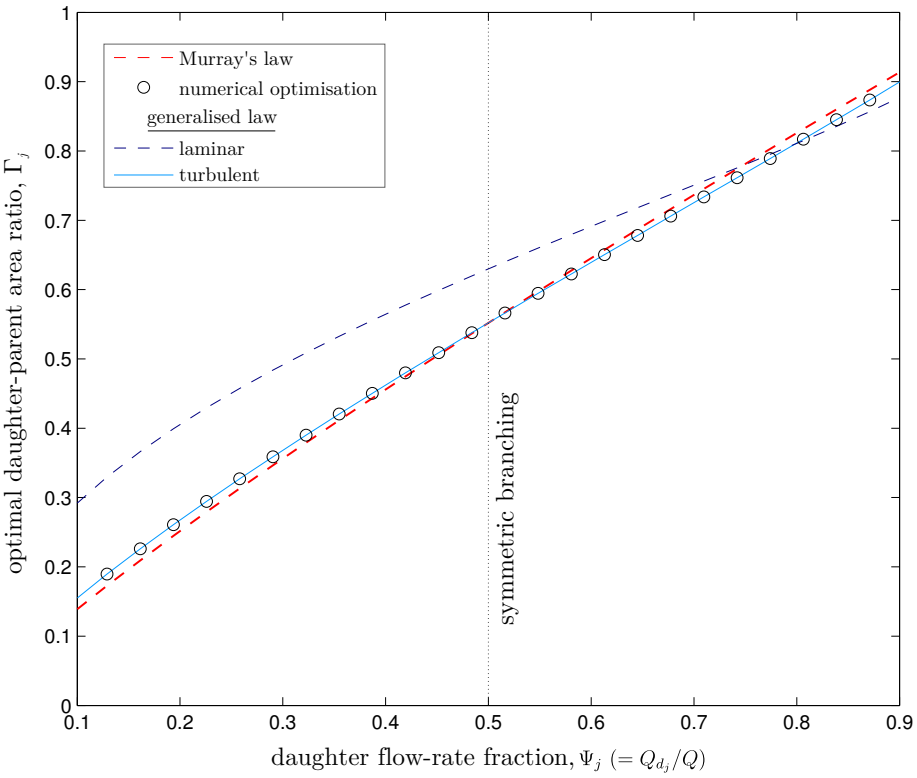

Figure 6.5: Optimal daughter-parent area ratio Γ_j against daughter flow-rate fraction Ψ_j, for fully-rough-wall turbulent flow through a two-level bifurcating network of arbitrary, but constant, cross-sectional shape and equal daughter channel pressure gradients ($\Phi_{ij} = 1$). Plotted for Murray's law (equation (6.45)), the laminar generalised law (equation (5.23)), the turbulent generalised law (equation (6.42)), and results from the numerical optimisation.

The optimisation results shown in Figs. 6.5 and 6.6 are for an asymmetrically bifurcating network with asymmetry induced by varying the daughter flow-rate fraction Ψ_j and daughter-daughter pressure gradient ration Φ_{ij}, respectively. Again, there is excellent agreement between the numerical optimisation and the turbulent

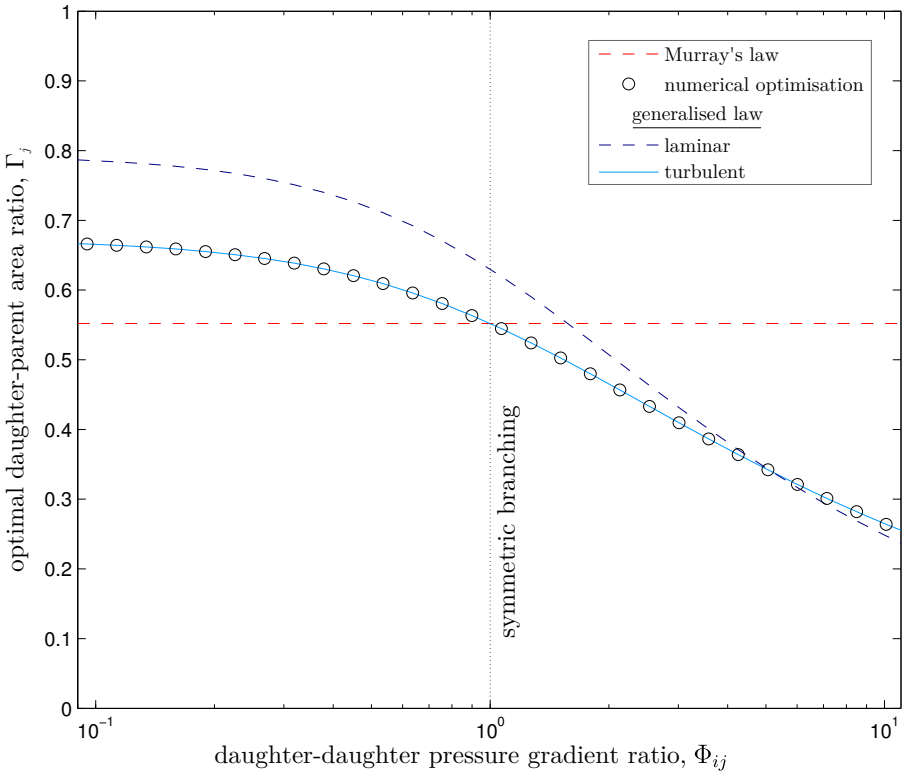

Figure 6.6: Optimal daughter-parent area ratio Γ_j against daughter-daughter pressure gradient ratio Φ_{ij}, for fully-rough-wall turbulent flow through a two-level bifurcating network of arbitrary, but constant, cross-sectional shape. The mass flow rate through each daughter channel is equal, i.e. $\Psi_j = 0.5$. Plotted for Murray's law (equation (6.45)), the laminar generalised law (equation (5.23)), the turbulent generalised law (equation (6.42)), and results from the numerical optimisation.

generalised law for all values of Ψ_j and Φ_{ij}. Compared to laminar flow, the optimal daughter-parent area ratio for the turbulent flow tends to be small. In a bifurcating channel where the flow rate through each daughter channel is equal, Γ_j is only larger for laminar flow when $\Phi_{ij} > 5.2$; when the pressure gradient over each daughter is equal, Γ_j is only larger for laminar flow when $\Psi_j > 0.8$. Murray's law proves to be a more accurate approximation for asymmetrically branching turbulent flows (compared to laminar flows), but still errs by 10% when $\Psi_j = 0.1$ (and $\Phi_{ij} = 1$), and by 19% when $\Phi_{ij} = 2$ (and $\Psi_j = 0.5$). For symmetric branching ($\Psi = 0.5$ and $\Phi_{ij} = 1$), the numerical and analytical solutions both agree with Murray's law [Uylings, 1977] and the results by Bejan et al. [2000] and Williams et al. [2008].

6.4 Optimal branching angles

The optimal branching angle in bifurcating fluidic networks has been the focus of a number of studies [Murray, 1926c; Horsfield and Cumming, 1967; Kamiya and Togawa, 1972; Uylings, 1977; Zamir, 1976a,b, 1978; Roy and Woldenberg, 1982; Roy, 1983; Gosselin and da Silva, 2007], but almost all previous literature has concerned channels with circular cross sections at the continuum-flow limit. In order to be suitable for the design of artificial networks, it is important that the optimisation for the branching angle is 1) applicable to arbitrary cross-sectional shapes, due to manufacturing restrictions often prohibiting cylindrical channels; and 2) applicable at the micro/nanoscale, due to the ever-increasing prominence of lab-on-a-chip devices.

6.4.1 Analytical solution

To determine the optimal branching angle θ, the position of the inlet to the parent channel p, and the outlets to the daughter channels d_1 and d_2, are fixed, as shown in Fig. 6.7. With inlet and outlet positions constrained, the channel lengths are now

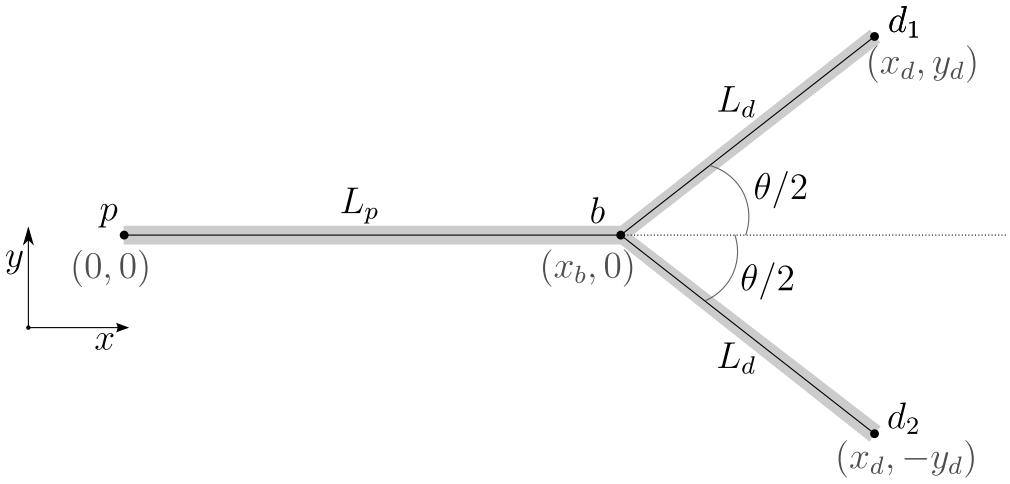

Figure 6.7: Schematic showing the symmetric bifurcation of a network, with a fixed parent inlet position at p $(0, 0)$ and fixed daughter outlet positions at d_1 (x_d, y_d) and d_2 $(x_d, -y_d)$.

a function of the position of the branching point b. For simplicity, only symmetric bifurcations are considered. By fixing the parent inlet at the origin, i.e. (0,0), the

branching point is set to lie on the x-axis. The channel lengths are then

$$L_p = x_b, \tag{6.46}$$

$$L_d = \sqrt{(x_d - x_b)^2 + y_d^2}. \tag{6.47}$$

To maximise flow conductance per unit volume through the network, a optimisation statement is required regarding the position of the branching point:

$$\underset{x_b \in [0, x_d]}{\arg\max} \left[\frac{Q}{\Delta P V} \right] \text{ subject to fixed } \begin{cases} Q, \Delta P \\ V, \Delta P \\ V, Q \end{cases} \tag{6.48}$$

Note that this optimisation can be considered separately to the optimisation for the daughter-parent area ratio Γ, as Γ is independent of the relative lengths of the parent and daughter channels and so is valid for all positions of x_b. It is recalled from §5.1 that the total volume of a symmetrically bifurcating network is

$$V = A_p L_p + 2 A_d L_d. \tag{6.49}$$

Inserting equation (6.49) into the new fitness function of equation (6.48), and noting that, for all constraint combinations, $\mathrm{d}(\Delta P)/\mathrm{d}x_b = 0$ and $\mathrm{d}Q/\mathrm{d}x_b = 0$, gives

$$\frac{\mathrm{d}}{\mathrm{d}x_b} \left(\frac{\Delta P V}{Q} \right) = \frac{\mathrm{d}A_p}{\mathrm{d}x_b} \left(L_p + 2\Gamma L_d \right) + A_p \left[1 - 2\Gamma \cos\left(\frac{\theta}{2} \right) \right] = 0, \tag{6.50}$$

where $A_d = \Gamma A_p$ and

$$\frac{x_d - x_b}{L_d} = \cos\left(\frac{\theta}{2} \right). \tag{6.51}$$

It is recalled from §5.1 that the total pressure drop over a bifurcating network can be expressed as

$$\Delta P = Q \left(L_p k_p + \frac{L_d k_d}{2} \right), \tag{6.52}$$

And, as $\mathrm{d}(\Delta P)/\mathrm{d}x_b = 0$ and $\mathrm{d}Q/\mathrm{d}x_b = 0$:

$$\frac{\mathrm{d}A_p}{\mathrm{d}x_b} \left(L_p \frac{\mathrm{d}k}{\mathrm{d}A}\bigg|_p + \frac{\Gamma L_d}{2} \frac{\mathrm{d}k}{\mathrm{d}A}\bigg|_d \right) + k_p - \frac{k_d}{2} \cos\left(\frac{\theta}{2} \right) = 0. \tag{6.53}$$

For symmetric bifurcations, the generalised law is

$$4\left.\frac{\mathrm{d}k}{\mathrm{d}A}\right|_p = \left.\frac{\mathrm{d}k}{\mathrm{d}A}\right|_d. \tag{6.54}$$

Combining equations (6.50), (6.53), and (6.54), via the chain rule, gives the optimal branching angle:

$$\cos\left(\frac{\theta}{2}\right) = \left(k_p - A_p\left.\frac{\mathrm{d}k}{\mathrm{d}A}\right|_p\right)\left(\frac{k_d}{2} - 2\Gamma A_p\left.\frac{\mathrm{d}k}{\mathrm{d}A}\right|_p\right)^{-1}, \tag{6.55}$$

which, for brevity, will be referred to as the generalised *angle* law to distinguish it from the generalised *area* law. Equation (6.55) is independent of the relative parent and daughter channel lengths and is valid for all non-trivial branching cases where $x_b > 0$ — when the network aspect ratio $\beta = x_d/y_d$ is small, the optimised solution is for the branching point to be at the inlet to the parent channel (see Appendix I for more detail). Combining equations (6.46), (6.47), and (6.51) gives an expression for the optimal daughter-parent length ratio $\Omega = L_d/L_p$ in terms of the optimal branching angle

$$\Omega = \left[\beta\sqrt{1-\cos^2\left(\frac{\theta}{2}\right)} - \cos\left(\frac{\theta}{2}\right)\right]^{-1}. \tag{6.56}$$

The extensions to the generalised law detailed in equations (6.55) and (6.56) are valid for any cross-sectional shape, for any fluid (e.g. non-Newtonian), and for any Reynolds number (e.g. for turbulent flow). However, in this thesis, the focus will be restricted to laminar flow. In the next section, some important cases are considered where A can be expressed easily as an analytical function of k.

The continuum-flow limit

It is recalled from §5.1.1 that, at the continuum-flow limit, the flow resistance per unit length k is

$$k = \frac{\mu}{\rho S A^2}, \tag{6.57}$$

and the optimal daughter-parent area ratio Γ for a symmetrically bifurcating network is

$$\Gamma = 2^{-2/3}. \tag{6.58}$$

Inserting equations (6.57) and (6.58) into the generalised angle law (equation (6.55)) gives

$$\cos\left(\frac{\theta}{2}\right) = 2^{-1/3}, \tag{6.59}$$

or $\theta \approx 74.93°$. This is exactly equivalent to the result found by Murray's law in equation (4.16). Substituting equation (6.59) into equation (6.56) gives the optimal daughter-parent length ratio for the continuum-flow limit:

$$\Omega = \frac{2^{1/3}}{\left(\beta\sqrt{2^{2/3}-1}-1\right)}. \tag{6.60}$$

The plug-flow limit

At the plug-flow limit, it is recalled from §5.1.2 that the flow resistance per unit length k is

$$k = \frac{\mu}{\rho\eta\mathcal{R}A^{3/2}}, \tag{6.61}$$

and the optimal daughter-parent area ratio Γ for a symmetrically bifurcating network is

$$\Gamma = N^{-4/5}. \tag{6.62}$$

Inserting equations (6.61) and (6.62) into the generalised angle law gives

$$\cos\left(\frac{\theta}{2}\right) = 2^{-1/5}, \tag{6.63}$$

or $\theta \approx 58.95°$. Substituting equation (6.63) into equation (6.56) gives the optimal daughter-parent length ratio for the plug-flow limit:

$$\Omega = \frac{2^{1/5}}{\left(\beta\sqrt{2^{2/5}-1}-1\right)}. \tag{6.64}$$

A slip-flow approximation

Between the continuum- and plug-flow limit, it is recalled from §5.1.3 that the flow resistance per unit length k can be expressed as

$$k = \frac{\mu\mathcal{P}}{\rho A^2\left(S\mathcal{P}+\eta\right)}. \tag{6.65}$$

Inserting equation (6.65) into the generalised angle law produces the general slip solution for the optimal branching angle in networks with any cross-sectional shape

(as long as the shape remains constant through the network), across all length-scales:

$$\cos\left(\frac{\theta}{2}\right)\left[P_d\left(\frac{S\mathcal{P}_p+\eta}{S\mathcal{P}_d+\eta}\right)+4\Gamma^3\left(2\mathcal{P}_p-\left(\frac{\eta A_p}{S\mathcal{P}_p+\eta}\right)\left.\frac{\mathrm{d}\mathcal{P}}{\mathrm{d}A}\right|_p\right)\right] = 2\Gamma^2\left[3\mathcal{P}_p-\left(\frac{\eta A_p}{S\mathcal{P}_p+\eta}\right)\left.\frac{\mathrm{d}\mathcal{P}_p}{\mathrm{d}A}\right|_p\right], \quad (6.66)$$

where it is recalled that $\mathcal{P}$ is the cross-section perimeter and Γ can be found by solving equation (5.36). The optimal daughter-parent length ratio Ω can then be found with equation (6.56).

Circular cross section For a circular cross section, $A=\pi R^2$, $S=1/8\pi$, $\mathcal{P}=2\sqrt{\pi A}$, and $\mathrm{d}\mathcal{P}/\mathrm{d}A=\sqrt{\pi/A}$. Substituting these values into equation (6.66) and simplifying gives

$$\cos\left(\frac{\theta}{2}\right)=2\Gamma^{3/2}\left(3\tilde{R}_p+10\right)\left[\frac{\left(\tilde{R}_p+4\right)^2}{\left(\tilde{R}_p\sqrt{\Gamma}+4\right)}+8\Gamma^{5/2}\left(\tilde{R}_p+3\right)\right]^{-1}, \quad (6.67)$$

where $\tilde{R}_p=R_p/\eta$ is the dimensionless radius of the parent channel.

Rectangular cross section For a rectangular channels of variable depth h and constant cross-section aspect ratio $\alpha=A/h^2$, $\mathcal{P}=2(\alpha+1)h$, $\mathrm{d}\mathcal{P}/\mathrm{d}A=(\alpha+1)h/A$, and an accurate approximation of S is given in equation (6.4). Substituting these values into equation (6.66) and simplifying gives

$$\cos\left(\frac{\theta}{2}\right)=\Gamma^{3/2}\left(6C\tilde{h}_p+5\right)\left[\frac{\left(C\tilde{h}_p+1\right)^2}{\left(C\tilde{h}_p\sqrt{\Gamma}+1\right)}+2\Gamma^{5/2}\left(4C\tilde{h}_p+3\right)\right]^{-1}, \quad (6.68)$$

where $\tilde{h}_p=h_p/\eta$ is the dimensionless depth of the parent channel and $C=2S(\alpha+1)$ is a constant.

6.4.2 Numerical verification and discussion

The numerical optimisation (see §5.2) uses mass flow rates calculated from a standard central-difference solution of the laminar Navier-Stokes equations with a Navier slip boundary condition. Unlike the procedure in §5.2, the channel lengths are not fixed as they depend on the branching point x_b. Instead, the parent channel inlet

(x_p, y_p) and the daughter channel outlets (x_d, y_d) are fixed and equation (5.43) is solved with $\Psi_i = 1/N$, the volume expression of equation (6.49), and the length expressions of equations (6.46) and (6.47).

The analytical and numerical solutions for the optimal branching angle θ are presented in Fig. 6.8 for a bifurcating network of channels with a variety of cross-sectional shapes, across the entire range of length scales. The results mirror

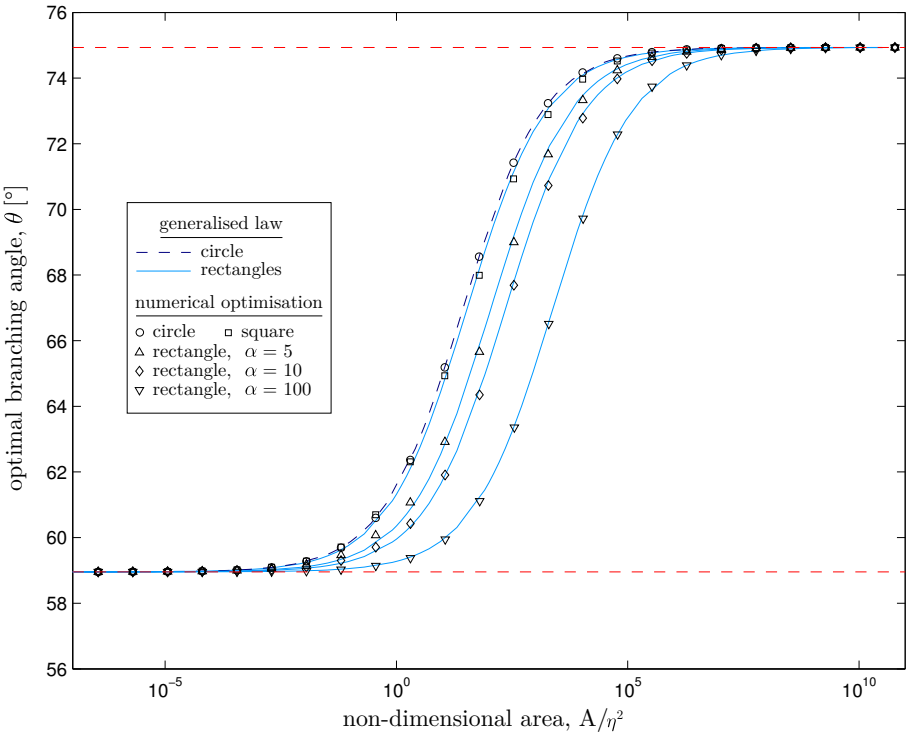

Figure 6.8: Optimal branching angle θ against non-dimensional parent area for a symmetrically bifurcating network of channels with a constant cross-sectional shape. Comparison of the approximate slip solution to the generalised angle law (equations (6.67) and (6.68)) and numerical optimisation using data from a Navier-Stokes slip solver. Plotted for circles, squares, and rectangles of cross-section aspect ratio $\alpha = 5$, $\alpha = 10$, and $\alpha = 100$.

those presented in Fig. 5.3 for the optimal daughter-parent area ratio. When the parent area is large, relative to the square of the slip length η, the optimal branching angle θ converges to the continuum-flow limit of the generalised angle law (equation (6.59)) for all shapes considered, and agrees with Murray's law (equation (4.16)). At the other extreme of scale, the optimal branching angle for all shapes converges to the plug-flow limit of the generalised angle law (equation (6.63)) for small parent

areas. In the transition between these limits, the approximate slip solution to the generalised angle law is also highly accurate across the entire range of scales for all shapes tested, and demonstrates that networks of channels with higher cross-section aspect ratios depart from the continuum-flow limit and approach the plug-flow limit at larger parent areas, owing to a lower characteristic length. Figures 5.3 and 6.8 combined verify that as the length scale reduces, the daughter-parent area ratio *and* branching angle must also reduce for the network to be globally optimised.

The results shown in Fig. 6.8 are valid for all daughter-parent length ratios Ω, provided that the optimal parent length $L_p > 0$ (the criteria for which are detailed in Appendix I). The analytical and numerical solutions for the optimal values of Ω for channels of circular cross section are presented in Fig. 6.9. The results converge

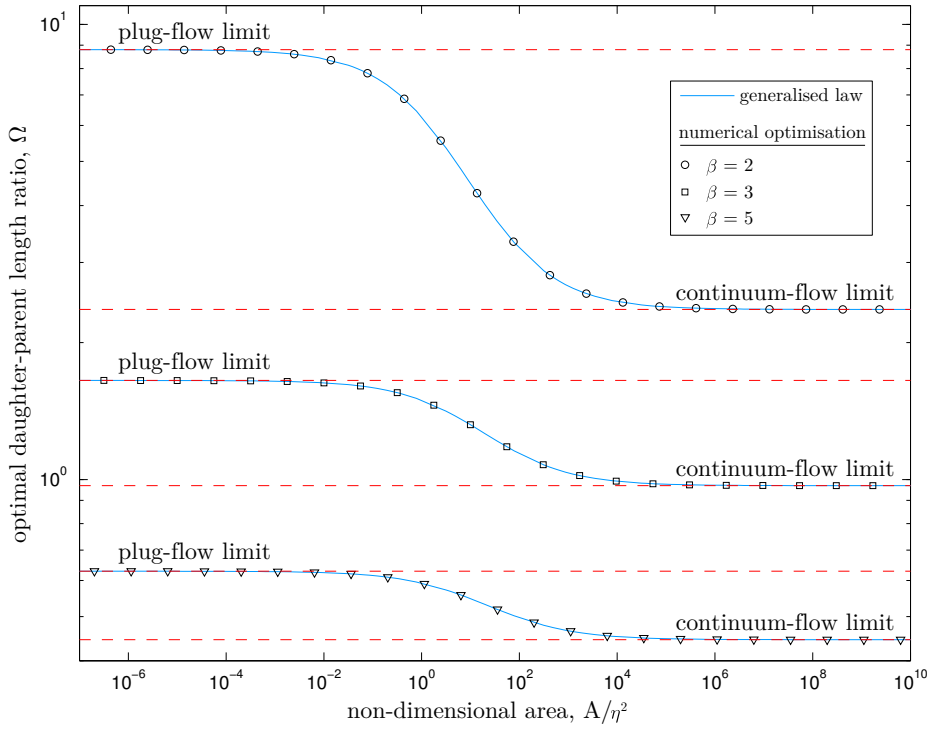

Figure 6.9: Optimal daughter-parent length-ratio Ω against non-dimensional parent area for a symmetrically bifurcating network of circular channels. Comparison of the approximate slip solution to the generalised law (equation (6.56)) and numerical optimisation using data from a Navier-Stokes slip solver. Plotted for network aspect ratios of $\beta = 2$, $\beta = 3$ and $\beta = 5$.

to the continuum-flow limit (equation (6.60)) and plug-flow limit (equation (6.64)) for large and small areas, respectively, and the slip solution to the generalised law

is accurate across the entire range of scales. While it has often been suggested [Horsfield et al., 1976; Horsfield, 1980; Emerson et al., 2006] that the channel length should be proportional to its radius (i.e. $\Omega = \sqrt{\Gamma}$), Fig. 6.9 shows that it is highly dependent on both the size of the parent cross-sectional area and the aspect ratio of the network β. In fact, contrary to the variation of Γ, Ω increases as the length-scale decreases (for all values of β that produce a non-trivial solution). In addition, Ω increases as β decreases. The corollary is that, when β becomes sufficiently small (see Appendix I for how small), the optimal solution is for the branching point to be at the inlet of the parent channel, in which case $\Omega = \infty$.

6.5 Summary

In this chapter, the generalised law has been applied to more complicated fluidic networks to determine the optimal daughter-parent area ratio Γ for some important technological and biological applications. The analytical solutions to the generalised law all show excellent agreement with the results from numerical optimisation, and further highlight the deficiencies of Murray's law when applied to branching networks.

Rectangular networks with a constant depth, often required for lab-on-a-chip devices, exhibit a change in cross-sectional shape between the parent and daughter channels. It has been shown that this leads to high- and low-aspect-ratio limits for Γ at each of the length-scale limits, which Murray's law is unable to predict. In addition, contrary to networks with a constant shape, Γ tends to decrease as area increases.

For networks transporting non-Newtonian fluids, e.g. blood, Γ has been shown to be dependent on the flow behaviour index n for asymmetric branching, contrary to what previous studies based on Murray's law [Revellin et al., 2009; Tesch, 2010] have stated. Aside from symmetric branching, Murray's law is only retrieved at the shear-thickening-limit, when $n \gg 1$ and Γ is no longer dependent on the relative pressure gradients in the daughter channels. At the shear-thinning-limit, when $n \ll 1$, Γ becomes independent of the relative mass flow rate through each daughter channel.

For turbulent fluidic networks, e.g. in many hydraulic and pneumatic devices, Γ tends to be smaller than it is for laminar flows, except in the case of large asymmetry. Murray's law for turbulent flows [Uylings, 1977] is only recovered for symmetric branching, in which case $\Gamma = N^{-6/7}$.

In addition, the generalised law has been extended to consider the optimal

branching angle. For symmetric bifurcation, it has been shown that the optimal branching angle θ varies between 74.93°and 58.95°at the continuum- and plug-flow limits, respectively, with the former limit agreeing with Murray's law. In addition, the daughter-parent length ratio has been shown to be a inversely related to the magnitude of both the parent cross-sectional area and the network aspect ratio, contrary to what previous studies have suggested.

Chapter 7

Conclusions

This thesis has presented new techniques for the simulation and design of nanofluidic branching networks, where non-continuum/non-equilibrium effects render traditional approaches invalid. A new hybrid method — the general networks internal-flow multiscale method (GeN-IMM) — enables the physical behaviour of the fluid to be precisely captured in a computationally tractable time period, while a new optimisation principle — the generalised law — provides analytical solutions for the most efficient geometrical arrangement. Although separate, the two techniques share a unified purpose to enhance the scope of nanofluidic network modelling, which is becoming increasingly important due to the high performance and functionality of lab-on-a-chip devices.

The GeN-IMM enables the accurate solution of compressible fluid flows within general, high-aspect-ratio nanoscale geometries. Networks are decomposed into smaller components, which can be simulated independently using a micro solver to capture the molecular phenomena — this thesis uses molecular dynamics (MD). Components are linked through an iterative refinement procedure which ensures the conservation of mass and the continuity of pressure throughout the network. Coupling occurs through the exchange of mass flow rate and pressure information (in the micro-macro direction), and through the application of external body force and density controls (in the macro-micro direction). By allowing channel heights and lengths, and inlet and outlet pressures, to be outputs of the iterative procedure instead of fixed values, the GeN-IMM can also be used as a design tool, removing the need for a costly trial-and-error process. To facilitate this, a wide variety of generalised constraints can be applied, including those on mass flow rate and shear stress, which are critical properties to control in drug delivery and cell response applications, respectively.

The GeN-IMM was tested for a variety of flow cases and constraint combinations in two networks: 1) a straight channel connecting two reservoirs, and 2) a bifurcating channel. These networks had to be fairly small and simplistic so that a full MD simulation could be performed for verification purposes. For all test cases, the GeN-IMM solution converged after 3 iterations, providing computational speed-ups of approximately 4 and 2 times (relative to a full MD simulation) for the straight channel and bifurcating channel cases, respectively. At convergence, the straight channel cases all exhibited relative errors of $< 1\%$ for all output variables, while the more complicated bifurcating channel cases displayed errors of up to 4% for all output variables, but mostly $< 2\%$.

A major advantage of the GeN-IMM is that non-continuum/non-equilibrium effects, such as velocity slip and molecular layering, can be accurately captured as they are inherently modelled in the MD simulations; a conventional Navier-Stokes solution could not predict these effects. The new hybrid method also has some clear advantages over full molecular simulations: 1) it is more efficient than a full MD simulation, for no discernible loss in accuracy, and the computational speed-up will be even greater for larger networks (as scale separation is increased); 2) it is less dependent on high-performance computing resources, as the relatively inexpensive simulations can be run independently on a small cluster of central/graphics processing units (either simultaneously or sequentially, if resources are limited); and 3) it can be used as a design tool for a wide variety of user-input constraints.

The generalised law is an optimisation principle based on the maximisation of flow conductance per unit volume, which will produce analytical expressions for the optimum daughter-parent area ratio Γ for any shape, at any length scale, for any flow model, and for any number of daughter branches.

Analytical solutions have been verified against a numerical optimisation and shown that, for the symmetric branching of cylindrical channels at the continuum-flow limit, the generalised law is equivalent to Murray's law [Murray, 1926a], where $\Gamma = N^{-2/3}$. However, when the network branches asymmetrically, i.e. the flow rate is not evenly divided between daughter channels (or the pressure gradients in the daughter channels are not equal), it has been shown that Murray's law is sub-optimal. This is because Murray's law presumes that the independent optimisation of each individual channel is the same as the global optimum for the entire network, which is not the case for asymmetric branching. This continuum-flow limit was found to be true for all cross-sectional shapes, assuming the shape remained constant through the network.

For symmetric branching, the generalised law is also shown to be optimal

at smaller length-scales (seen in lab-on-a-chip systems), where the flow becomes dominated by velocity slip at the wall, and the optimal daughter-parent area ratio converges to $\Gamma = N^{-4/5}$. Furthermore, the generalised law has been verified for networks of rectangular channels with a constant depth (i.e. the cross-sectional shape changes at the branching point), which is often a requirement for artificial nanoscale devices, owing to fabrication limitations. When the depth is constant, it has been shown that there are high- and low-aspect-ratio limits for Γ at each of the length-scale limits: $\Gamma = N^{-1}$ and $\Gamma = N^{-1/2}$ are the high- and low-aspect-ratio continuum-flow limits, respectively; and $\Gamma = N^{-1}$ and $\Gamma = N^{-2/3}$ are the high- and low-aspect-ratio plug-flow limits, respectively.

In addition, for symmetric bifurcation, the generalised angle law has been developed and shown that the optimal branching angle θ varies from 74.93° at the continuum-flow limit to 58.95° at plug-flow limit, with the former limit agreeing with Murray's law [Murray, 1926c]. In addition, the daughter-parent length ratio has been shown to be inversely related to the magnitude of both the parent cross-sectional area and the network aspect ratio. This is contrary to the suggestions made in previous studies [Horsfield et al., 1976; Horsfield, 1980; Emerson et al., 2006] that the length of each channel should be proportional to its radius. These developments make the generalised law ideally suited for use as a biomimetic design tool for a variety of micro and nanofluidic networks.

To further investigate the shortcomings of Murray's law, the generalised law has also been applied to different fluidic models at the continuum-flow limit: non-Newtonian fluid flows and turbulent flows. Using the power law model, Γ has been shown to be dependent on the flow behaviour index n for asymmetric branching in non-Newtonian fluidic networks, contrary to the results of previous studies based on Murray's law [Revellin et al., 2009; Tesch, 2010]. Aside from symmetric branching, Murray's law is shown to only be retrieved at the shear-thickening-limit ($n \to \infty$), where Γ becomes independent of relative pressure gradients in the daughter channels. At the shear-thinning-limit ($n \to 0$), Γ becomes independent of the relative mass flow rate through each daughter channel. In turbulent fluidic networks, Γ tends to be smaller than it is for laminar flows, except in the case of large asymmetry. Like its laminar counterpart, the turbulent Murray's law [Uylings, 1977] is only optimal for symmetric branching, in which case $\Gamma = N^{-6/7}$.

7.1 Future Work

Based on the work in this thesis, there are a number of potential expansions to the GeN-IMM and generalised law. The most prominent example would be combining the two techniques to create a single method which can accurately resolve the fluid behaviour in a geometrically optimised branching channel. This would involve the inclusion of the optimal daughter-parent area ratio Γ as a non-linear generalised constraint, which would be iteratively updated based on the measured mass flow rates and pressure drops through the daughter channels. There are also some interesting possible future studies for the GeN-IMM and generalised law individually:

GeN-IMM

- Use of the GeN-IMM in conjunction with other micro solvers, such as the direct simulation Monte Carlo method. This will enable the simulation and design of a wide range of rarefied gas applications, including micro heat exchangers for cooling integrated circuits, micro-jet actuators for flow control in aerospace, and hand-held gas chromotography systems. It will also enable non-periodic boundary conditions to be employed, which will increase the computational speed-up of the hybrid method.

- Extension of the method to accommodate multispecies flows to enable the simulation of passive nanoscale mixers for a variety of lab-on-a-chip applications. This would require modelling the concentration gradient of each species in the channel components and approximating the mean density of a component as a weighted sum of the density of each species.

- Application of the method to more realistic substrates (e.g. metals, metal oxides, and ceramics) and fluids (e.g. non-monatomic fluids). For example, it could be applied to the flow of salt water through complex networks of carbon nanotubes to test desalination efficiency.

- Extension of the method to accommodate networks of channels with varying height (e.g. converging-diverging channels); quasi-steady problems with large time-scale separation; non-isothermal flow problems, e.g. Knudsen pumps; and to electro-osmotic flows (as opposed to pressure-driven flows), which are often used for medical implants, drug deliver, or chemical separations.

- Extension of the method to incorporate machine learning approaches (e.g. neural networks or Gaussian processes) to accurately predict the output of

MD simulations (e.g. mass flow rate) based on the similarity of the input parameters (e.g. channel height, density, body force, etc.) to those in a pre-existing database. The input/output database, which will inexorably grow as new MD configurations are simulated, would drastically reduce the computational expense of all similar network cases as a molecular simulation would rarely need to be invoked.

- Investigation into the variation of convergence speed with the accuracy of the initial flow-conductance coefficient estimates ($K_{ij,q}$ and $D_{ij,q}$), and whether the linear pressure variation approximation remains accurate for longer channels.

Generalised law

- Application of the generalised law to different cross-sectional shapes such as 1) trapezoids with an angle of 54.74°, which are often used in lab-on-a-chip devices (by wet etching a $< 100 >$ silicon surface); and 2) ellipses of various aspect ratio, which more accurately describe some biological vessels, e.g. parts of the venous vasculature.

- Extension of the generalised law for non-Newtonian fluids to consider small-scale effects, including slip flows and plug flows. This would also include consideration of the Fahræus-Lindqvist effect [Fahræus and Lindqvist, 1931] which states that when the vessel radius drops below ~ 300 μm, the viscosity of blood decreases with a further decrease in vessel radius as a result of a decrease in the average concentration of red blood cells.

- Application of the generalised law to pulsatile flow, which is found in the cardiovascular and respiratory systems of animals, and in many artificial hydraulic systems. This would require consideration of the Womersley number which gives measure to the magnitude and frequency of pulsations.

- Extension of the generalised law to consider the optimal branching angles and daughter-parent length ratios for asymmetric branching. This could be compared to the optimal branching angle found by Murray's law for minimum work [Murray, 1926c], and other laws based on minimum drag force [Zamir, 1976a] and minimum volume Kamiya and Togawa [1972].

- Extension of the generalised law to consider the optimal branching angles and optimal daughter-parent area and length ratios in multi-level networks by fixing multiple outlets and solving for multiple branching points. These networks could be compared to similar biological networks for validation.

Appendix A

Argon phase diagram

In this thesis, isothermal fluid simulations of dense argon are maintained at a constant temperature of 292.8 K, which places argon in the supercritical phase [Lemmon et al., 2015] — see Fig. A.1. This temperature is chosen to ensure that the fluid remains in the same phase for the entire simulation. Large pressure drops are required in the simulations in order to obtain high signal-to-noise ratios for mass flow rate measurements; if the temperature is reduced to the liquid phase there is only a small window of operability, i.e. there is high chance that the fluid either crosses into the gaseous phase at low pressures or into the solid phase at high pressures.

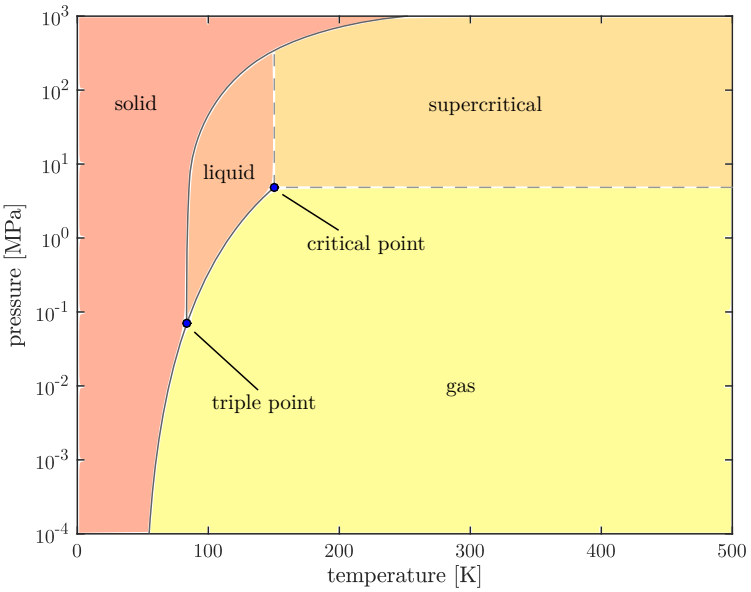

Figure A.1: The phase diagram for argon, showing the solid, liquid, gas, and supercritical regions, as well as the triple and critical points.

Appendix B

Channel micro-element length

In this thesis, all channel micro-elements have a length of $L' = 12\sigma$ (4.08 nm), where $\sigma = 0.34$ nm is the intermolecular separation between two particles that yields a potential of zero. To demonstrate that this length is sufficiently large to not induce finite-size effects, Fig. B.1 plots the measured mean mass flow rate through channel micro-elements of different length. For clarity, mass flow rates are normalised with respect to the flow through the largest channel ($L' = 24\sigma$) and channel lengths are normalised with respect to σ. In each simulation, the channel height was 3.4 nm (10σ) and the channel depth was 6.8 nm (20σ) - the same dimensions used for the straight channel network cases. All the simulations were maintained at a constant temperature of 292.8 K and brought to a constant density of 1064 kg/m^3, after which a body force of 0.122 pN was applied to all the molecules in the domain to drive the flow - this represents the same pressure gradient regardless of micro-element length. In all simulations, the micro-element lengths are multiples of the wall molecule spacing used in the full MD simulations (0.6σ), to ensure that the wall-fluid interaction is consistent.

Figure B.1 suggest that the length of channel micro-elements should be at least 9σ to avoid finite-size effects altering the physics of the flow, and thus using a length of 12σ for the simulations in this thesis is sufficient. In fact, using a channel micro-element length of 12σ is actually optimal. This is because in addition to being a multiple of 0.6σ, the micro-element length should also be multiple of the cut-off radius (4σ) for maximum computational efficiency, to ensure that only molecules in the nearest neighbour cells are considered for the calculation of the interatomic potential (the most expensive step for MD). So, the optimal channel micro-element length is the lowest common multiple of 0.6σ and 4σ (and must be $\geq 9\sigma$) — 12σ.

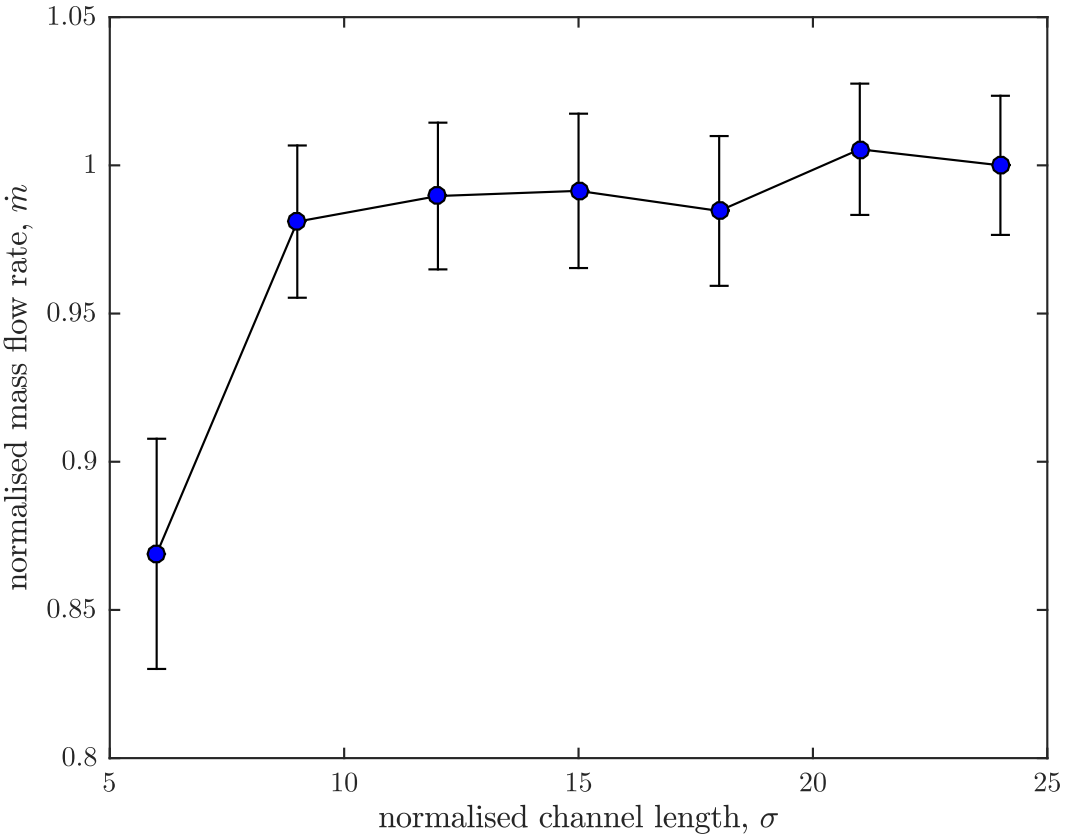

Figure B.1: Normalised mass flow rate against normalised channel micro-element length. Error bars are 1.96 standard errors of the mean to represent the 95% confidence level and account for autocorrelation within micro-elements.

Appendix C

Estimation of flow-conductance coefficients $K_{ij,q}$

Initial estimates of the flow-conductance coefficients, $K_{ij,q}$ (=$K_{ji,q}$) and $D_{ij,q}$ (=$D_{ji,q}$), can be made from past experience of the component geometry type, or from a presimulation using using either a continuum or molecular model. During the GeN-IMM algorithm, these estimates are updated using data from previous iterations. Presimulation estimates and updates to these estimates from iteration data are performed in the same way: by solving a set of simultaneous equations for each component q, using pressure and mass flow rate data at boundaries i and j measured from simulations:

$$\langle \dot{m}_i \rangle = \sum_{j=1(\neq i)}^{W_q} \langle P_i - P_j \rangle K_{ij,q}, \tag{C.1}$$

and

$$\langle \dot{m}_i \rangle = - \sum_{j=1(\neq i)}^{W_q} \langle (P_i - \Phi_i) - (P_j - \Phi_j) \rangle D_{ij,q}, \tag{C.2}$$

where $\dot{m}$ is the mass flow rate, P is the pressure, Φ is the body-force-generated pressure jump (in the artificial region), and W_q is the number of boundaries in component q. With W_q boundaries, component q has $W_q(W_q - 1)/2$ independent flow-conductance coefficients $K_{ij,q}$ (and similarly $W_q(W_q - 1)/2$ independent values of $D_{ij,q}$) and each simulation provides $W_q - 1$ unique equations. This means $\lceil W_q/2 \rceil$ simulations are required to adequately define all flow-conductance coefficients. Taking a serial network as an example then ($W_q = 2$), each component has one independent value of $K_{ij,q}$ (and one of $D_{ij,q}$ if it is a junction component) and requires data from one simulation to define them.

In this thesis, a mixture of preliminary simulations and estimations from experience were used for initial approximations, then data from the latest iteration was used to continuously refine the predictions of $K_{ij,q}$ and $D_{ij,q}$.

In Chapter 3, the correction factors λ_q and $\Omega_{ij,q}$ are updated by combining equation (C.1) with equations (3.14) and (3.15) for channel and junction components, respectively. In the artificial region, the correction factors $\Psi_{ij,q}$ are updated by combining equation (C.2) and (3.16).

Appendix D

Equation of state coefficients

For all cases in this thesis, the coefficients $a_{b,q}$ are the same for each component and are determined by fitting a least-squares polynomial through presimulation data of a periodic cube of fluid argon molecules. In this presimulation, an empty cube with side lengths of 10.88 nm is filled with a large number of argon molecules. There is no external forcing and periodic boundary conditions applied in all directions. As there are no channel walls, the molecular layering effect does not occur in this presimulation. However, as the equation of state (equation (2.6)) is iterative, this slight incongruence between the conditions in the presimulation and the micro-element simulations will not effect the final converged solution of the GeN-IMM.

The temperature is maintained at 292.8 K, while the mean pressure over the total volume of the cube is measured as molecules are systematically deleted, producing a relationship between mass density and pressure. For the temperature and pressure range considered, the fluid argon is in the supercritical phase (see Fig. A.1). A β-order polynomial is then fitted to the data, which provides the coefficients. Table D.1 and Fig. D.1 show the values of $a_{b,q}$ for fluid argon (using $\beta = 2$) and the pressure-density relationship, respectively. Data from the National institute of Standards and Technology (NIST) is also plotted [Lemmon et al., 2015] for validation purposes.

Table D.1: Equation of state coefficients $a_{b,q}$.

b	$a_{b,q}$
2	-2.9569×10^{-13}
1	2.5750×10^{-5}
0	-66.6108

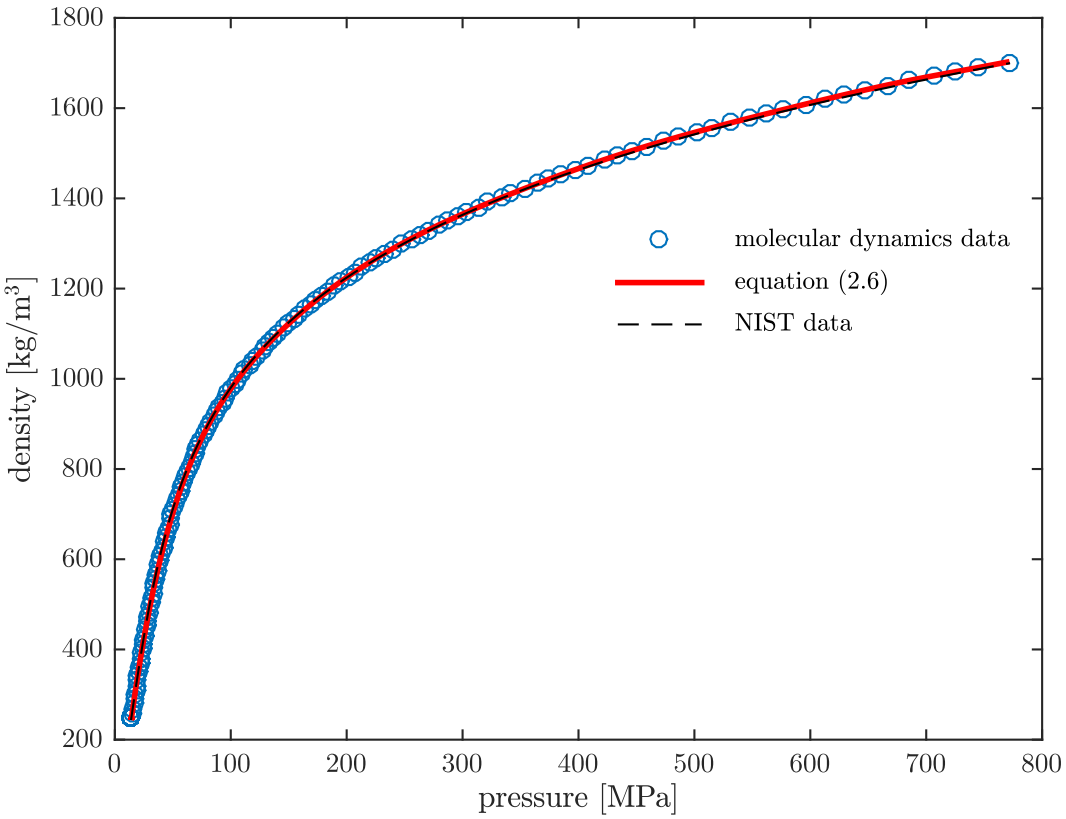

Figure D.1: Mass density against pressure for dense fluid argon at a temperature of 292.8 K. Shown for the periodic cube molecular dynamics simulation data, the equation of state (2.6) (with the terms in angled brackets equal to zero), and the NIST data.

Appendix E

Generating pressure jumps in junction micro-elements

The most convenient and common way of emulating a pressure gradient in serial molecular dynamics (MD) simulations is to apply a uniform body force to all fluid molecules in the channel [Koplik et al., 1988; Travis et al., 1997; Travis and Gubbins, 2000; Fan et al., 2002; Docherty et al., 2013], accompanied by periodicity in the flow direction. However, when the geometry is non-uniform in its cross section, as is the case for junction micro-elements (and the full MD simulations of the networks), the pressure gradient becomes a varying field. As such, the flow generated by a uniform body forcing will no longer be hydrodynamically equivalent to that created by an imposed pressure difference over the same geometry.

This problem is overcome by applying a step body force in localised regions of uniform cross section [Zhu et al., 2002, 2004]. This is used in the GeN-IMM by applying uniform body forces only in an artificial region, in order to impose the correct pressure differences over the real region. This method also retains the simplicity of using periodic boundary conditions (PBCs) in all directions for all of the MD simulations in this thesis. The main drawback of the method is that a complicated component geometry requires a similarly complicated artificial region in the micro-element to ensure the geometrical match necessary for PBCs to function (see Fig. 2.4). This makes the micro-element larger than it would otherwise be, and can have a detrimental effect on overall computational efficiency.

The magnitude of the localised step body force $F_{i,q}$ applied at the i^{th} boundary of the q^{th} component is chosen such that it creates a momentum flux (a pressure jump $\Phi_{i,q}$) within that region that is equal and opposite to that of the pressure dif-

ference ΔP we wish to induce over the real region, i.e.

$$-\Delta P = \Phi_{i,q} = F_{i,q}\rho_n \Delta x, \tag{E.1}$$

where Δx is the extent of the localised region and ρ_n is the number density in this region. Equation (E.1) can be rearranged in terms of the desired uniform forcing magnitude:

$$F_{i,q} = \frac{\Phi_{i,q}}{\rho_n \Delta x}. \tag{E.2}$$

Appendix F

Laminar macroscopic theory for entrance/exit lengths

Laminar macroscopic theory suggests that, for circular tubes, the entrance/exit length L_e is

$$L_e/D = 0.06R_e, \tag{F.1}$$

where D is the tube diameter, and $R_e = \rho\bar{U}D/\mu$ is the Reynolds number, where ρ is the mass density, $\bar{U}$ is the mean velocity, and μ is the dynamic viscosity. For non-circular channels, a reasonable approximation is to substitute the hydraulic diameter $D_h = 4A/P$ for D, where A is the cross-sectional area and P is the wetted perimeter. The cases in this thesis have a cross section with a height h and an infinite width, so $D_h = 2h$. Substituting this into equation (F.1) gives

$$L_e = \frac{0.24\bar{\rho}\bar{U}h^2}{\mu}. \tag{F.2}$$

Out of all of the micro-elements used in any of the network cases in this thesis, the largest required entrance/exit lengths are the inlet of case B1 and the outlet of case B2. As the cross-sectional area and mass flow rate is a constant along the channel, then $\rho\bar{U}$ is also a constant. For convenience then, the parameters for equation (F.2) will be taken from the midpoint of the channel. This is along section A-A in Fig. 2.14 and along section C-C in Fig. 2.18. For the ease of estimating a mean velocity, the effective channel height h will be considered to be only the region where fluid molecules exist.

For the inlet of case 1, the effective channel height is approximately 3.6 nm, the mean density over this region is approximately 1500 kg/m^3 and, the mean velocity is approximately 70 m/s. At a temperature of 293 K, the average viscosity

of argon is estimated to be 2.25 $\times 10^{-}4$ Pa·s for the pressure range used in this thesis [Younglove and Hanley, 1986]. Inserting these values into equation (F.2) gives $L_e \approx$ 1.5 nm. For the outlet of case 2, the effective channel height is approximately 3.0 nm, the mean density over this region is approximately 1100 kg/m^3, and the mean velocity is approximately 140 m/s. Inserting these values into equation (F.2) again gives $L_e \approx 1.5$ nm. The entrance/exit region used for the Y-junction component in the bifurcating network cases is ≈ 6 nm in both the real and artificial regions, four times the largest value predicted from laminar macroscopic theory.

Appendix G

Generalised constraint requirements for the GeN-IMM

Consider a network with Q components, C channel components, W boundaries, and I internal boundaries. This means there is a total of $3W + C$ unknowns:

- W mass flow rates.
- W pressures.
- W heights.
- C lengths.

The constraints are just a generalised case of those introduced in chapter 2, so the total number of fixed properties must be the same. The total number of generalised constraints the user must specify is $2W - 3I/2$. To regain the constraints from chapter 2, the user specifies $W - I$ pressures, $W - C - I/2$ heights, and C lengths.

However, it is still possible to over- or under-constrain an individual component even when the total number of generalised constraints given is correct. If component q has W_q boundaries, then it must have $W_q - 1$ iterative scheme equations (i.e. equation (2.5)) and 1 equation for the conservation of mass within the component (i.e. equation (3.13)). If it is a channel component, there must also be 1 equation stating that the height is constant along the length of the channel (i.e. equation (3.4)). For component q, there are $3W_q + C_q$ unknowns, where $C_q = 1$ for a channel component and $C_q = 0$ for a junction component. The channel length is the extra unknown in channel components. Therefore, the maximum number of generalised constraints that may be specified in component q is $2W_q$.

There is also a minimum number of generalised constraints that must be set in each component. The value of variables at external boundaries can only be found through generalised constraints or equations (2.5) and (3.13), whereas variable values at internal boundaries can be determined from their neighbouring component (i.e. equations (3.1)-(3.3)). If component q has I_q internal boundaries, the maximum number of variables that can be determined from neighbouring components is $3I_q$, i.e. the mass flow rate, pressure and height at each internal boundary. This means that the minimum number of generalised constraints that must be specified in component q is $2W_q - 3I_q$.

As an example, consider the straight channel network introduced in chapter 2. For this network, $Q = 3$, $C = 1$, $W = 6$, and $I = 4$. Therefore, the user must specify a total of $2 * 6 - 3 * 4/2 = 6$ generalised constraints. This broke down into $6 - 4 = 2$ pressures, $6 - 1 - 4/2 = 3$ heights, and 1 length. Now, consider the individual components. For all three components, $W_q = 2$. In addition, for components #1 and #3, $I_q = 1$ and $C_q = 0$, while $I_q = 2$ and $C_q = 1$ for component #2. This means that for components #1 and #3, the maximum and minimum number of generalised constraints is $2 * 2 = 4$ and $4 - 3 * 1 = 1$, respectively. For component #2, these values are $2 * 2 = 4$ and $4 - 3 * 2 = -2$, respectively, with the negative value implying that there is no minimum requirement for the number of generalised constraints.

Appendix H

Numerical optimisation procedure for the verification of analytical solutions

The properties of the network that are fixed in this optimisation are: total volume V, parent channel length L_p, daughter channel lengths L_{d_i}, parent channel inlet pressure P_p, daughter channel outlet pressures P_{d_i}, and daughter flow-rate fraction Ψ_i. The fluid properties are fixed, so the mass flow rate q through any single channel is an explicit function of just two variables:

$$q = q(A, P_b), \tag{H.1}$$

where A is the cross-sectional area and P_b is the pressure at the parent-daughter branching point, i.e. it is the outlet pressure of the parent channel, and the inlet pressure of the daughter channels. Values for mass flow rates are obtained either from published sources, from high-resolution finite-difference slip solutions, from exact analytical expressions, or from stochastic particle calculations (for dilute gases). The channel cross-sectional areas are constrained by the volume equation (5.3) such that

$$A_p = \frac{\left(V - \sum_{i=1}^{N} A_{d_i} L_{d_i}\right)}{L_p}, \tag{H.2}$$

where N is the number of daughter chanels. To satisfy mass conservation in a two-level network, i.e. $q_p = \sum_{i=1}^{N} q_{d_i}$, the branching pressure is constrained:

$$P_b = \frac{\left(\frac{P_p}{L_p k_p} + \sum_{i=1}^{N} \frac{P_{d_i}}{L_{d_i} k_{d_i}} \right)}{\left(\frac{1}{L_p k_p} + \sum_{i=1}^{N} \frac{1}{L_{d_i} k_{d_i}} \right)}, \tag{H.3}$$

where, for fixed fluid properties, flow resistance per unit length k is solely a function of the cross-sectional area, as defined in equations (5.18), (5.30), (5.35), (6.27), and (6.39), for continuum flow, plug flow, slip flow, non-Newtonian fluid flow, and fully-rough turbulent flow, respectively. A further constraint ensures that the correct proportion of mass flow rate is taken by each daughter channel, i.e.

$$q_{d_i} = \Psi_i q_p. \tag{H.4}$$

Finally, there are physical limits that must be adhered to: no cross-sectional area can be negative, i.e.

$$A_p \geq 0, \tag{H.5}$$

$$A_{d_i} \geq 0, \tag{H.6}$$

and the branching pressure must lie between the parent inlet pressure and the largest of the daughter outlet pressures, i.e.

$$P_p > P_b > \max_{1 \leq i \leq N} \left(P_{d_i} \right). \tag{H.7}$$

An iterative procedure then finds the parent and daughter areas (and the pressure branching point) that satisfies the constraints of equations (H.2)-(H.7) and maximises the mass flow rate through the parent channel q_p.

Appendix I

Network aspect ratio limits for non-trivial optimal angles

The generalised angle law (equation (6.55)) becomes invalid when the network aspect ratio ($\beta = x_d/y_d$) is sufficiently small such that the branching point $x_b = L_p = 0$ and the solution is trivial. In this instance, the optimal branching point is at the inlet of the parent channel and the branching angle is simply

$$\cos\left(\frac{\theta}{2}\right) = \frac{x_d}{\sqrt{x_d^2 + y_d^2}}. \tag{I.1}$$

Substituting equation (I.1) into equation (6.55) and rearranging for β gives

$$\beta = 2\left(k_p - A_p \frac{\mathrm{d}k}{\mathrm{d}A}\bigg|_p\right)\left[\left(k_d - 4\Gamma A_p \frac{\mathrm{d}k}{\mathrm{d}A}\bigg|_p\right)^2 - 4\left(k_p - A_p \frac{\mathrm{d}k}{\mathrm{d}A}\bigg|_p\right)^2\right]^{-1/2}. \tag{I.2}$$

Equation (I.2) gives the network aspect ratio required for the optimal branching point to be at the parent channel inlet. Below this aspect ratio, equation (6.55) is invalid.

At the continuum-flow limit, substituting equations (6.57) and (6.58) into equation (I.2) gives

$$\beta = \frac{6}{\left[\left(2^{4/3} + \frac{8}{2^{2/3}}\right)^2 - 36\right]^{1/2}}, \tag{I.3}$$

or $\beta \approx 1.30$. At the plug-flow limit, substituting equations (6.61) and (6.62) into

equation (I.2) gives

$$\beta = \frac{5}{\left[\left(2^{6/5} + \frac{6}{2^{4/5}}\right)^2 - 25\right]^{1/2}}, \tag{I.4}$$

or $\beta \approx 1.77$. This means that to ensure non-trivial results, $\beta > 1.77$.

Bibliography

A. Alexiadis, D. A. Lockerby, M. K. Borg, and J. M. Reese. A laplacian-based algorithm for non-isothermal atomistic-continuum hybrid simulation of micro and nano-flows. *Comput. Methods Appl. Mech. Eng.*, 264:81–94, 2013.

M. P. Allen and D. J. Tildesley. *Computer Simulation of Liquids*. Clarendon Press, 1987.

H. C. Andersen. Molecular dynamics simulations at constant pressure and/or temperature. *J. Chem. Phys.*, 72(4):2384, 1980.

N. Asproulis, M. Kalweit, and D. Drikakis. A hybrid molecular continuum method using point wise coupling. *Adv. Eng. Softw.*, 46(1):85–92, 2012.

J. G. Aunins, B. Bader, A. Caola, J. Griffiths, M. Katz, P. Licari, K. Ram, C. S. Ranucci, and W. Zhou. Fluid mechanics, cell distribution, and environment in cellcube bioreactors. *Biotechnol. Prog.*, 19(1):2–8, 2003.

A. Bejan. *Shape and Structure, from Engineering to Nature*. Cambridge University Press, 2000.

A. Bejan, L. A. O. Rocha, and S. Lorente. Thermodynamic optimization of geometry: T- and y-shaped constructs of fluid streams. *Int. J. Therm. Sci.*, 39(9-11): 949–960, 2000.

H. J. C. Berendsen, J. P. M. Postma, W. F. van Gunsteren, A. DiNola, and J. R. Haak. Molecular dynamics with coupling to an external bath. *J. Chem. Phys.*, 81(8):3684, 1984.

G. A. Bird. *Molecular Gas Dynamics and the Direct Simulation of Gas Flows*. Oxford Engineering Science Series 42. Clarendon Press, 1994.

E. Blum. Die querschnittsbeziehungen zwischen stamm und sten im arteriensystem. *Pflgers Archiv Gesamte Physiol. Menschen Tiere*, 175(1):1–19, 1919.

M. K. Borg. *Hybrid Molecular-Continuum Modelling of Nano-Scale Flows*. PhD thesis, University of Strathclyde, 2010.

M. K. Borg, G. B. Macpherson, and J. M. Reese. Controllers for imposing continuum-to-molecular boundary conditions in arbitrary fluid flow geometries. *Mol. Simul.*, 36(10):745–757, 2010.

M. K. Borg, D. A. Lockerby, and J. M. Reese. A multiscale method for micro/nano flows of high aspect ratio. *J. Comput. Phys.*, 233:400–413, 2013a.

M. K. Borg, D. A. Lockerby, and J. M. Reese. A hybrid molecular-continuum simulation method for incompressible flows in micro/nanofluidic networks. *Microfluid. Nanofluid.*, 15(4):541–557, 2013b.

M. K. Borg, D. A. Lockerby, and J. M. Reese. Fluid simulations with atomistic resolution: a hybrid multiscale method with field-wise coupling. *J. Comput. Phys.*, 255:149–165, 2013c.

M. K. Borg, D. A. Lockerby, and J. M. Reese. The FADE mass-stat: A technique for inserting or deleting particles in molecular dynamics simulations. *J. Chem. Phys.*, 140(7):074110, 2014.

M. Born and R. Oppenheimer. Zur quantentheorie der molekeln. *Ann. Phys.*, 389 (20):457–484, 1927.

M. Brenner, X. Shi, and S. Nagel. Iterated instabilities during droplet fission. *Phys. Rev. Lett.*, 73(25):3391–3394, 1994.

P. J. Cadusch, B. D. Todd, J. Zhang, and P. J. Daivis. A non-local hydrodynamic model for the shear viscosity of confined fluids: analysis of a homogeneous kernel. *J. Phys. A: Math. Theor.*, 41(3):035501, 2008.

Y. Chen and P. Cheng. Heat transfer and pressure drop in fractal tree-like microchannel nets. *Int. J. Heat Mass Transf.*, 45(13):2643–2648, 2002.

D. L. Cohn. Optimal systems: I. the vascular system. *Bull. Math. Biophys.*, 16(1): 59–74, 1954.

D. L. Cohn. Optimal systems: Ii. the vascular system. *Bull. Math. Biophys.*, 17(3): 219–227, 1955.

A. de-Waele. Viscometry and plastometry. *Oil. Color. Chem. Assoc. J.*, 6:33–88, 1923.

R. Delgado-Buscalioni and P. Coveney. Continuum-particle hybrid coupling for mass, momentum, and energy transfers in unsteady fluid flow. *Phys. Rev. E*, 67 (4):046704, 2003a.

R. Delgado-Buscalioni and P. V. Coveney. Usher: An algorithm for particle insertion in dense fluids. *J. Chem. Phys.*, 119(2):978, 2003b.

A. Diaz Lantada, B. Pareja Sánchez, C. Gómez Murillo, and J. Urbieta Sotillo. Fractals in tissue engineering: toward biomimetic cell-culture matrices, microsystems and microstructured implants. *Expert Rev. Med. Devices*, 10(5):629–648, 2013.

S. Y. Docherty, W. D. Nicholls, M. K. Borg, D. A. Lockerby, and J. M. Reese. Boundary conditions for molecular dynamics simulations of water transport through nanotubes. *Proc. Inst. Mech. Eng., Part C*, 228(1):186–195, 2013.

W. E. *Principles of Multiscale Modeling.* Cambridge University Press, 2011.

W. E and B. Engquist. The hetereogeneous multi-scale methods. *Commun. Math. Sci.*, 1(1):87–132, 2003.

W. E, B. Engquist, and Z. Huang. Heterogeneous multiscale method: A general methodology for multiscale modeling. *Phys. Rev. B*, 67(9):092101, 2003.

W. E, B. Engquist, X. T. Li, and W. Q. Ren. Heterogeneous multiscale methods: A review. *Commun. comput. phys.*, 2(3):367–450, 2007.

W. E, W. Ren, and E. Vanden-Eijnden. A general strategy for designing seamless multiscale methods. *J. Comput. Phys.*, 228(15):5437–5453, 2009.

Y. Eguchi and T. Karino. Measurement of rheologic property of blood by a falling-ball blood viscometer. *Ann. Biomed. Eng.*, 36(4):545–553, 2008.

C. Eloy. Leonardo's rule, self-similarity, and wind-induced stresses in trees. *Phys. Rev. Lett.*, 107(25), 2011.

D. F. Emerich and C. G. Thanos. The pinpoint promise of nanoparticle-based drug delivery and molecular diagnosis. *Biomol. Eng.*, 23(4):171–184, 2006.

D. R. Emerson, K. Cieślicki, X. Gu, and R. W. Barber. Biomimetic design of microfluidic manifolds based on a generalised murray's law. *Lab Chip*, 6(3):447–454, 2006.

R. Fahræus and T. Lindqvist. The viscosity of the blood in narrow capillary tubes. *Am. J. Physiol.*, 96(3):562–568, 1931.

X. Fan, N. Phan-Thien, N. T. Yong, and X. Diao. Molecular dynamics simulation of a liquid in a complex nano channel flow. *Phys. Fluids*, 14(3):1146, 2002.

E. G. Flekkøy, G. Wagner, and J. Feder. Hybrid model for combined particle and continuum dynamics. *Europhys. Lett.*, 52(3):271–276, 2000.

E. G. Flekkøy, R. Delgado-Buscalioni, and P. Coveney. Flux boundary conditions in particle simulations. *Phys. Rev. E*, 72(2), 2005.

M. Gad-el Hak. The fluid mechanics of microdevices-the freeman scholar lecture. *J. Fluids. Eng.*, 121(1):5, 1999.

L. Gosselin and A. Bejan. Tree networks for minimal pumping power. *Int. J. Therm. Sci.*, 44(1):53–63, 2005.

L. Gosselin and A. K. da Silva. Constructal microchannel networks of rarefied gas with minimal flow resistance. *J. Appl. Phys.*, 101(11):114902, 2007.

M. Griebel, S. Knapek, and G. W. Zumbusch. *Numerical Simulation in Molecular Dynamics*. Springer, 2007.

N. G. Hadjiconstantinou. Hybrid atomistic-continuum formulations and the moving contact-line problem. *J. Comput. Phys.*, 154(2):245–265, 1999.

N. G. Hadjiconstantinou. Comment on cercignani's second-order slip coefficient. *Phys. Fluids.*, 15(8):2352, 2003.

N. G. Hadjiconstantinou. Discussion of recent developments in hybrid atomistic-continuum methods for multiscale hydrodynamics. *Bull. Pol. Acad. Sci.: Tech. Sci.*, 53(4):335–342, 2005.

N. G. Hadjiconstantinou and A. T. Patera. Heterogeneous atomistic-continuum representations for dense fluid systems. *Int. J. Mod. Phys. C*, 8(4):967–976, 1997.

J. Hansen and I. R. McDonald. *Theory of Simple Liquids*. Elsevier Academic Press, 2006.

W. R. Hess. ber die periphere regulierung der blutzirkulation. *Pflgers Archiv Gesamte Physiol. Menschen Tiere*, 168(9-12):439–490, 1917.

R. Hockney. The potential calculation and some applications. *Methods Comp. Phys.*, 9:136–211, 1970.

G. Hooper. Diameters of bronchi at asymmetrical divisions. *Respir. Physiol.*, 31(3): 291–294, 1977.

W. Hoover. Canonical dynamics: Equilibrium phase-space distributions. *Phys. Rev. A*, 31(3):1695–1697, 1985.

K. Horsfield. Morphometry of the small pulmonary arteries in man. *Circ. Res.*, 42 (5):593–597, 1978.

K. Horsfield. Are diameter, length and branching ratios meaningful in the lung? *J. Theor. Biol.*, 87(4):773–784, 1980.

K. Horsfield and G. Cumming. Angles of branching and diameters of branches in the human bronchial tree. *Bull. Math. Biophys.*, 29(2):245–259, 1967.

K. Horsfield and G. Cumming. Morphology of the bronchial tree in man. *J. App. Physiol.*, 24(3):373–383, 1968.

K. Horsfield, F. G. Relea, and G. Gumming. Diameter, length and branching ratios in the bronchial tree. *Respir. Physiol.*, 26(3):351–356, 1976.

R. E. Horton. Erosional development of streams and their drainage basins; hydrophysical approach to quantitative morphology. *Geol. Soc. Am. Bull.*, 56(3): 275, 1945.

C. Huang, J. W. Gregory, and J. P. Sullivan. Microchannel pressure measurements using molecular sensors. *J. Microelectromech. Syst.*, 16(4):777–785, 2007.

G. M. Hutchins, M. M. Miner, and J. K. Boitnott. Vessel caliber and branch-angle of human coronary artery branch-points. *Circ. Res.*, 38(6):572–576, 1976.

H. Jiang, X. Weng, and D. Li. Microfluidic whole-blood immunoassays. *Microfluid. Nanofluid.*, 10(5):941–964, 2010.

J. E. Jones. On the determination of molecular fields. II. from the equation of state of a gas. *Proc. R. Soc. A*, 106(738):463–477, 1924.

M. Kalweit and D. Drikakis. Multiscale methods for micro/nano flows and materials. *J. Comput. Theor. Nanosci.*, 5(9):1923–1938, 2008.

A. Kamiya and T. Togawa. Optimal branching structure of the vascular tree. *Bull. Math. Biophys.*, 34(4):431–438, 1972.

A. Kamiya, T. Togawa, and A. Yamamoto. Theoretical relationship between the optimal models of the vascular tree. *Bull. Math. Biol.*, 36(3):311–323, 1974.

G. Karniadakis, A. Beskok, and N. R. Aluru. *Microflows and Nanoflows*. Springer, 2005.

G. S. Kassab and Y. B. Fung. The pattern of coronary arteriolar bifurcations and the uniform shear hypothesis. *Ann. Biomed. Eng.*, 23(1):13–20, 1995.

M. Knudsen. Die gesetze der molekularstrmung und der inneren reibungsstrmung der gase durch rhren. *Ann. Phys.*, 333(1):75–130, 1909.

J. Koplik and J. R. Banavar. Continuum deductions from molecular hydrodynamics. *Annu. Rev. Fluid Mech.*, 27(1):257–292, 1995.

J. Koplik, J. Banavar, and J. Willemsen. Molecular dynamics of poiseuille flow and moving contact lines. *Phys. Rev. Lett.*, 60(13):1282–1285, 1988.

P. Koumoutsakos. Multiscale flow simulations using particles. *Annu. Rev. Fluid Mech.*, 37(1):457–487, 2005.

M. L. Kovarik and S. C. Jacobson. Nanofluidics in lab-on-a-chip devices. *Anal. Chem.*, 81(17):7133–7140, 2009.

M. LaBarbera. Principles of design of fluid transport systems in zoology. *Science*, 249(4972):992–1000, 1990.

K. P. Lee, T. C. Arnot, and D. Mattia. A review of reverse osmosis membrane materials for desalination - development to date and future potential. *J. Membr. Sci.*, 370(1-2):1–22, 2011.

E. W. Lemmon, M. O. McLinden, and D. G. Friend. Thermophysical properties of fluid systems. In *NIST Chemistry WebBook, NIST Standard Reference Database Number 69*, page 20899. National Institute of Standards and Technology, 2015.

D. Lim, Y. Kamotani, B. Cho, J. Mazumder, and S. Takayama. Fabrication of microfluidic mixers and artificial vasculatures using a high-brightness diode-pumped nd:yag laser direct write method. *Lab Chip.*, 3(4):318, 2003.

D. A. Lockerby, A. Patronis, M. K. Borg, and J. M. Reese. Asynchronous coupling of hybrid models for efficient simulation of multiscale systems. *J. Comput. Phys.*, 284:261–272, 2015.

S. K. Loyalka and S. A. Hamoodi. Poiseuille flow of a rarefied gas in a cylindrical tube: Solution of linearized boltzmann equation. *Phys. Fluids. A.*, 2(11):2061, 1990.

S. K. Loyalka and S. A. Hamoodi. Erratum: "poiseuille flow of a rarefied gas in a cylindrical tube: Solution of linearized boltzmann equation" [phys. fluids a 2, 2061 (1990)]. *Phys. Fluids. A.*, 3(11):2825, 1991.

N. Ma, K. W. Koelling, and J. J. Chalmers. Fabrication and use of a transient contractional flow device to quantify the sensitivity of mammalian and insect cells to hydrodynamic forces. *Biotechnol. Bioeng.*, 80(4):428–437, 2002.

G. B. Macpherson and J. M. Reese. Molecular dynamics in arbitrary geometries: parallel evaluation of pair forces. *Mol. Simul.*, 34(1):97–115, 2008.

D. Mantzalis, N. Asproulis, and D. Drikakis. Filtering carbon dioxide through carbon nanotubes. *Chem. Phys. Lett.*, 506(1-3):81–85, 2011.

D. Mattia and F. Calabrò. Explaining high flow rate of water in carbon nanotubes via solid-liquid molecular interactions. *Microfluid. Nanofluid.*, 13(1):125–130, 2012.

D. Mattia and Y. Gogotsi. Review: static and dynamic behavior of liquids inside carbon nanotubes. *Microfluid. Nanofluid.*, 5(3):289–305, 2008.

H. N. Mayrovitz and J. Roy. Microvascular blood flow: evidence indicating a cubic dependence on arteriolar diameter. *Am. J. Physiol.: Heart Circ. Physiol.*, 245(6): 1031–1038, 1983.

K. A. McCulloh and J. S. Sperry. The evaluation of murray's law in psilotum nudum (psilotaceae), an analogue of ancestral vascular plants. *Am. J. Bot.*, 92 (6):985–989, 2005.

K. A. McCulloh, J. S. Sperry, and F. R. Adler. Water transport in plants obeys murray's law. *Nature*, 421(6926):939–942, 2003.

K. A. McCulloh, J. S. Sperry, and F. R. Adler. Murray's law and the hydraulic vs mechanical functioning of wood. *Funct. Ecol.*, 18(6):931–938, 2004.

W. S. Miller. The structure of the lung. *J. Morphol.*, 8(1):165–188, 1893.

W. S. Miller. *The Lung.* Baillière, Tindall & Cox, 1937.

J. H. Milsum and F. A. Roberge. Physiologcial regulation and control. In *Foundations of Mathematical Biology*, pages 1–95. Academic Press, 1973.

S. K. Mitra and S. Chakraborty. *Microfluidics and Nanofluidics Handbook*. CRC Press, 2012.

K. M. Mohamed and A. A. Mohamad. A review of the development of hybrid atomistic-continuum methods for dense fluids. *Microfluid. Nanofluid.*, 8(3):283–302, 2009.

C. D. Murray. The physiological principle of minimum work: I. the vascular system and the cost of blood volume. *Proc. Natl. Acad. Sci.*, 12(3):207–214, 1926a.

C. D. Murray. The physiological principle of minimum work: II. oxygen exchange in capillaries. *Proc. Natl. Acad. Sci.*, 12(5):299–304, 1926b.

C. D. Murray. The physiological principle of minimum work applied to the angle of branching of arteries. *J. Gen. Physiol.*, 9(6):835–841, 1926c.

W. D. Nicholls. *Molecular Dynamics Simulations of Liquid Flow in and around Carbon nanotubes*. PhD thesis, University of Strathclyde, 2012.

X. Nie, S. Chen, and M. O. Robbins. Hybrid continuum-atomistic simulation of singular corner flow. *Phys. Fluids*, 16(10):3579, 2004a.

X. B. Nie, S. Y. Chen, W. E, and M. O. Robbins. A continuum and molecular dynamics hybrid method for micro- and nano-fluid flow. *J. Fluid Mech.*, 500: 55–64, 2004b.

S. Nosé. A molecular dynamics method for simulations in the canonical ensemble. *Mol. Phys.*, 52(2):255–268, 1984.

S. O'Connell and P. Thompson. Molecular dynamics-continuum hybrid computations: a tool for studying complex fluid flows. *Phys. Rev. E*, 52(6):R5792–R5795, 1995.

D. E. Olsen, G. A. Dart, and G. F. Filley. Pressure drop and fluid flow regime of air inspired into the human lung. *J. Appl. Physiol.*, 28(4):482–494, 1970.

W. Ostwald. About the rate function of the viscosity of dispersed systems. *Kolloid Z.*, 36:99–117, 1925.

A. Patronis and D. A. Lockerby. Multiscale simulation of non-isothermal microchannel gas flows. *J. Comput. Phys.*, 270:532–543, 2014.

A. Patronis, D. A. Lockerby, M. K. Borg, and J. M. Reese. Hybrid continuum-molecular modelling of multiscale internal gas flows. *J. Comput. Phys.*, 255: 558–571, 2013.

S. Prakash and J. Yeom. *Nanofluidics and Microfluidics*. William Andrew, 2014.

M. Praprotnik, L. Delle Site, and K. Kremer. Adaptive resolution molecular-dynamics simulation: Changing the degrees of freedom on the fly. *J. Chem. Phys.*, 123(22):224106, 2005.

G. A. Radtke, N. G. Hadjiconstantinou, and W. Wagner. Low-noise monte carlo simulation of the variable hard sphere gas. *Phys. Fluids.*, 23(3):030606, 2011.

D. C. Rapaport. *The Art of Molecular Dynamics Simulation*. Cambridge University Press, 2004.

N. Rashevsky. The principle of adequate design. In *Foundations of Mathematical Biology*, pages 143–175. Academic Press, 1973.

W. Ren and W. E. Heterogeneous multiscale method for the modeling of complex fluids and micro-fluidics. *J. Comput. Phys.*, 204(1):1–26, 2005.

C. Renault, S. Colin, S. Orieux, P. Cognet, and T. Tzédakis. Optimal design of multi-channel microreactor for uniform residence time distribution. *Microsyst. Technol.*, 18(2):209–223, 2012.

R. Revellin, F. Rousset, D. Baud, and J. Bonjour. Extension of murray's law using a non-newtonian model of blood flow. *Theor. Biol. Med. Modell.*, 6(1):7, 2009.

K. Ritos. *Water flow at the nanoscale: a computational molecular and fluid dynamics investigation*. PhD thesis, University of Strathclyde, 2014.

R. Rosen. *Optimality Principles in Biology*. Butterworths, 1967.

A. G. Roy. Optimal angular geometry models of river branching. *Geographical Analysis*, 15(2):87–96, 1983.

A. G. Roy and M. J. Woldenberg. A generalization of the optimal models of arterial branching. *Bull. Math. Biol.*, 44(3):349–360, 1982.

R. Schoch, J. Han, and P. Renaud. Transport phenomena in nanofluidics. *Rev. Mod. Phys.*, 80(3):839–883, 2008.

E. Schrödinger. An undulatory theory of the mechanics of atoms and molecules. *Phys. Rev.*, 28(6):1049–1070, 1926.

L. I. Segerink and J. C. T. Eijkel. Nanofluidics in point of care applications. *Lab Chip*, 14(17):3201–3205, 2014.

S. M. Senn and D. Poulikakos. Laminar mixing, heat transfer and pressure drop in tree-like microchannel nets and their application for thermal management in polymer electrolyte fuel cells. *J. Power Sources*, 130(1-2):178–191, 2004.

F. Sharipov. Rarefied gas flow through a long tube at any temperature ratio. *J. Vac. Sci. Technol. A.*, 14(4):2627, 1996.

T. F. Sherman. On connecting large vessels to small. the meaning of murray's law. *J. Gen. Physiol.*, 78(4):431–453, 1981.

P. D. Stein and H. N. Sabbah. Turbulent blood flow in the ascending aorta of humans with normal and diseased aortic valves. *Circ. Res.*, 39(1):58–65, 1976.

N. Suwa, T. Niwa, H. Fukasawa, and Y. Sasaki. Estimation of intravascular blood pressure gradient by mathematical analysis of arterial casts. *Tohoku J. Exp. Med.*, 79(2):168–198, 1963.

W. C. Swope, H. C. Anderson, P. H. Berens, and K. R. Wilson. A computer simulation method for the calculation of equilibrium constants for the formation of physical clusters of molecules: Application to small water clusters. *J. Chem. Phys.*, 76(1):637–649, 1982.

L. A. Taber, S. Ng, A. M. Quesnel, J. Whatman, and C. J. Carmen. Investigating murray's law in the chick embryo. *J. Biomech.*, 34(1):121–124, 2001.

K. Tesch. On some extensions of murray's law. *Task Quarterly*, 14(3):227–235, 2010.

D. W. Thompson. *On Growth and Form.* Cambridge University Press, 1942.

P. Thompson and M. Robbins. Simulations of contact-line motion: Slip and the dynamic contact angle. *Phys. Rev. Lett.*, 63(7):766–769, 1989.

P. A. Thompson and S. M. Troian. A general boundary condition for liquid flow at solid surfaces. *Nature*, 389(6649):360–362, 1997.

B. Todd, J. Hansen, and P. Daivis. Nonlocal shear stress for homogeneous fluids. *Phys. Rev. Lett.*, 100(19), 2008.

B. D. Todd. Cats, maps and nanoflows: some recent developments in nonequilibrium nanofluidics. *Mol. Simul.*, 31(6-7):411–428, 2005.

K. P. Travis and K. E. Gubbins. Poiseuille flow of lennard-jones fluids in narrow slit pores. *J. Chem. Phys.*, 112(4):1984, 2000.

K. P. Travis, B. D. Todd, and D. J. Evans. Poiseuille flow of molecular fluids. *Phys. A: Stat. Theor. Phys.*, 240(1-2):315–327, 1997.

D. B. Tuckerman and R. F. W. Pease. High performance heat sinking for vlsi. *IEEE Electron Device Lett.*, 2(5):126–129, 1981.

H. Uylings. Optimization of diameters and bifurcation angles in lung and vascular tree structures. *Bull. Math. Biol.*, 39(5):509–520, 1977.

L. Verlet. Computer "experiments" on classical fluids. i. thermodynamical properties of lennard-jones molecules. *Phys. Rev.*, 159(1):98–103, 1967.

G. Wagner, E. Flekkøy, J. Feder, and T. Jøssang. Coupling molecular dynamics and continuum dynamics. *Comput. Phys. Commun.*, 147(1-2):670–673, 2002.

R. A. Waltz, J. L. Morales, J. Nocedal, and D. Orban. An interior algorithm for nonlinear optimization that combines line search and trust region steps. *Math. Program.*, 107(3):391–408, 2005.

X. Wang, A. S. Mujumdar, and C. Yap. Thermal characteristics of tree-shaped microchannel nets for cooling of a rectangular heat sink. *Int. J. Therm. Sci.*, 45 (11):1103–1112, 2006.

E. R. Weibel. *Morphometry of the Human Lung.* Springer, 1963.

E. R. Weibel and D. M. Gomez. Architecture of the human lung: Use of quantitative methods establishes fundamental relations between size and number of lung structures. *Science*, 137(3530):577–585, 1962.

T. Werder, J. H. Walther, and P. Koumoutsakos. Hybrid atomistic-continuum method for the simulation of dense fluid flows. *J. Comput. Phys.*, 205(1):373–390, 2005.

F. M. White. *Viscous Fluid Flow.* McGraw-Hill, 1974.

H. S. Wijesinghe and N. G. Hadjiconstantinou. Discussion of hybrid atomistic-continuum methods for multiscale hydrodynamics. *Int. J. Multiscale Comput. Eng.*, 2(2):189–202, 2004.

H. R. Williams, R. S. Trask, P. M. Weaver, and I. P. Bond. Minimum mass vascular networks in multifunctional materials. *J. R. Soc. Interface*, 5(18):55–65, 2008.

T. A. Wilson. Design of the bronchial tree. *Nature*, 213(5077):668–669, 1967.

L. P. Yarin, A. Mosyak, and G. Hetsroni. *Fluid Flow, Heat Transfer and Boiling in Micro-channels*. Springer, 2009.

S. Yasuda and R. Yamamoto. A model for hybrid simulations of molecular dynamics and computational fluid dynamics. *Phys. Fluids*, 20(11):113101, 2008.

T. Young. The croonian lecture: On the functions of the heart and arteries. *Philos. Trans. R. Soc. London*, 99(0):1–31, 1809.

B. A. Younglove and H. J. M. Hanley. The viscosity and thermal conductivity coefficients of gaseous and liquid argon. *J. Phys. Chem. Ref. Data*, 15(4):1323, 1986.

M. Zamir. The role of shear forces in arterial branching. *J. Gen. Physiol.*, 67(2): 213–222, 1976a.

M. Zamir. Optimality principles in arterial branching. *J. Theor. Biol.*, 62(1):227–251, 1976b.

M. Zamir. Shear forces and blood vessel radii in the cardiovascular system. *J. Gen. Physiol.*, 69(4):449–461, 1977.

M. Zamir. Nonsymmetrical bifurcations in arterial branching. *J. Gen. Physiol.*, 72 (6):837–845, 1978.

M. Zamir and N. Brown. Arterial branching in various parts of the cardiovascular system. *Am. J. Anat.*, 163(4):295–307, 1982.

M. Zamir and H. Chee. Branching characteristics of human coronary arteries. *Can. J. Physiol. Pharmacol.*, 64(6):661–668, 1986.

M. Zamir and J. A. Medeiros. Arterial branching in man and monkey. *J. Gen. Physiol.*, 79(3):353–360, 1982.

M. Zamir, J. A. Medeiros, and T. K. Cunningham. Arterial bifurcations in the human retina. *J. Gen. Physiol.*, 74(4):537–548, 1979.

M. Zamir, S. M. Wrigley, and B. L. Langille. Arterial bifurcations in the cardiovascular system of a rat. *J. Gen. Physiol.*, 81(3):325–335, 1983.

M. Zamir, S. Phipps, B. L. Langille, and T. H. Wonnacott. Branching characteristics of coronary arteries in rats. *Can. J. Physiol. Pharmacol.*, 62(12):1453–1459, 1984.

F. Zhu, E. Tajkhorshid, and K. Schulten. Pressure-induced water transport in membrane channels studied by molecular dynamics. *Biophys. J.*, 83(1):154–160, 2002.

F. Zhu, E. Tajkhorshid, and K. Schulten. Theory and simulation of water permeation in aquaporin-1. *Biophys. J.*, 86(1):50–57, 2004.

V. D. Zimparov, A. K. da Silva, and A. Bejan. Thermodynamic optimization of tree-shaped flow geometries. *Int. J. Heat Mass Transfer*, 49(9-10):1619–1630, 2006.